



**Determination of  
Metal Quality of  
Aluminium and Its Alloys**

by

DERYA DISPINAR

A thesis submitted to  
The University of Birmingham  
For the degree of  
DOCTOR OF PHILOSOPHY

UNIVERSITY OF  
BIRMINGHAM

**University of Birmingham Research Archive**

**e-theses repository**

This unpublished thesis/dissertation is copyright of the author and/or third parties. The intellectual property rights of the author or third parties in respect of this work are as defined by The Copyright Designs and Patents Act 1988 or as modified by any successor legislation.

Any use made of information contained in this thesis/dissertation must be in accordance with that legislation and must be properly acknowledged. Further distribution or reproduction in any format is prohibited without the permission of the copyright holder.

## Abstract

Aluminium alloy castings are being used increasingly in safety-critical applications in the automotive and aerospace industries. To produce castings of sufficient quality, it is, therefore, important to understand the mechanisms of the formation of defects in aluminium melts, and important to have a reliable and simple means of detection.

During the production of aluminium ingots and castings, the surface oxide on the liquid is folded in to produce crack-like defects (bifilms) that are extremely thin, but can be extremely extensive, and so constitute seriously detrimental defects. However, the presence of bifilms has not been widely accepted, because there has been no single metal quality test that has been able to resolve features that are only nanometres, or sometimes micrometres, in thickness. In the past, porosity has usually been held solely responsible for most failures in aluminium alloys, and hydrogen has been blamed as the actual cause. In this work it has been found that bifilms are the initiator and hydrogen is only a contributor in the porosity formation process. For the first time, evidence is presented for the contribution of air (or perhaps more strictly, residual nitrogen from air) as an additional gas, adding to hydrogen in pores in cast Al alloys.

The Reduced Pressure Test (RPT) is used which is a simple and widely known test, is cost effective and involves no complicated equipment or consumables, thus recommending it for implementation on the foundry floor. Nevertheless, the discriminating use of the RPT clearly reveals the existence of bifilms, and the effect of hydrogen on porosity formation. On this basis, several Al-Si based alloys were studied: LM0 (99.5% Al), LM2 (Al-11Si), LM4 (Al-5Si-3Cu), LM25 (Al-7Si-0.4Mg), LM24 (Al-8Si-3CuFe), LM27 (Al-6Si-2Cu). A quality index -*Bifilm Index*- is introduced to quantify the results of the reduced pressure test which helps to assess the aluminium melt quality in best means. In addition, mechanical tests were carried out to correlate bifilm index with mechanical properties.

The oxide content of recycled aluminium alloys has been a long-standing and serious problem. This thesis reports the use of the RPT test developed in this study to an industrial remelting facility that has resulted in significant benefit.

*to my wife, muzzy,  
without whom I wouldn't be*

## Acknowledgement

It is the greatest honour to be able to work under supervision of Professor John Campbell. I am grateful to be one of the luckiest persons who had a chance to work with him. I am thankful and gratified for all of his help, assistance, inspiration and guidance on the all aspects.

I would like to thank Professor Nick R. Green for his support and supervision. I thank the University of Istanbul, Metallurgy and Materials Engineering, Head of Department, Prof. Dr. Ibrahim Yusufoglu, for his encouragement to help me begin my postgraduate study in University of Birmingham. Thanks to all of my colleagues, the research assistants in the department, particularly Dr. Cem Kahruman in Istanbul. I would have to acknowledge Higher Education Council of Turkey, for supporting my research.

I would like to acknowledge the financial support of Norton Aluminium and particularly their assistance in the use of facilities in the foundry. The research was also partially supported by University of Birmingham.

I would like to thank Adrian Caden for his assistance during the experiments and rest of the IRC group for their warm and kind friendship. Although we could not finalise this project together, I would like to thank to Dr. Simon Fox for his effort and support on the start of my thesis.

I would like to express my gratitude to Nazım Karadağ for his commitment and continued support as my best friend.

My mom and dad, and my whole family; there are no words to express my feelings for your never-ending support and belief in me.

Above all, I would like to express my deepest gratitude to my wife and best friend Muzi, for her love and support and everything during this work and ever.

*Non scholæ sed vitæ discimus...*

# TABLE of CONTENTS

<b>CHAPTER 1 INTRODUCTION .....</b>	<b>1</b>
<b>CHAPTER 2 LITERATURE REVIEW .....</b>	<b>4</b>
<b>2.1 History of Casting and Aluminium .....</b>	<b>5</b>
2.1.1 Casting Processes.....	6
<b>2.2 Metal Quality .....</b>	<b>8</b>
2.2.1 The Dissolution of Hydrogen.....	9
2.2.2 Formation of Oxide Film .....	10
<b>2.3 The Concept of Surface Entrainment: Bifilms .....</b>	<b>14</b>
2.3.1 Incorporation of Surface Films into Melts .....	15
<b>2.4 Compacting and Unfurling (Ravelling and Unravelling) of Bifilms.....</b>	<b>15</b>
<b>2.5 Porosity Phenomena .....</b>	<b>16</b>
2.5.1 Nucleation .....	16
2.5.2 Growth .....	18
2.5.3 The New Approach to Pore Formation .....	18
<b>2.6 Porosity Types .....</b>	<b>20</b>
2.6.1 Shrinkage Porosity .....	21
2.6.2 Gas Porosity .....	22
<b>2.7 Factors Affecting Porosity.....</b>	<b>22</b>
2.7.1 An Increase in the Hydrogen Content of the Melt .....	23
2.7.2 An Increase in the Entrained (exogenous) Inclusion Content .....	23
2.7.3 Oxide Structure .....	23
2.7.4 Alloying .....	24
2.7.5 Cooling Rate .....	24
2.7.6 Intermetallics .....	24
<b>2.8 Measurement of Metal Quality.....</b>	<b>25</b>
2.8.1 Inclusion Detection Techniques .....	26
2.8.1.1 LIMCA (Liquid Metal Cleanliness Analyser) .....	26
2.8.1.2 PoDFA – PREFIL (Porous Disk Filtration Analysis) .....	26
2.8.1.3 Ultrasonic .....	27
2.8.1.4 Summary of Quality Assessment Techniques .....	27
2.8.2 Reduced Pressure Test (RPT) .....	28
<b>2.9 Secondary Remelting - Recycling .....</b>	<b>29</b>
2.9.1 Melting .....	30
2.9.1.1 Rotary Furnace .....	30
2.9.1.2 Tilt Rotary Furnace .....	31
2.9.1.3 Electric Furnace .....	31
2.9.2 Fluxing .....	31
2.9.3 Degassing .....	32
<b>Summary .....</b>	<b>33</b>

<b>CHAPTER 3 EXPERIMENTAL PROCEDURE .....</b>	<b>34</b>
3.1 Alloys .....	34
3.2 Reduced Pressure Test (RPT) .....	34
3.2.1 Laboratory Tests .....	35
3.2.2 Industrial Tests .....	35
3.3 Hydrogen Measurement .....	37
3.4 Moulds .....	38
3.5 Density Measurement .....	39
3.6 Image Analysis .....	40
3.7 Tensile Tests .....	41
3.7.1 Weibull Analysis.....	42
3.8 Microscopy and Microanalysis .....	43
3.9 Quality Index Studies.....	43
 <b>CHAPTER 4 RESULTS .....</b>	 <b>45</b>
4.1 Laboratory Tests .....	45
4.1.1 Effect of Binder Type and Content on RPT .....	45
4.1.2 RPT Optimisation of Temperature and Pressure .....	46
4.1.3 The Assessment of Effect of Bifilms on RPT .....	47
4.2 Industrial Trials .....	47
4.2.1 Fluxing and Degassing Studies .....	47
4.2.2 Studies at Casting Area: Two Different Casting Heights .....	48
4.2.3 Studies in Holding Furnace: Trials on use of Diffusers .....	49
4.3 Quality Index Results and Evaluation of Bifilm Index .....	51
4.3.1 Methods Investigated to Quantify RPT .....	52
4.3.1.1 Laboratory Test Results .....	53
4.3.1.2 Industrial Test Results .....	53
4.3.2 Relationship between Bifilm Index and Number of Pores .....	55
4.4 Calculation of Air Gap between Bifilm .....	56
4.5 Tensile Tests.....	56
4.5.1 Optimisation of Tensile Test Pattern .....	56
4.5.2 Comparison of Different Conditions .....	57
 <b>CHAPTER 5 DISCUSSION .....</b>	 <b>59</b>
5.1 The RPT Mould Effect Study .....	59
5.2 Pore Formation and Growth .....	59

5.3	Effect of Time and Temperature on Pore Morphology .....	65
5.4	Effect of Different Pouring Height .....	68
5.5	Effect of Different Gas Flow Rates during Fluxing and Degassing .....	69
5.6	Comparison of Effect of Ceramic Diffusers During Fluxing .....	70
5.7	Evaluation of Bifilm Index .....	71
5.8	The Relationship between Number of Pores, Hydrogen and Bifilm Index .....	77
5.9	Image Analysis Studies .....	79
5.10	Optimum Pressure Considerations .....	80
5.11	Effect of Bifilms on Mechanical Properties .....	81
5.12	Parameters Affecting the RPT Sensitivity .....	83
5.12.1	Sample Pouring Temperature .....	84
5.12.2	Microstructure .....	84
5.12.3	Chamber Pressure .....	84
5.12.4	Shrinkage .....	85
5.12.5	Melt Gas Content .....	85
<b>CHAPTER 6 CONCLUSIONS .....</b>		<b>86</b>
<b>FUTURE WORK .....</b>		<b>88</b>
<b>PUBLICATIONS.....</b>		<b>89</b>
<b>REFERENCES.....</b>		<b>91</b>
<b>APPENDICES</b>		
I	Calculation of Theoretical Hydrogen-Density Relationship .....	105
II	Comparison of Image Analysis Software .....	107
III	Calculation of Air Gap between Bifilm .....	114
<b>FIGURES .....</b>		<b>117</b>
<b>TABLES .....</b>		<b>192</b>

## List of Illustrations

<b>Figure 2.1:</b> Surface turbulence; probably the most common mechanism of introducing bifilm into the melt: The folding of the film, dry side to dry side, will trap gas between the surfaces[5] .....	115
<b>Figure 2.2:</b> Solubility of hydrogen in pure aluminium [34] .....	115
<b>Figure 2.3:</b> (a) Supersaturation of hydrogen in the absence of bifilm (b) pore formation and diffusion of hydrogen into the gap between the bifilm.....	115
<b>Figure 2.4:</b> Oxygen partial pressure and oxide structure[42].....	116
<b>Figure 2.5:</b> the effect of increasing height on a falling stream of liquid [5];.....	116
a) the oxide film remains intact,	
b) the oxide film being detached and accumulating to form a dross ring,	
c) the oxide film and air being entrained in the bulk melt	
<b>Figure 2.6:</b> confluence geometry: separation and rejoining involves the formation of films [5] a) at the side, b) randomly, c) on the top.....	116
<b>Figure 2.7:</b> Energies of a growing pore [5] .....	117
<b>Figure 2.8:</b> Geometry of a bubble [5]: (a) wetting and contact angle between liquid and solid (b) energy association between homogeneous and heterogeneous nucleation.....	117
<b>Figure 2.9:</b> Feeding mechanisms in a solidifying casting [5].....	117
<b>Figure 2.10:</b> Volumetric shrinkage in long freezing range alloy depending on the thickness of casting [5].....	118
<b>Figure 2.11:</b> Typical pore microstructure in an Al-Si alloy (a) interdendritic [172], (b) intereutectic [174].....	118
<b>Figure 2.12:</b> Porosity morphology associated with the hydrogen level of the melt [88] (a) High hydrogen content: diffusion into bifilms starts in liquid (b) High-medium hydrogen content: high liquid fraction (c) Medium-low hydrogen content: growing in interdendritic structure (d) Low hydrogen content: not enough driving force to expand the bifilms .....	119
<b>Figure 2.13:</b> Schematic demonstration of entrainment of an inclusion [5] .....	119
<b>Figure 2.14:</b> Effects of alloying elements on hydrogen solubility in liquid Al at 973K, 1 atm partial pressure of hydrogen [36] .....	120
<b>Figure 2.15:</b> The relation between porosity, hydrogen and cooling rate[80].....	120
<b>Figure 2.16:</b> Porosity formation and intermetallics.....	121
a) nucleating on bifilm [174], b) nucleation on oxides [211], c) shrinkage and $\beta$ -phase[215] , d) $\beta$ -phase on oxide [105]	
<b>Figure 2.17:</b> Schematic representation of LiMCA [220].....	122
<b>Figure 2.18:</b> Schematic representation of PoDFA test [220].....	122
<b>Figure 2.19:</b> Schematic diagram of ultrasonic technique.....	122
<b>Figure 2.20:</b> Schematic RPT pparatus.....	123
<b>Figure 2.21:</b> bifilms and porosity formation [5].....	123
<b>Figure 2.22:</b> Schematic section of a 5t capacity Rotary Furnace (Size: 3 to 14 m <sup>3</sup> ).....	123
<b>Figure 2.23:</b> Schematic drawing of Tilt Rotary Furnace (Size: 3 to 14 m <sup>3</sup> ).....	124
<b>Figure 2.24:</b> 2.5t capacity Induction Furnace.....	124
<b>Figure 2.25:</b> different type of degassers (illustrated by air in water) bubble size and distribution in a) lance, b) rotary degassing head [236].....	125
<b>Figure 2.26:</b> different type of diffusers (illustrated by the use of air bubbles in water) stationary ceramic diffusers a) disc-type, b) T-type [237].....	125

<b>Figure 3.1:</b> (a) RPT machine and (b) schematic circuit drawing.....	126
<b>Figure 3.2:</b> a schematic representation of aluminium ingot production.....	126
<b>Figure 3.3:</b> schematically shown surface turbulence during fluxing and degassing.....	127
<b>Figure 3.4:</b> Dimensions of the holding furnace and location of diffusers.....	127
<b>Figure 3.5:</b> Schematic illustration of changes made at the casting trials.....	128
(a) - '1' The launder was lowered to be as close to the casting mould possible	
- '2' The casting and filling speed were decreased	
(b) - '3' More care was taken to avoid the severe turbulence on tapping	
<b>Figure 3.6:</b> Sand moulds that were used in RPT .....	129
a) resin binder,	
b) sodium silicate + coal dust mixture; and metal samples cast in the moulds	
c) an outer view (50x35x15 mm);	
d) a section through the centre.	
<b>Figure 3.7:</b> Pattern design: (a) core box, (b) dimensions.....	130
<b>Figure 3.8:</b> a) sand particles adhered on surface of RPT sample,	
b) better surface finish with addition of coal dust.....	130
<b>Figure 3.9:</b> Schematic diagram of tensile test piece mould showing the dimensions of the optimised mould.....	131
<b>Figure 3.10:</b> Tensile test bar dimensions used for mechanical tests.....	131
<b>Figure 3.11:</b> Real time X-Ray studies with different gating designs; entrapment of bubbles and severe turbulence was observed (dark regions are gaps and white regions are liquid metal in the marked points).....	132
<b>Figure 3.12:</b> Schematic illustration of mould fillings taken from real time X-Ray studies(Figure 3.11) Left row: Different patterns, Right Row: same pattern as left row but with filters placed under sprue (dark regions are liquid metal and white regions are air entrapment and gap).....	133
<b>Figure 4.1:</b> RPT sample density change with hydrogen (solidified at 100 mbar –alloy LM4).....	134
<b>Figure 4.2:</b> density index change at 100 mbar –alloy LM4.....	134
<b>Figure 4.3:</b> RPT sample density change with hydrogen (solidified at 10 mbar –alloy LM4).	135
<b>Figure 4.4:</b> density index change at 10 mbar –alloy LM4.....	135
<b>Figure 4.5:</b> density index variation at different pressures –alloy LM4.....	136
<b>Figure 4.6:</b> Sectioned surface of the reduced pressure test samples cast at moulds with different binder contents (alloy LM4).....	137
<b>Figure 4.7:</b> theoretical density-hydrogen relationship at different vacuum levels.....	138
<b>Figure 4.8:</b> comparison of theoretical relationship of density change with hydrogen from RPT samples obtained at different vacuum levels –alloy LM4	
(a)1000 mbar, (b)200 mbar, (c)100 mbar, (d)50 mbar, (e)10 mbar .....	138
<b>Figure 4.9:</b> different morphology and size of pores in RPT sample at different vacuum levels and casting temperatures.....	141
<b>Figure 4.10:</b> schematic bursting of bubbles from the surface.....	142
<b>Figure 4.11:</b> Examples of bursting shown from sectioned surfaces of the reduced pressure test samples at 10 mbar .....	142
<b>Figure 4.12:</b> SEM images of inside the pores of RPT samples (LM4).....	142
<b>Figure 4.13:</b> EDS analysis of roughened areas shown in Figure 4.12.....	144
(a)Some thick oxides gave only Al and O peaks	
(b) In some cases Mg, Si and Cu phases under the thin oxide were detected	
<b>Figure 4.14:</b> density-hydrogen relationship at different vacuum levels; LM0 melt at 750°C	145
<b>Figure 4.15:</b> Sectioned surfaces of 99% Al (LM0) samples cast at 750°C: clean and unclean melts (200 mbar, 100 mbar, 50 mbar).....	146

<b>Figure 4.16:</b> SEM pictures of LM0: oxide covered surfaces inside the pores (a) young oxides, (b) old oxides.....	146
<b>Figure 4.17:</b> Alloy LM27: degassing studies with high gas flow rate and low gas flow rate (50 and 100 mbar).....	147
<b>Figure 4.18:</b> fluxing and degassing with different diffusors (alloy LM4 - 50 and 100 mbar)	147
<b>Figure 4.19:</b> The predicted bubble distribution with different diffusors.....	147
a) lance: coarse and few bubbles,	
b) disc type ceramic: finer and more bubbles,	
c) T-type ceramic: finer and evenly distributed	
<b>Figure 4.20:</b> density-hydrogen relationship at different casting levels (LM24); a) 50 mbar, b) 100 mbar .....	148
<b>Figure 4.21:</b> histogram of density of the RPT samples (LM24) (a) 50 mbar, (b) 100 mbar .....	149
<b>Figure 4.22:</b> the effect of casting height and bifilms on the pore morphology (LM24).....	150
<b>Figure 4.23:</b> SEM images inside the pore (LM24).....	150
a) bottom filled: fragments of a bifilm in between dendrites,	
b) top poured: close up of an internal crumpled oxide	
<b>Figure 4.24:</b> The density change of the reduced pressure test samples cast at different heights (alloy LM25 – 100 mbar).....	151
<b>Figure 4.25:</b> The density histogram of the reduced pressure test samples cast at different heights (alloy LM25).....	151
<b>Figure 4.26:</b> Sectioned surface of the reduced pressure test samples cast at different heights (alloy LM25; RPT 100 mbar).....	151
<b>Figure 4.27:</b> Density change of RPT samples (100 mbar) from start, mid to end when running:(a) 0 diffuser, (b) 1 diffuser, (c) 2 diffusers.....	152
<b>Figure 4.28:</b> Density of RPT samples comparing different number of diffusers (100 mbar)..	152
<b>Figure 4.29:</b> The density of RPT samples comparing the different techniques (100 mbar)... (a) 0 diffuser, (b) 1 diffuser, (c) 2 diffusers (SET 1: non-quiescent conditions, SET 2: quiescent conditions)	153
<b>Figure 4.30:</b> X-RAY images of some of RPT samples .....	154
<b>Figure 4.31:</b> Schematic illustration of sectioning of RPT samples.....	155
<b>Figure 4.32:</b> shape factor change with the hydrogen level (LM4: RPT at 200 mbar).....	155
<b>Figure 4.33:</b> shape factor change with the hydrogen level (LM4: RPT at 100 mbar).....	155
<b>Figure 4.34:</b> shape factor change with the hydrogen level (LM4: RPT at 50 mbar).....	156
<b>Figure 4.35:</b> shape factor change with the hydrogen level (LM4: RPT at 10 mbar).....	156
<b>Figure 4.36:</b> shape factor change with temperature at different vacuum levels (LM4).....	157
<b>Figure 4.37:</b> average pore area with temperature and pressure (LM4).....	157
<b>Figure 4.38:</b> porosity % versus temperature and pressure (LM4).....	158
<b>Figure 4.39:</b> Porosity % versus density and pressure (LM4: at all temperatures).....	158
<b>Figure 4.40:</b> relationship between porosity %, hydrogen and pressure (LM4: at all temperatures).....	158
<b>Figure 4.41:</b> relationship between average pore area with hydrogen and pressure (LM4: at all temperatures).....	159
<b>Figure 4.42:</b> average pore area change with density (LM4: at all temperatures).....	159
<b>Figure 4.43:</b> alloy LM4: (a) shape factor change with density at different vacuum levels (b) shape factor distribution .....	160
<b>Figure 4.44:</b> quality index ( $QI_2$ ) change with the RPT density (Alloy LM4) (a: $QI_2=5$ , density= $2600 \text{ kg/m}^3$ , b: $QI_2=1$ , density= $2700 \text{ kg/m}^3$ ).....	161
<b>Figure 4.45:</b> quality index ( $QI_2$ ) change with the density (Alloy LM24); Comparison of different castings heights (a) 100 mbar, (b) 50 mbar.....	161
<b>Figure 4.46:</b> Concept of $QI_3$ change with density .....	162

<b>Figure 4.47:</b> $QI_3$ change with density - data from experiments (LM4).....	162
<b>Figure 4.48:</b> Bifilm index versus density at different vacuum levels (LM4) (all temperatures).....	163
<b>Figure 4.49:</b> Bifilm index versus density at different vacuum levels (LM4) (a) 700°C, (b) 800°C, (c) 900°C.....	163
<b>Figure 4.50:</b> Bifilm index versus hydrogen at different vacuum levels (LM4) (a) 700°C, (b) 800°C, (c) 900°C .....	164
<b>Figure 4.51:</b> Bifilm index versus hydrogen at different vacuum levels (LM4) (all data from Figure 4.50 superimposed here on the same graph).....	164
<b>Figure 4.52:</b> Bifilm index versus density as a function of casting height; LM24 (a) 100 mbar, (b) 50 mbar.....	165
<b>Figure 4.53:</b> Weibull distribution change of bifilm index of different casting heights (LM24).....	165
<b>Figure 4.54:</b> Bifilm index versus density; LM25 (100 mbar).....	166
<b>Figure 4.55:</b> Weibull distribution change of bifilm index of different casting heights (LM25 - 100 mbar).....	166
<b>Figure 4.56:</b> Bifilm index versus density (LM24-100 mbar).....	167
<b>Figure 4.57:</b> Bifilm index (determined at 100 mbar) change from start, mid to end Comparing different number of diffusers (LM24).....	168
<b>Figure 4.58:</b> Comparison of bifilm index change (determined at pressure 100 mbar) between non-quiescent (SET 1) and quiescent conditions (SET 2) (a) 0 diffuser, (b) 1 diffuser, (c) 2 diffusers.....	168
<b>Figure 4.59:</b> Weibull distribution change of bifilm index of different casting conditions .... (LM24 -100 mbar) (a) Non-quiescent conditions (SET 1) (b) Quiescent conditions (SET 2)	169
<b>Figure 4.60:</b> The relationship between the number of pores and bifilm index (determined at pressure 100 mbar).....	170
<b>Figure 4.61:</b> Schematic illustration of sectioned surface of RPT samples illustrating the relationship between the number of pores and bifilm index.....	170
<b>Figure 4.62:</b> The relationship between bifilm index (determined at 100 mbar) and hydrogen content of the melt.....	171
<b>Figure 4.63:</b> Change in the average air gap between bifilms with temperature.....	171
<b>Figure 4.64:</b> Comparison of Weibull distribution of tensile properties developed under conditions of quiescent and non-quiescent fillings: Alloy LM27 (a) UTS, (b) elongation.....	172
<b>Figure 4.65:</b> Comparison of Weibull distribution of mechanical test results of bars obtained by machining of ingots and by re-melting and casting into test bars, Alloy LM4. (a) The Weibull plot of UTS and (b) the Weibull plot of elongation $e$ .....	173
<b>Figure 4.66:</b> Sectioned surface of RPT samples alloy LM2 (100 mbar) (a) High Mg, (b) Low Mg .....	173
<b>Figure 4.67:</b> Alloy LM24 Weibull distribution change of two different casting heights showing (a) UTS, (b) elongation .....	174
<b>Figure 4.68:</b> Alloy LM2 (low Mg) Weibull distribution change of two different casting heights showing (a) UTS, (b) elongation.....	175
<b>Figure 4.69:</b> Alloy LM2 (high Mg) Weibull distribution change of two different casting heights showing (a) UTS, (b) elongation.....	176
<b>Figure 4.70:</b> Alloy LM2 (Bottom Filled): Weibull distribution change of different Mg content (a) UTS, (b) elongation values .....	177
<b>Figure 4.71:</b> Alloy LM2 (Top poured): Weibull distribution change of different Mg content (a) UTS, (b) elongation values .....	178

<b>Figure 4.72:</b> Alloy LM2 (Top poured): Weibull distribution change of different Mg content (a) UTS, (b) Elongation .....	179
<b>Figure 4.73:</b> SEM pictures from the fracture surface of tensile test bars (LM24 – low Mg)..	180
<b>Figure 4.74:</b> SEM pictures from the fracture surface of tensile test bars (LM24 – high Mg)	181
<b>Figure 4.75:</b> LM24 comparison of distribution of tensile properties at the start of casting with and without filter (a) UTS, (b) Elongation .....	182
<b>Figure 4.76:</b> Alloy LM24: Comparison of the Weibull distributions of strength and elongation at the start and end of casting (a) UTS, (b) Elongation .....	183
<b>Figure 4.77:</b> Relationship between bifilm index (100 mbar) and tensile properties of LM24 and LM2 alloys (a) elongation, (b) UTS .....	184
<b>Figure 4.78:</b> Bifilm index (100 mbar) change with .....	185
(a) Weibull modulus of elongation values, (b) Weibull modulus of UTS values (the lines are drawn by software as a best-fit)	
<b>Figure 5.1:</b> Semi-quantitative predictions of melt cleanliness [246].....	186
<b>Figure 5.2:</b> Sample density and hydrogen relationship of 319 (LM24).....	186
for various melt treatments (100 mbar)[246]:(a) untreated, (b) grain refined, (c) modified	
<b>Figure 5.3:</b> The effect of holding time and temperature on pore morphology in alloy LM4 at 10 mbar RPT .....	187
<b>Figure 5.4:</b> Schematic representation of the ratcheting action (a) air gap between original bifilm (b) hydrogen diffuses or pressure may change to cause the pore to expand, increasing the area of its oxide film (c) oxygen in the air gap between the bifilm oxidizes and fixes the new enlarged bifilm area, preventing its return to its original size.....	187
<b>Figure 5.5:</b> As bifilms are carried from top to bottom of the melt by EM stirring action, they open and close under the cycling metallostatic pressure .....	188
<b>Figure 5.6:</b> Schematic image of a shrinkage pore in 3D and resulting 2D image [129].....	188
<b>Figure 5.7:</b> Hydrogen measurement throughout a sequence of test.....	189
(a) 2different tests from studies with LM4 (b) 3different tests from studies with LM24	
<b>Figure 5.8:</b> Comparison of LaOrchan’s RPT result [240] with the current work.....	189

## List of Tables

<i>Table 2.1: Summary of factors affecting porosity formation in aluminum castings .....</i>	<i>190</i>
<i>Table 2.2: Techniques for oxide detection and measurement [18] .....</i>	<i>192</i>
<i>Table 2.3: Specification of the alloys that are used in the experiments.....</i>	<i>193</i>
<i>Table 2.4: Similar alloy specifications.....</i>	<i>193</i>
<i>Table 2.5: Application area of alloys.....</i>	<i>193</i>
<i>Table 3.1: Composition of the alloys that were used in the experiments .....</i>	<i>194</i>
<i>Table 3.2: RPT test matrix followed in the laboratory .....</i>	<i>194</i>
<i>Table 4.1: Weibull modulus of bifilm indices of different alloy and casting conditions....</i>	<i>195</i>
<i>Table 4.2: Coordinates of points shown in Figure 4.61 .....</i>	<i>195</i>
<i>Table 4.3: Chemical analysis change from start to end of casting 2.5 ton melt of LM24 from holding furnace .....</i>	<i>195</i>
<i>Table 4.4: Mechanical test results and Weibull Modulus of alloys LM2 and LM24 .....</i>	<i>196</i>

# CHAPTER 1

## INTRODUCTION

“*Knowing your enemy*”, probably the first step to success in a battle. In castings, defects in microstructure determine the characteristics of an alloy; therefore, it is important to understand these defects and their formation mechanisms.

The usage of aluminium and its alloys have increased in many applications and industries over the decades. The automotive industry is the largest market for aluminium castings and cast products. Aluminium is widely used in other applications such as aerospace, marine engines and structures. Parts of small appliances, hand tools and other machinery also use thousands of different aluminium castings. The applications grow as industry seeks new ways to save weight and improve performance. However, another aspect has become of critical importance: the achievement of quality and reliability of the products. Therefore, in the past decade, developments have focused on quality factors that affect the properties of aluminium.

In a product, the properties are influenced by melt treatment, casting technique, solidification mode and microstructure. Solidification is the stage at which the microstructure is formed. Segregation and hot tearing are among the kind of defects that can occur during solidification. However, this is not the topic of this study. This thesis considers defects that are formed at the melting stage and during the handling of the melts in a casting process. All these processes occur before the stage of solidification. Undoubtedly, any defect present or created at the melting stage could be carried to the final microstructure (unless, perhaps, filters are used), effectively adding to any solidification defects, and will, of course, affect the component's life. Therefore it is apparent that the control of the quality of the product begins with the control of the quality of the melt.

At present, there is no single quality test that is capable of identifying and classifying the most serious defects that can exist in aluminium alloy melts. These defects, which have been held responsible for potential failure mechanisms, are dissolved hydrogen and the entrained aluminium oxide, in the form of defects known as ‘*bifilms*’.

The standard reduced pressure test (RPT) appears to be able to provide an indication of metal quality but has so far resisted quantification, being used, at best, as a comparative assessment. It involves the solidification of two small samples of melt, one at atmospheric pressure, and the other under a partial vacuum. A comparison of the densities of the samples is then used to give a numerical indication of melt quality. However, as will be shown in this work, this approach is not at all reliable, and furthermore, the RPT is unable to distinguish between hydrogen content and metal cleanliness. It is important to address this issue because of the recognition that hydrogen porosity cannot nucleate (either homogeneously or heterogeneously as we shall see) without the presence of bifilms. For the first time, evidence will be presented later in this study for the contribution of air (or perhaps more strictly, residual nitrogen from air) as an additional gas, adding to hydrogen in pores in cast Al alloys.

Early studies have assumed that hydrogen would always nucleate without difficulty so that there would be a linear relationship between the density of a sample and its hydrogen content. Therefore, simply by measuring the density at any stage of a process this would give an indication of the hydrogen content. However, the reality of the situation is that bifilms are the initiator and hydrogen is only a contributor in the formation of porosity.

Earlier studies were also conducted at laboratory scale allowing only relatively few data to be collected. In the scope of this work, for the first time, data have been collected in the industrial environment of a secondary remelter company, allowing hundreds of different experiments and thousands of data to be collected. In this way the test was uniquely authenticated both statistically and experimentally.

The aim of this work was first to develop the RPT into a quantitative (or at least semi-quantitative) analysis technique for determining the metal quality in aluminium melts and then to correlate the metal quality with the mechanical properties.

Although the research aims to make a number of contributions towards developing a quantitative method to describe the metal quality in detail we need to first establish exactly what is meant by the “enemy!” In addition, the term ‘*quality*’ is taken up as a challenge to establish a definition. These matters are reviewed in Chapter 2.

Then, in Chapter 3, the experimental study is presented which includes demonstration of the reduced pressure test where the issue of porosity phenomena was investigated. Once the operation of the reduced pressure test was established in the laboratory, the test machine was transported to the industrial environment to obtain larger data sets for a wide range of different alloys in different conditions. For instance, melts were sampled both before and after metal treatments such as fluxing, degassing and filtration. The unique feature of this exercise was that it provided for the first time thousands of results, not easily achieved in a laboratory, that constituted a stringent test of the usefulness of the concepts.

In Chapter 4, the results of these discourses and experiments will be analyzed with reference to Campbell's recently introduced concept of bifilms. This concept appears to be capable of building our understanding of metal quality in detail, allowing us to develop a quality index that will further assist foundrymen to produce high quality castings.

The interpretation of results and evaluation, as well as evolution of metal quality, are addressed in Chapter 5, illustrating the coherence of the concepts introduced in this work.

Finally, Chapter 6 presents the conclusions.

## CHAPTER 2

### LITERATURE SURVEY

Jules Verne, "From the Earth to the Moon", 1865;  
The aluminium capsule is being shot into space (Chapter 7):

*"Employ another metal instead of iron"*

*"Copper?" said Morgan*

*"No! That would be too heavy. I have better than that to offer."*

*"What then?" asked the major.*

*"Aluminium!" replied Barbicane.*

*"Aluminium?" cried his three colleagues in chorus.*

*"Unquestionably, my friends. This valuable metal possesses the whiteness of silver, the indestructibility of gold, the tenacity of iron, the fusibility of copper, the lightness of glass. It is easily wrought, is very widely distributed, forming the base of most of the rocks, is three times lighter than iron, and seems to have been created for the express purpose of furnishing us with the material for our projectile."*

No doubt that with all the excitement and scientific success in the 20<sup>th</sup> Century, with the remarkable properties such as its light weight, strength, recyclability, corrosion resistance, durability, ductility, formability and conductivity, aluminium has become a valuable material. Due to this unique combination of properties, the variety of applications of aluminium continues to increase. Today more aluminium is produced each year than all other non-ferrous metals combined.

It is these distinctive properties why aluminium has been predominantly associated with aerospace and automotive industries. The driving force for improved properties, lower production cost and greater strength/weight ratios together with demands such as reduced pollution, improved fuel efficiency and increased performance have helped aluminium alloy castings replace iron-based alloys in many automotive applications.

Today, significant amounts of aluminium alloys are being cast to produce components. The automotive industry is the largest market for aluminium castings and cast products make up more than half of the aluminium used in cars. Main products include engine blocks, cylinder heads, suspension control arms, front strut supports, wheels, and pistons. The volume of cast aluminium components is projected to grow significantly in the next decade [1].

There is growing evidence [2-12] that, in general, aluminium castings under-perform by a large margin. This is not only because of shrinkage or gas porosity, but particularly because of the existence of extremely thin but detrimental defects called bifilms. Bifilms may or may not become sufficiently open to become visible as porosity, but appear to be the ultimate challenge in today's aluminium castings. Porosity, and probably unwittingly, bifilms, have been held responsible for many failures in products - low mechanical properties, low fatigue properties and reduced elongation.

Considerable effort has gone into understanding and controlling defects that are formed in aluminium and its alloys during casting. This study furthers this effort, focussing on quality of the liquid metal during processing from the beginning (alloy manufacture) to the end of production (casting). The results of some laboratory scale studies together with a series of tests carried out in a commercial secondary remelting operation will be demonstrated. First, this literature survey starts with some brief information about the history of casting aluminium.

## **2.1 History of Casting and Aluminium**

A casting may be defined as a "metal object obtained by allowing molten metal to solidify in a mould," the shape of the object being determined by the shape of the mould cavity. So the process begins by melting the metal, blending the alloy, and finishes after pouring it into moulds. As can be recognized from the definition, casting is essentially a simple, inexpensive, and versatile way of forming so it is not surprising that it was historically the first method used. Even today, casting continues to be the most widely used method of forming. Technical advances, of course, have been made, but the principle remains the same: molten aluminium is poured into a mould to replicate a desired pattern.

Although it is not known who made the first casting, or exactly where, most historians believe that this great step forward was made in ancient Mesopotamia in the period of 4000-3000 BC. The oldest casting in existence is believed to be a copper frog cast in Mesopotamia probably around 3200 BC, and its complexity indicates clearly that it was preceded by simpler objects. It also has been claimed that cast gold objects were found in royal tombs of the first dynasty of Egypt dating back to 4000 BC [13].

Progress in casting was necessarily slow. From pure copper, early man moved to bronze. In the years following 3000 BC, the metal casting process was a vital element in both art and the production of military hardware. Then came tin, zinc, and brass. Shortly after 1000 BC, the first production of cast iron is attributed to China. Developments in metal casting came swiftly in the 14<sup>th</sup> and 15<sup>th</sup> centuries after all the improvements in moulding practices. Clearly sand casting had largely displaced earlier clumsier methods of obtaining a metal shape. The available casting techniques were constantly improved upon as the industrial revolution gained momentum [13].

The development of casting practices for aluminium and its alloys is a relatively recent accomplishment. Aluminium alloys were not available in any substantial quantity for casting purposes until long after the discovery in 1886 of the electrolytic process of reduction of aluminium oxide by Charles Martin Hall in USA and Paul Heroult in France [14]. Although Hall's invention provided aluminium at a greatly reduced cost, the full value of aluminium as a casting material was not established until alloys suitable for the foundry process were developed. Since about 1915, a combination of circumstances - gradually decreasing cost, the expansion of air transportation, development of specific casting alloys, improved properties, and the impetus provided by two world wars - has resulted in an ever-increasing use of aluminium castings [15].

### ***2.1.1 Casting Processes***

Metal casting processes can be classified either by the type of mould or pattern, or by the pressure or force used to fill the mould with molten metal. Conventional sand, shell and plaster moulds often utilize a permanent pattern, but the mould is used only once. Permanent

moulds otherwise known as dies are machined in metal, graphite or other specially selected die matrix material and are used for large volume production castings. Investment casting and the lost foam process involve an expendable mould as well as an expendable pattern [16].

One of the most versatile methods is sand casting. Virtually any pattern can be pressed into a fine sand mixture to form a mould into which the aluminium can be poured. This is by far the highest productivity of any casting process, and highly economical. Variants of the process are also suitable for small quantities, intricate designs and one-off and large castings.

Some of the main advantages of the casting process can be given as follows:

1. Most intricate shapes both internal and external may be cast.
2. Because of their nature, some metals can only be cast since they cannot be shaped by other methods.
3. Construction may be simplified. A number of separate items in an assembly can sometimes be integrated to be cast as a single piece.
4. Highly adaptable to mass production.
5. Extremely large, heavy metal objects may be cast that would be difficult and/or economically impossible to produce otherwise.
6. Some engineering properties are obtained more favourably in cast metals: in general a wide range of alloy compositions and properties is produced in cast form, and the properties available are generally isotropic.
7. Generally low cost.

Aluminium is one of the most versatile of the common foundry metals, with cast products consuming, as a world average, some 20% of this metal. Its light weight is the one most commonly cited advantage. Apart from that, the special advantages of aluminium alloys for castings are the relatively low melting temperatures, negligible solubility for all gases except hydrogen, and the good surface finish that is usually achieved with final products. It can exhibit a wide range of mechanical properties (strength, hardness, and other properties may be greatly altered by alloying and/or heat treatment); architectural and decorative value; corrosion resistance; non-toxicity (cooking utensils, other food handling equipment);

electrical conductivity; ease of machining; lower shipping cost per piece. Most alloys also display good fluidity and compositions can be selected with solidification ranges appropriate to particular applications. However, a major problem with aluminium castings is the relatively high shrinkage of between 3.5 and 8.5% that occurs during solidification [17]. Other negative features include its high solubility to hydrogen in the molten state, the lack of resistance to abrasion and wear; inability to develop combination of high tensile strength, toughness and hardness as in ferrous alloys; lack of resistance to severe corrosion (compared to copper and stainless steel) [15].

## 2.2 Metal Quality

One of the challenges faced by the foundry technologist and researchers is to obtain a consistent quality. Therefore extensive efforts have been made to produce quality products from various alloy systems meeting the demanding mechanical behaviour.

There are three important features that define metal quality: control of trace elements, reduction of dissolved gas, and removal of non-metallic inclusions. Inclusions in the aluminium alloy act as stress-raisers, and can cause premature failure of a component [18-20]. Oxide particles and films are often the most common inclusions observed within aluminium melts. The oxides arrive in the melt right from the start of melting. They arrive as oxide skins on the surface of the material to be melted. When remelted in a crucible furnace, or other type of bath of molten metal, as each piece of solid charge is submerged and melts, its surface oxide floats free and becomes suspended in the melt. Such films are finally found as complete, massive, film-like or dross-like inclusions in finished castings [5].

The presence of these defects, as well as gas or shrinkage porosity formed during solidification, can make properties unpredictable and significantly affect the mechanical properties of aluminium castings [9, 21, 22], especially the ductility and fatigue properties [2, 3, 23-28].

Since the significant expression in the definition of casting is the use of liquid metal to give the shape of the object directly, the primary quality factor begins with the control of the melt.

As indicated above, the liquid metal may gain a significant amount of oxide from the melting process. However, even more may be added if the melt is handled poorly, particularly if it is violently stirred or is poured. The experimental studies in this thesis show later how these mechanical handling issues can introduce additional oxides. Ultimately, however, if during the final casting operation the melt is handled carefully, quiescently, then there will be no reason why a defect should form. However, of course, the melt itself will often already contain a population of defects, unfortunately introduced during its previous processing that would normally have included one or more pouring stages.

During melting, important interactions that occur between an aluminium melt and its environment include the absorption of hydrogen and the formation of oxide films. Hydrogen dissolves readily in liquid aluminium but is much less soluble in the solid state and may therefore form porosity if it is rejected from solution during solidification. The free energy of formation of alumina is such that it is impossible to prevent its formation at exposed liquid aluminium surfaces. In fact, the alumina film is an important part of the melting process, simply because it protects the metal underneath from further oxidation, or even, as in the case of molten magnesium, combustion. However, the problem begins when an oxide film is pushed into, or otherwise entrained, in the melt. These entrainment events are surface folding actions in which two non-wetting surface films will come into contact with gas trapped between them (Figure 2.1). This constitutes a defect that will act exactly like a crack in the liquid and is known as a 'double oxide film' defect or a 'bifilm' [5]. As a result, the potential for introducing defects into aluminium castings begins at the melting stage where hydrogen gas and oxide films become incorporated into the melt.

### ***2.2.1 The Dissolution of Hydrogen***

The majority of light metals and alloys in their molten condition are inclined to considerable adsorption of gases. The gases absorbed by the surface of the metal are capable of diffusing into the metal in the atomic state [29]. Oxygen, nitrogen and other gases form chemical compounds on the surface of the liquid metal, however hydrogen appears as the principal gas that can be taken into solution in the bulk liquid.

Hydrogen, on account of the small volume of its atom, diffuses more rapidly than other gases in liquid metals. The investigations [30-33] showed that diffusion through an alumina film is accomplished in the following stages:

1. Dissociation of the molecular hydrogen
2. Development of activated adsorption on the oxide surface
3. Release of hydrogen from the adsorbed layer and its passage into true solution
4. Movement of the dissolved hydrogen through the crystal lattice
5. Passage of hydrogen into the absorbed layer on the opposite side of the film
6. Desorption of atoms of hydrogen
7. Transport by advection of the bulk liquid.

The main source for hydrogen results from the dissociation of water vapour. Fluxes, crucibles, refractories and charge materials all usually contain some moisture which will add hydrogen to the melt. Water vapour may be readily found in the atmosphere, especially on hot and humid days. The reactions involved are



As seen in Figure 2.2, the solubility of hydrogen in pure aluminium decreases with decreasing temperature [32, 34-40]. This decreased solubility of hydrogen in the solid phase can result in the precipitation of hydrogen gas, which may cause porosity. However such precipitation requires suitable conditions, of course, otherwise the hydrogen is forced to remain in solution, in a supersaturated state (Figure 2.3).

### ***2.2.2 Formation of Oxide Film***

With the exception of pure gold, no pure metal and no alloy are stable in air at room temperature. All metals and alloys tend to react with air to form oxides and/or nitrides [41].

As the temperature increases, the oxidation or nitridation rate increases (with the exception of Ag). In this study only oxidation is considered.

Since in their molten state, many metals and alloys exhibit a solid surface film of oxide, the oxidation of liquid metal in various atmospheres plays an important role in melting and casting operations. Many of the problems that arise in these operations originate from oxidation.

For solid metals, the oxide films which form on the metal may protect it from further oxidation [41], and at the same time may influence the dissolution and release of hydrogen. Pilling and Bedworth, from an investigation of the process of oxidation of metals, established that the protective action of the film may be determined by the ratio of the molecular volume of the oxide to the atomic volume of the metal contained in the compound. If this ratio is greater than unity, a dense continuous film is formed; if this ratio is less than unity, a discontinuous film is formed; that is:

$$\frac{w_o d_M}{W_M d_o} > 1 \quad \text{continuous film} \quad (2.3)$$

$$\frac{w_o d_M}{W_M d_o} < 1 \quad \text{discontinuous film} \quad (2.4)$$

$W_{o/M}$ : the molecular weight of the oxide/metal

$d_{o/M}$ : density of the oxide/metal

In the case of liquid metals the liquid would adjust its surface area infinitely to accommodate changes if its surface was a liquid. However, as we know, the surface of most liquid metals already has a solid oxide in place. Thus when the new solid forms on top of the existing solid, and volume and/or length changes are required, one or both of the phases has to give way. Such behaviour has been observed many times during the growth of multi-layered oxides on solid metals [42-45], and would be expected to occur similarly during multi-layer growth of films on liquids.

In the formation of a continuous protective film, the rate of oxidation is limited by the diffusion of atoms of oxygen through the film, and will decrease with time according to a parabolic law [41]. With discontinuous films, the oxygen will penetrate, not by diffusion, but principally through breaks in the film, and the rate of oxidation is likely to increase according to a linear law [29].

For pure aluminium, because it is so very reactive with oxygen, oxidation starts by the rapid formation of an amorphous alumina layer within milliseconds, where the film grows by outward diffusion of aluminium ions [46-57]. This amorphous oxide film has a high impermeability to the diffusion of aluminium and oxygen ions; thus, the film forms a protective layer over the molten aluminium. Because they are entrained quickly and have little time to grow, amorphous films are referred to as '*young oxides*' [58]. They are characterised by extreme thinness, usually measured in tens of nanometers.

After an incubation time the amorphous oxide layer suffers a discontinuous change of structure. A fast migration of oxygen through the oxide-metal interface occurs at high temperature, resulting in a nucleation and growth of  $\gamma\text{-Al}_2\text{O}_3$  crystalline phase under the amorphous layer [44, 45, 47, 48, 59-62]. The incubation for this transformation is normally around 5 to 10 minutes at  $750^\circ\text{C}$  [58] and is reduced by increased temperature and increased inclusion content in the melt [63]. During this period the films have time to thicken, becoming often micrometres or even millimetres thick. These thicker oxide films, referred to as '*old oxides*' [54] are characterised by their crystalline form.

Continued exposure of these films to temperatures at which the melt is held causes a final transformation from  $\gamma$  to  $\alpha\text{-Al}_2\text{O}_3$  [47, 48, 59]. This transformation occurs naturally with the reaction of water vapour with the aluminium melt where hydroxyl ion removal proceeds by the absorption of hydrogen into the melt. After crystallization, the film grows inward by diffusion of oxygen through the crystalline oxide layer [54-57]. Reducing the water vapour pressure in the environment enhances the ease of transformation further, and results in a more rapid conversion of  $\gamma\text{-Al}_2\text{O}_3$  to  $\alpha\text{-Al}_2\text{O}_3$ . During this transformation the 24% decrease in volume of the oxide (which occurs due to the structure and morphology change in oxide from

cubic spinel  $\gamma\text{-Al}_2\text{O}_3$  to rhombohedral  $\alpha\text{-Al}_2\text{O}_3$  [49]) results in fracture of the oxide which leads to breakaway oxidation [42, 44-46, 48-51, 53, 62, 64].

In the case of alloys, the nature of the oxides formed depends on the melt composition. The alloying elements such as iron, copper, zinc and manganese have little effect on this oxidation process. However, in the presence of approximately 0.005 wt% of magnesium, the surface oxide is the mixed oxide  $\text{MgO}\cdot\text{Al}_2\text{O}_3$  also known as spinel [5, 44, 58-62, 64-70]. When the magnesium content of the alloy is raised above approximately 2%, then the oxide film is expected to be pure magnesia,  $\text{MgO}$  (Figure 2.4).

Several studies [42, 44, 46, 49, 59-62, 64-66, 68-75] showed that this rapid degradation of the initial amorphous  $\text{Al}_2\text{O}_3$  surface to a less protective oxide film consisting entirely of  $\text{MgO}$  or of both  $\text{MgO}$  and  $\text{MgAl}_2\text{O}_4$ , is explained by two possible mechanisms. The first mechanism is explained by the observation of two compositionally different layers: an outer layer of  $\text{MgO}$  and an inner layer of  $\text{Al}_2\text{O}_3$  doped with small amounts of magnesium [44, 46, 62, 64, 67]. Although both magnesium and aluminium have high affinities to oxygen, the formation of the oxide layer is not only controlled by thermodynamics. The growth is time dependent, and related to such kinetic factors as the diffusion rate of metal cations and/or oxide anions through the oxide layer. Thus, the presence of an outer  $\text{MgO}$  layer strongly suggests that during the initial thickening of amorphous  $\text{Al}_2\text{O}_3$  layer,  $\text{Mg}^{+2}$  ions diffuse through the amorphous  $\text{Al}_2\text{O}_3$  layer more rapidly than  $\text{Al}^{+3}$  ions (Figure 2.4).

The second mechanism is described by the nucleation of  $\text{MgAl}_2\text{O}_4$ .  $\text{Mg}$  oxidation kinetics is controlled by  $\text{Mg}$  diffusion through the oxide layer defects [61]. Evidently, because of its high vapour pressure, magnesium evaporates and ruptures the continuous film, altering its protectiveness [64]. Therefore, local pathways occur where oxygen is transported through the channels as well as the breakaway oxidation paths. When the magnesium concentration at the melt-oxide interface falls to below a critical level, localised nucleation and formation of  $\text{MgAl}_2\text{O}_4$  are favoured by preferential breakaway oxidation.

### 2.3 The Concept of Surface Entrainment: Bifilms

In contrast to all the problems that are created by the surface films, the molten aluminium can actually benefit from this oxide skin. Because of the protective nature of the alumina that is formed on the surface, the oxidation cannot continue further down into the melt. Therefore it is important to keep in mind that the oxide only begins to be a problem when the surface film is submerged [5]. During this action, a single oxide cannot be submerged alone. It has to be folded. Since the film is grown from the melt, the underside is in atomic contact however the top surface will be crystalline. Therefore, during the folding action two film surfaces will be brought into contact. These surfaces of solid oxide will of course have zero bonding between them (Figure 2.1). This bifilm will act as a crack in the liquid. During turbulent filling, handling, transfer or pouring, the melt may become filled with huge density of these cracks [76].

Campbell [76-78] has shown that this surface entrainment occurs if the velocity of the liquid exceeds a critical value. The critical value corresponds to that speed at which the metal can just reach the height of a sessile drop. It can be shown:

$$V_{critical} = 3.5 \left( \frac{\gamma}{r} \right)^{1/4} \quad (2.5)$$

Where  $\gamma$  is surface tension,  $r$  is density. This critical value has been shown both theoretically and experimentally to be approximately 0.5 m/s for liquid aluminium [5].

It is all the more curious as quoted by Campbell [77] that “for many thousands of years any action which resulted in the folding-in, or submergence of the surface, was not widely appreciated as a potential source of major problems for castings made from such metals.”

### ***2.3.1 Incorporation of Surface Films into Melts***

Cleanliness of a molten aluminium alloy is a function of the type and amount of bifilms present. There are various mechanisms by which these cracks can be incorporated into castings [5].

For example, the oxide skin of the charged metal is automatically incorporated during melting. During handling or transfer of the liquid metal, the surface of the liquid may be broken due to surface turbulence (Figure 2.1). During the pouring, at higher speeds and heights, dross can be carried under the surface together with entrained air (Figure 2.5). Because of the geometry of a casting, the metal stream may separate and rejoin together at some distant location. This rejoining of the advancing film fronts may form a bifilm (Figure 2.6).

### **2.4 Compacting and Unfurling (ravelling and unravelling) of Bifilms**

The entrainment process of bifilms was described previously as folding action and two halves coming together to become incorporated into the melt. However, the bifilms could ravel into small compact features by the internal turbulence created in the melt. Therefore their size could be reduced approximately 10 times from their original size. In this form they could be relatively harmless [76]. However, during solidification, they could unravel back to their original starting shape to form a planar crack. The possible mechanisms that could assist this type of an action can be summarised as follows:

1. hydrogen precipitation in the air layer between the films
2. shrinkage, reducing the pressure acting on the films
3. iron precipitation in the form of beta phases
4. large grain size, encouraging extensive rafts of dendrites to straighten the films by an inclusion pushing action.

The loss of ductility observed as a result of hydrogen porosity, shrinkage porosity, iron levels, and large grain size, all occur mainly as a result of the action in opening the compact convoluted bifilms [79].

In this thesis, the precipitation of hydrogen in between the bifilms, straightening and inflating the double film, is a central feature of the study.

## 2.5 Porosity Phenomena

### 2.5.1 Nucleation

Pore formation is assumed to obey the laws of nucleation and growth [5, 80-82], the formal theory of which is analogous to the theory of the nucleation of a solid from the liquid (Figure 2.7). The process consists of the following:

1. The presence of hydrogen atoms within the liquid pool (because of segregation, as the solidification front advances, the hydrogen content in the liquid is concentrated ahead of the front)
2. The formation of sub-critical embryo pores
3. Pores having the radius above the critical size continue to grow (as long as hydrogen atoms are available)

Following the approach of Fischer [82] for homogeneous nucleation, a quantity of work is associated with the formation of a bubble in the liquid. The formation of a pore of volume  $V$  requires work equal to  $p_e V$ , meaning that porosity has to push back the liquid far enough to create a bubble of volume  $V$ , where  $p_e$  is the pressure of the liquid. The formation and stretching out of the new liquid-gas interface of area  $A$  requires a work of  $\gamma A$ , where  $\gamma$  is the interfacial energy per unit area  $A$ . The work required to fill the bubble with gas at pressure  $p_i$  is negative and equal to  $-p_i V$ , because pressure inside the bubble clearly helps the formation of the bubble [5]. Assuming the bubble to be spherical in shape and of radius  $r$ , the total work is:

$$\Delta G = \gamma A + p_e V - p_i V \quad (2.6)$$

$$\Delta G = \gamma A + \Delta p V$$

$$\Delta G = (4\pi r^2)\gamma + \left(\frac{4}{3}\pi r^3\right)\Delta p$$

$$r^* = -\frac{2\gamma}{\Delta p} \quad (2.7)$$

where  $r^*$  is the critical radius for the homogeneous nucleation of a bubble, below which it is not capable of surviving and above which it will tend to grow (Figure 2.7),  $\Delta p$  is the pressure difference inside the pore and  $\gamma$  is the surface tension of the liquid.

In castings, the nucleation of pores can be expected to occur primarily at heterogeneous sites. Heterogeneous sites are inherent in almost all liquids, with inclusions forming the most important category of such sites in the melt. Since oxides and other non-metallic inclusions are not wetted by the metal, the microscopically rough surfaces with free cavities serve as nuclei for bubbles to grow. It has been well demonstrated that the presence of inclusions and oxides greatly enhances the porosity formation in aluminium alloys [83-89].

The energy relationship between homogeneous and heterogeneous nucleation is given by [5]:

$$\frac{P_{het}}{P_{hom}} = 1.12 \left( \frac{(2 + \cos \theta)(1 - \cos 2\theta)}{4} \right)^{1/2} \quad (2.8)$$

where  $P_{het}$  and  $P_{hom}$  are the pressures required for heterogeneous and homogeneous nucleation, and  $\theta$  is the contact angle between the solid particle and the liquid, which defines the extent of wetting:  $\theta = 0^\circ$  means wetting whereas  $\theta = 180^\circ$  means complete non-wetting (Figure 2.8). As seen from Figure 2.8 and Equation 2.8, as the wetting angle decreases, the ratio of  $P_{het}/P_{hom}$  goes to unity which is the wetting condition that is homogenous nucleation. This corresponds to greatest difficulty for the nucleation of a pore. The nucleation becomes even harder on a well wetted surface than in the bulk liquid, because there are fewer atomic sites on a surface compared to the bulk.

### 2.5.2 Growth

During solidification, dissolved atomic hydrogen in excess of the low solid solubility, may tend to associate to the molecular state if embryonic pores are available, forming bubbles. The content of atomic hydrogen at which pores will form is known as the ‘threshold hydrogen content’. This will only occur if the equilibrium hydrogen pressure is sufficiently high:

$$p_g + p_s > p_a + p_m + p_{st} \quad (2.9)$$

Here,  $p_g$  is equilibrium pressure of dissolved gas in the melt,  $p_s$  is pressure drop due to shrinkage which helps the formation of porosity,  $p_a$  is atmospheric pressure of system,  $p_m$  is pressure due to metallostatic head ( $\rho_Lgh$ ),  $p_{st}$  is pressure due to surface tension ( $2\gamma/r$ ).

When the pressure inside this homogeneously or heterogeneously nucleated gas bubble is greater than the sum of the variables ( $p_a, p_m, p_{st}, p_s$ ) in Equation 2.9, then the growth of a pore is favoured [86, 89-107]. In other words, porosity will grow if the pressure difference across the embryonic bubble surface, with positive pressure from hydrogen gas inside, and negative pressure created by shrinkage on the outside, exceeds the restraining pressure due to surface tension. Even in the most favourable case that can be imagined, however, the nucleation and growth of a bubble is unlikely because of the huge difficulty of nucleation, whether homogeneous or heterogeneous: the small size of the embryonic bubble means that the pressures involved are enormous, in the range of gigapascals. Thus it is unlikely that supersaturations of hydrogen, nor tensile stresses due to shrinkage, will be sufficient to achieve the nucleation condition.

### 2.5.3 The New Approach to Pore Formation

In cast aluminium products the occurrence of low mechanical properties has traditionally been assigned to the presence of porosity: both macro and micro. The usual interpretation is that microporosity results from (i) an incomplete liquid metal feeding which leads to volumetric shrinkage, and (ii) reduced solubility of hydrogen upon solidification. For this reason, there

has always been an attempt to control shrinkage and gases in metals in an effort to reduce the formation of porosity.

Tremendous efforts, including theoretical, mathematical and analytical approaches have been made over the past decades to understand the porosity problem in aluminium castings with a view to providing a remedy. A summary of recent studies [108-156] on porosity formation in aluminium castings is shown in Table 2.1. The size, the shape, the location, the amount of pores that would be formed was aimed to be calculated prior to castings. However, in most of the cases the predictions have corresponded poorly with the experimental results. Unfortunately, researchers have not satisfactorily explained the reasons why.

It was the classic and pioneering experiment by Brondyke and Hess in 1964 [157] that demonstrated that a sample of liquid aluminium which solidified to give a porous solid, when passed through a filter gave a sound solid. This was a first indication that pore formation required the presence of foreign inclusions in the melt. The implication of this finding was that clean liquid metals could withstand considerable stress without the formation of porosity [78].

The statistics of the mechanical failure of castings, and the direct observation of the filling of castings using real-time X-ray radiography had actually demonstrated for the first time the association between surface turbulence and the creation of porosity [78]. Recently, for the first time, these bifilms, acting as cracks, have been observed in liquid aluminium alloys by Fox [158-160]. Using the reduced pressure test technique, he manipulated the conditions during freezing so that the cracks opened sufficiently to be recorded by radiography. This work corroborated the theory that folded oxide skins introduced into the melt were somehow related to the porosity in castings. Taking this recent work in consideration, a detailed investigation on the reduced pressure test was aimed to resolve this issue in this work. Therefore, the hypothesis and the starting point of study was that bifilms that are introduced into the melt could be the '*primary*' cause of porosity in castings.

It has been recognised that the homogeneous nucleation of pores in liquid aluminium would require extremely high gas contents and shrinkage pressures of the order of 30,000

atmospheres (Equation 2.7) [161, 162]. Thus, the homogenous nucleation of pores is in principle difficult and is unlikely to occur in practice. Although the energy required for heterogeneous nucleation is  $1/20^{\text{th}}$  of that of homogenous nucleation (Figure 2.8 b) [5], 1500 atmospheres is still too high to be reached in a usual solidification process. It follows that the occurrence of porosity in cast metals has presented an intractable problem, simply because, in theory, porosity cannot be nucleated. The predictions of the classical atomic models are, at best, probably overestimating the difficulty of initiating pores by at least two orders of magnitude. It seems from general experience that pore initiation in castings almost certainly occurs at stresses less than this. As it happens, in the words of Campbell [5] “the opening of a bifilm involves negligible force, being so easy that it can be assumed that this process will be overwhelmingly favoured, and making irrelevant all the conventional assumptions of homogeneous or even heterogeneous nucleation. As a result, for the initiation of all porosity, whether gas or shrinkage, and whether in conditions that are well fed or unfed, or high gas or well degassed levels, it is assumed that bifilms are the initiation source”. For the first time, evidence for this theory will be demonstrated and experimental findings that support this approach will be shown in the results of this work.

## 2.6 Porosity Types

Porosity formation in aluminium alloys can be classified as follows:

- according to size:
  - a. macroporosity
  - b. microporosity
  
- according to cause:
  - a. shrinkage
  - b. gas
    - (i) precipitated from solution in bifilms during solidification
    - (ii) mechanically entrained by surface turbulence
    - (iii) mechanically blown into the melt (as, for instance, for a core blow).

These categories are not hard distinctions, but they do provide a starting point for an introduction. Apart from the bubble damage arising from pouring and mould filling, classification according to cause will be discussed briefly, because hydrogen is the major contributor of porosity in aluminium alloys.

Since nucleation is not possible in a casting free from bifilms, there is no remaining mechanism for pore formation. In case of the presence of bifilms, then the growth of the pores can be controlled by two mechanisms (inspired by Whittenberger [163]):

- *with feeding*: if there is enough feeding, in which any reduction in environmental pressure around the bubble is negligible compared to the metallostatic pressure, then the rate is controlled by the rate of gas deposition alone into bifilms
- *without feeding*: average growth rate is controlled by shrinkage rate (controlled by the rate of solidification of course) and deposition of hydrogen in combination.

The rate of gas deposition is controlled by a diffusion process, therefore increasing the freezing rate reduces the time available, and so reduces total volume of gas porosity. It has to be kept in mind that a porosity-free casting does not necessarily mean a bifilm-free casting.

### ***2.6.1. Shrinkage Porosity***

Basically, shrinkage porosity arises because of the density difference between the solid and liquid alloy phases. As solidification proceeds, the volume diminishes and surrounding liquid flows in to compensate. Depending on the amount and distribution of solid, the fluid flow may be impeded or even completely blocked. When sufficient liquid cannot flow in, the solid may flow in (a process known as solid feeding, and is essentially the plastic collapse of the casting by a creep process at the high temperatures involved). If neither liquid nor solid can feed the shrinkage, a large internal tensile stress develops that may be sufficient for voids (pores) to form. This shrinkage porosity can be either small-distributed pores or one large pore.

Out of five possible feeding mechanisms (Figure 2.9), interdendritic feeding is considered to be the one of the most difficult stages for the creation of porosity defects. Particularly in long freezing range alloys, feeding becomes progressively more difficult due to the decreasing size of the channels (Figure 2.10). Eventually, the channel freezes completely and isolates small areas from the supply of fresh metal. At this stage only solid feeding remains, the solid collapsing plastically to compensate for the volume deficit.

### ***2.6.2. Gas Porosity***

The basic concept driving the precipitation of hydrogen during solidification is the solubility difference of hydrogen in the solid and in the liquid. Since it is low in the solid, some of the gas will be rejected from solution during solidification. The rejected gas diffuses into the bifilms (into the porosity inside or actually initiated by the bifilms) and expands the central gap. The consequent expansion of the bifilm may be constrained in the restricted spaces between the growing dendrites, so that they become irregular, gas-filled cavities with the characteristic “interdendritic” shape as seen in Figure 2.11a. These types of pores are sometimes erroneously identified as shrinkage pores. Depending on the fraction of eutectic phase, these cavities may also appear “round” (Figure 2.11b) [164-167]. This depends on the mode of freezing, whether planar or dendritic.

## **2.7 Factors Affecting Porosity**

Piwonka and Flemings [108] have studied porosity formation. The aim of their work was to examine analytically the general problem of pore formation in solidification and to perform limited confirmatory experiments. They concluded that shrinkage and microporosity result from:

- the pressure drop difference arising from resistance to flow,
- the solidification mode where hydrogen diffusion is associated, and
- the initial hydrogen content of the melt.

Their work inspired many investigators to calculate the porosity [27, 91-101, 103-105, 110-119, 144, 145, 151-154, 168-187]. After these investigations, other factors such as chemical composition, solidification range, volumetric shrinkage, cooling rate, heat extraction, grain structure and the presence of oxides and inclusions were found to influence gas porosity formation. Gathering this information together, the factors that increase the likelihood of porosity formation are described in the following sections.

### ***2.7.1 An increase in hydrogen content of the melt***

The initial hydrogen concentration in the melt is one of the most important factors influencing the amount of porosity formed. At low initial concentrations, pores form late and they are usually small (Figure 2.12 c-d). At high initial concentrations (Figure 2.12 a-b), pores start to form in the early stages of solidification and grow much larger [86, 91, 92, 101, 103, 106, 116, 127, 134, 143, 151, 169, 188].

### ***2.7.2 An increase in the Entrained (exogenous) inclusion content***

The content of the entrained inclusions is one of the foremost important factors because the non-wetted (microscopically rough) surfaces already constitute the initiation site (the growth point) for hydrogen diffusion and pore growth [83-86, 88, 89, 157]. The only way inclusions can be entrained (i.e. included in the liquid by being introduced through its oxide-covered surface) is being wrapped by the surface oxide film [5] as seen from Figure 2.13. In this way the inclusion is generally surrounded by an adherent layer of air trapped inside the thin oxide skin. It is therefore a good initiation site for expansion by hydrogen precipitation.

### ***2.7.3 Oxide structure***

Pure aluminium is a soft ductile metal, but by alloying with other elements, the physical and mechanical properties can be substantially changed. Typical alloying elements are copper, magnesium, silicon, zinc, titanium and iron. One of the important aspects of alloying in the oxidation process is passivation by the growth of a protective oxide. However, alloy

modifications can alter the oxide structure. For instance, when strontium is present in the melt,  $\text{SrO}\cdot\text{Al}_2\text{O}_3$  forms, which is less protective than amorphous  $\text{Al}_2\text{O}_3$  [84, 128, 138, 189-192]. Similarly, magnesium addition alters the oxide film from  $\text{Al}_2\text{O}_3$  to spinel  $\text{MgAl}_2\text{O}_4$  or to  $\text{MgO}$  which is also weaker [44, 46, 59, 62, 66, 70, 193, 194]. During these transformations, hydrogen gas may also be introduced into molten metal (Equation 2.2), if moisture is present in the environment. Therefore as the rate of gas pickup at the surface is increased, together with increased oxidation, porosity will increase.

### ***2.7.4 Alloying***

Grain refiners are added to alloys to increase the strength and toughness by changing the microstructure, especially to a smaller grain size. However, these changes also alter large pores to smaller discrete pores. But it has been recognised [102, 106, 119, 127, 130, 133, 142, 190, 191, 195-198] that this alteration of the microstructure only alters the size of the pores but not the number of pores. In addition, some elements shift the eutectic temperature, while others may affect the hydrogen solubility in aluminium (Figure 2.14) [35, 36, 199, 200].

### ***2.7.5 Cooling rate***

Increasing the solidification velocity reduces the time for diffusion of hydrogen [95, 106, 130, 167, 169, 170, 181, 190, 195, 198, 201-204] into the bifilms. Eventually, porosity will decrease (Figure 2.15).

### ***2.7.6 Intermetallics***

Although the iron content in Al-Si alloys is at an impurity level, it plays an important role in the mechanical behaviour of the alloy. Relatively large amounts of iron are soluble in liquid aluminium (in excess of 2 wt%) but the solubility in the solid at its freezing point is only about 0.005 wt%. Because of this low solid solubility, the segregation ratio of iron is high. The great increase of iron at the freezing front encourages the formation of iron-rich intermetallic phases. These intermetallics nucleate on oxide films [83, 126, 164, 165, 205-

209] present in the liquid metal. Furthermore, because of their morphology, as the intermetallics grow they tend to unfurl bifilms [164, 165], changing them from compact ravelled defects to large planar cracks. Iron phases have traditionally been blamed for fractures in Al alloys because they were thought to be brittle. Actually it appears that the bifilms on which iron phases nucleate are responsible for the fracture since, of course, they constitute cracks in the solid (Figure 2.16).

## 2.8 Measurement of Metal Quality

The dissolution of hydrogen gas in liquid aluminium has been assumed to be a significant issue for the production of high quality castings. Clearly, it seemed that reliable measurement of the hydrogen content in the melt was required. This led to the development of many techniques.

Early attempts to determine the hydrogen content started in the 1950s. Several techniques based on solidification under reduced pressure have been tried [38, 39, 210-213] where the densities of the small samples solidified under vacuum were measured, and comparison with the theoretical density was related to the amount of hydrogen evolved. The technique was commendably robust and low cost, but quantitative assessment of the gas in solution to any degree of accuracy and reliability has remained elusive.

Currently, methods such as RPT (Reduced Pressure Test), NOTORP, Alscan, Hyscan, Telegas are used to determine hydrogen content, which have developed from early attempts in 1950s. The principle of most of these methods is basically as follows: a gas ( $N_2$  or Ar) is circulated through the liquid by a probe. When hydrogen equilibrates with the carrier gas, the partial pressure or activity of the hydrogen is measured giving the hydrogen content. This fundamental technique is complex, delicate, expensive and slow.

## ***2.8.1 Inclusion Detection Techniques***

Over the years, a number of test methods have been developed for inclusion detection in liquid aluminium (Table 2.2), but the general experience in the casting industry has been that these were usually slow, inappropriately complicated and/or expensive for use on the foundry floor. The main approaches are listed below.

### *2.8.1.1 LIMCA (Liquid Metal Cleanliness Analyser)*

A measurement is made of the electrical potential across a small hole (diameter 0.05 to 0.10 mm) through which a sample of liquid is forced to flow (Figure 2.17). The approach is one of the few inclusion detection techniques that is continuous in action, and so can monitor quality of metal flowing in a launder for instance [214]. Naturally this technique is limited to inclusions that can enter the hole. The inclusions that are seen to be important in the technique described in this present work are in range from 1 to 10 mm diameter as will be described. Thus the most important inclusions cannot be detected by the LIMCA test.

A further development of LIMCA in which the voltage drop across a tube of perhaps a fraction of a mm in diameter is monitored clearly had in mind the detection of minute, compact spheroidal inclusions. The approach remains curiously inappropriate for up to 10 mm diameter film-type inclusions.

### *2.8.1.2. PoDFA – PREFIL (Porous Disc Filtration Analysis)*

Both the PoDFA and PREFIL tests involve the passing of the melt through a fine filter. The filter and its deposit can be subsequently sectioned and the inclusions identified by metallographic techniques. The interpretation of the metallographic sections is a highly skilled and lengthy operation, and not easily quantified [214]. However, for PoDFA the rate of blockage of the filter is an additional measure of cleanness (Figure 2.18). The samples required for a reliable result are generally in the range of approximately 2 kg. The technique

requires a certain degree of skill; otherwise the filter can block prematurely and give a poor result.

Techniques using filtration (pore size in micrometres) cannot detect nanometre thick films, nor are the techniques expected to be sensitive to their presence since they are not structurally rigid and so wrap around the filter structure so closely that they will remain undetectable even in carefully polished metallographic sections.

### *2.8.1.3. Ultrasonic*

A number of interesting attempts have been made to monitor reflections from inclusions in the melt using ultrasonics. The method can be clearly used on single samples or continuously (Figure 2.19). Signals can be obtained and counted, but seem to correspond to inclusions of size only up to 0.1 mm diameter [18]. This is possibly because ultrasonic techniques will be expected to receive echoes from crumpled areas of films, giving the appearance of groups of small reflectors instead of one large, but not very flat, film.

### *2.8.1.4 Summary of Quality Assessment Techniques*

Thus all of our current sophisticated techniques for inclusion detection and monitoring give cause for concern. In addition, the accuracy of some of the techniques has to be questioned when alumina films often exceed 10 mm across, but are only nm thick.

Thus all major techniques for the assessment of the quality of melts tend to measure either hydrogen or inclusion content. In addition many of the techniques have become highly sophisticated and therefore involve expensive hardware and software. However, as mentioned before, hydrogen alone is not the major factor reducing quality; it is actually the combination of hydrogen and bifilms together that plays the effective role.

### 2.8.2. *Reduced Pressure Test (RPT)*

Having carried out this critique of the techniques for quality assessment of liquid aluminium alloys, in contrast to other quality assessment techniques, the Reduced Pressure Test (RPT) was regarded as having the best potential for development. It was simple and rugged, and sensitive to both gas and inclusion content, particularly double oxide films.

The Straube-Pfeiffer vacuum solidification test, giving the RPT the full name of its German originators, has been generally denigrated as a result of its failure to be a reliable hydrogen test. In fact, however, it has always been a good test of the *porosity potential* of the melt. Interestingly, the humble RPT is precisely what is required to meet the required conditions for the effective control of porosity, since, as we have noted previously, we need to monitor both inclusions and hydrogen content. Either alone is insufficient.

In addition to being fundamentally appropriate, the test is easy, robust, simple, low cost, and relatively quick, assessing the effect of both detrimental defects: (i) hydrogen and (ii) entrained inclusions, or perhaps more explicitly, bifilms.

The test simply consists of solidification under a reduced pressure (Figure 2.20). The reduction of pressure serves to magnify the effect of dissolved gas on the opening of bifilms. The schematic illustration is given in Figure 2.21. For instance, if the pressure is reduced to 1/100<sup>th</sup> of an atmosphere, it is expected that the residual air layer between the films would be expanded by approximately 100 times, thus converting an essentially invisible defect into one that is visible on an image produced by X-ray radiography, and to the unaided eye on a polished section.

The popularity of the RPT as currently widely used in the industry lies in the relative simplicity and inexpensive nature of the test. One major disadvantage is, however, that it is not quantitative. Nevertheless, it becomes possible to identify the size, shape, type and distribution of non-metallic inclusions in the final product which can be seen on a polished cross section of the reduced pressure test. These can be used by the cast shop as the 'fingerprints' of the melt. Thus even in its simplest qualitative form, the test is useful.

## 2.9 Secondary Remelting – Recycling

Recycling of metals has become an essential part of a sustainable industrial society economically, technically and ecologically. For these reasons, the process of recycling has become of great importance where each metal has its own recycling method. Besides the valuable metals such as gold, the recycling of aluminium has grown to a great extent [1, 215-218].

Materials that are discarded during the manufacturing and fabrication of aluminium and its alloys, and materials that are recovered when an aluminium article has been produced, used and finally discarded at the end of its useful life, are generally defined as scrap. Such material includes used beverage cans, car cylinder heads and blocks, window frames from demolished buildings and old electrical conductors. The recycling of all these is carried out by secondary aluminium refiners or remelters [1].

Secondary aluminium refiners convert most of their materials into foundry ingot, generally based on the aluminium-silicon alloy system with additions of other metals such as copper and magnesium. These ingots, formulated according to recognised national or international specifications (Table 2.4), go into the manufacture of aluminium cast components. The application area of alloys is given in Table 2.5. A significant share of the secondary aluminium refiners' output is also delivered in a molten form by road tanker to large foundry users thus eliminating the need for further melting operations [1, 215-218].

One of the most important factors in recycling aluminium is that remelting saves up to 95% of the energy needed to produce the primary product. Another important factor is that the majority of used aluminium can be recycled, which makes it highly valuable. Today recycled aluminium accounts for one-third of aluminium consumption world-wide [1].

Naturally, the recycling process does not consist simply of gathering scrap and remelting it, usually into bars or ingots for subsequent re-melting by the casting industry. The quality of the recycled material has to be of a sufficient standard to make adequate castings. It is well known by casters that the remelting industry turns out, inadvertently, different qualities of

ingot from plant to plant, and, unfortunately, also can vary from a single plant on a melt to melt basis.

With a view to attempting to understand the factors that are of major importance in the control of quality, a typical secondary remelting process includes:

1. Sorting of scrap into alloy types
2. Centrifuging and drying to reduce contaminants such as oil and water.
3. Magnetic separation of iron.
4. Melting.
5. Fluxing and degassing to remove inclusions, oxides and dissolved gases.
6. Pouring into a holding furnace
7. Chemical analysis and adjustment of analysis if necessary.
8. Transferring to casting unit via a launder (a refractory lined open channel)
9. Casting into bars or ingots on an automated casting machine.

## ***2.9.1 Melting***

### *2.9.1.1 Rotary Furnace*

A common method for the melting of aluminium is the use of a rotary furnace [218-220]. This starting point for recycling consists of a cylindrical, refractory lined steel drum, supported by a structural steel frame. The furnace is heated by a natural gas flame that burns along the axis of the drum (Figure 2.22). These furnaces are efficient melters because of their action in rotating the heated roof refractory under the melt for direct contact, together with a good mixing action. Once preheated, flux and feed material are charged into the furnace. The natural gas burner is then positioned in the melting chamber and the furnace rotated. The molten metal is then discharged to a holding furnace or to the casting area.

### *2.9.1.2 Tilt Rotary Furnace*

The tilt rotary furnace works in the same way as the rotary furnace, the major difference being the horizontal tilting action so that the initial feeding of scrap, charge, salts and the final casting is done from the same door giving an advantage of high yield and low maintenance cost (Figure 2.23).

### *2.9.1.3 Electric Furnace*

The principle of operation of the induction furnace is the phenomena of inducing electrical current in the charge by means of a alternating magnetic field supplied by an induction coil that surrounds the crucible (Figure 2.24).

The key advantage of induction heating is its speed; melting as a result of the Joule heating from the induced current. In addition, of course, the unit is free from significant polluting effluents, and gives a working environment that is relatively cool and safe.

## **2.9.2 Fluxing**

When melting and handling molten aluminium alloys, foundries must combat the formation of dross, non metallic inclusions and oxide build up. The difficulty in remelting aluminium alloy swarf and light scrap is that these materials have a large active surface area that can become further oxidised during heating.

To overcome these problems, the process relies on fluxes. A flux is a material (often based on a chloride or fluoride) added to molten metal that unites with impurities to form a dross or slag, which rises to the surface of the metal and can be removed by skimming. Fluxing is a useful means of obtaining clean metal, preventing excessive oxide formation, removing non metallic inclusions from the melt and removing oxide build-up from furnace walls [221, 222].

In general fluxes can be broadly categorized as passive or active. Passive fluxes protect the surface of the molten bath from oxidation and prevent hydrogen pick up by the melt. Active fluxes react chemically with the aluminium oxide and clean melt more effectively [221, 222].

The role of inclusions in aluminium is of great importance in that every aspect of quality is affected by the presence of these second phases. Thus during processing operations, attention should be paid to mitigate the formation of inclusions, and as importantly, to remove those which are already present in the melt.

### *2.9.3 Degassing*

There are many sources of hydrogen during the melting and preparation of aluminium: atmospheric humidity, grain refiners, fluxes, damp tools, scrap, and the products of combustion. These factors along with the normal atmospheric oxygen, also contribute to the formation of oxides and inclusions.

Bubbling an inert gas through a melt of aluminium reduces the amount of undesirable hydrogen. Hydrogen is removed from the melt by its diffusion into the degassing bubbles as a result of the difference in partial pressure between the melt and the gas [156, 223-227].

Factors that influence the diffusion of hydrogen into the degassing bubbles are [223]: i) the area of contact surface between the gas and the melt, and ii) the contact time between the gas and the melt. For this purpose, different types of degassers are used as shown in Figures 2.25 and 2.26.

The ceramic diffusers [228, 229], for example, promote the efficient elimination of included hydrogen in less processing time than with open-ended tubes, because of the smaller size of bubbles and consequently greater area of bubble surface that is generated. In addition, they have advantages such as resistance to aluminium attack, excellent resistance to thermal shock, longer life than graphite, non-wetting minimizes dross build-up, lower flow rate than graphite diffusers for equivalent degassing.

The degassing process also reduces non-metallic inclusions since they generally become attached to the rising bubbles (if surface energies are favourable (non-wetting)) and are subsequently skimmed from the surface. The inert gas (argon and/or nitrogen) bubbles bring about excellent stirring that assists in homogenising the temperature and chemical composition of the melt.

## **SUMMARY**

For critical applications, it is vital to produce high quality and reliable castings. The quality and reliability are largely threatened by the defects that may be present in the structure. Since the final microstructure is directly dependent upon the as-cast microstructure, it is essential to determine the defects that are formed during production.

Porosity, viewed as one of the most important factors of quality, has been generally held responsible for low mechanical properties (particularly fatigue and elongation). As a consequence, hydrogen has been believed to be main cause and source of porosity. However, the required energy for nucleation of porosity (either homogeneously or heterogeneously) is extremely difficult to achieve during solidification. In contrast, the folded oxide skins introduced into the melt by turbulence, namely 'bifilms,' serve as sites into which hydrogen can precipitate, and shrinkage can cooperate, to expand the defects without difficulty.

The RPT is a simulation of the common condition inside a casting, where the effects of shrinkage and gas act in combination to grow porosity; the application of the vacuum additionally cooperating to expand the gap between the bifilms. This accurate simulation makes it the perfect test of the quality of the melt.

In the following chapters, the work on the reduced pressure test covered in the scope of this study will demonstrate the stages of quantification of metal quality. The evaluation and development of the quality index, which was established through an extended study in laboratory together with various conditions tested in a secondary remelter, will be exhibited.

## CHAPTER 3

### EXPERIMENTAL PROCEDURE

#### 3.1 Alloys

In this study, a number of commercially available British Standard LM series Al-Si based alloys were used. Their compositions are given in Table 3.1. These alloys feature good castability, reasonable strength, reasonable fatigue performance and corrosion resistance, and are widely used for automotive products.

#### 3.2 Reduced Pressure Test (RPT)

A schematic drawing of the RPT machine is shown in Figure 3.1. Basically, the equipment consists of a vacuum chamber and a rotary pump. The vacuum can be adjusted by a regulator. A digital display shows the elapsed time under vacuum. The principle was given in detail in Section 2.8.2.

In each experiment, three sets of tests were carried out. Two samples were poured into sand moulds; the first sample solidified in air under atmospheric pressure, the second solidified under a vacuum. The third sample was used for determining the hydrogen level of the melt with a Severn Science HYSCAN machine.

Two subsequent experiments were implemented. Once the reduced pressure test had been established in the laboratory, the test machines were transported to a commercial secondary remelter to sample larger melts of a wide range of different alloys. Sampling was carried out both before and after metal treatments such as fluxing, degassing, transfer of melt and at the casting stage.

### ***3.2.1 Laboratory tests***

Initially, a series of preliminary tests was done to determine the optimum test conditions. LM4 ingots weighing about 6-7 kg that were obtained from same batch of melt, were melted using standardised conditions in an induction furnace (2250 Hz, 15 kW, 500 V, open air, clay-graphite crucible, melted within 10-15 minutes). Samples for RPT were taken from the melt by a 100 g ladle (that was coated with BN and pre-heated above the melt for a few minutes), at melt temperatures of 700°C, 800°C and 900°C. The samples were solidified at different levels of pressure from 1 atmosphere down to low vacuum pressures (1000, 200, 100, 50, 10 mbar absolute pressure). The test matrix is given in Table 3.2. The purpose of this test was to examine the effect of temperature and pressure on the density of samples, thus providing an assessment of susceptibility to pore formation.

In the second test, a simple experiment was carried out with 99% Al (LM0) to see the effects of bifilms. A clean melt (melted in a 200 kg capacity resistance furnace) was carefully prepared by carrying out 3 fluxing and degassing operations using a rotary flux/degasser. After that, RPT samples were taken at 750°C, using great care to avoid as far as possible any introduction of surface oxide. Subsequently the melt was stirred, mixed, and poured from a height of approximately 1 m to ensure that bifilms were introduced, and then RPT samples were taken again.

### ***3.2.2 Industrial tests***

The steps of a typical secondary remelting process are shown schematically in Figure 3.2. The material was melted in an electric furnace (750°C). Fluxing and degassing (via a 25 mm bore steel tube which was plunged into the melt as seen in Figure 3.2) was carried out to remove inclusions, oxides and dissolved gases. Prior to casting, the melt was transferred to a holding furnace. From here, the melt was carried by launders (approximately 1 m long in L-shape and not preheated) to the casting area where ingots weighing 6-7 kg (dimensions of 50 x 60 x 550 mm) were poured.

In this particular secondary smelting operation, there were two 2500 kg electric induction melting furnaces, one 5000 kg rotary melting furnace (gas fired) and one 5000 kg capacity rotary-tilt furnace (also gas fired) (Figures 2.22-2.24).

In the electric furnaces the melt was treated by adding fluxing salts onto the surface of the melt, and then lancing with nitrogen gas. After treatment, the dross that had accumulated on the surface was skimmed off. In the rotary and rotary-tilt furnaces, the fluxing treatment was automatically accomplished by the rotating action of the furnace (Figure 2.22, 2.23) because melt and flux were in constant contact in the rotating furnace. Therefore the recovery rate (i.e. the metallic yield) of these types of furnaces is higher compared to induction furnaces. Also, of course, as noted earlier, the constant rotating of the preheated roof under the melt provides for efficient heat transfer.

During all these operations (fluxing, degassing, transferring), the surface oxide film breaks, re-oxidises and is submerged, introducing bifilms into the melt. For this reason the quality of the melt was assessed at each step of the process (after melting, following fluxing and degassing, and after the melt is transferred to holding furnace, prior to casting). RPT samples were taken to investigate the metal quality and to define the potential for defect formation at each stage.

One of the initial studies was carried out in the electric furnaces with alloy LM27. During fluxing and degassing via the tubular steel lances two different gas flow rates were compared:

- (i) A conventional rate (about 20 l/min) with the gas tap from the nitrogen cylinder fully open. This rate caused severe disturbance to the surface of the melt (Figure 3.3). In addition, the so-called inert gas used to carry out the degassing operation can never be truly inert, so that its content of oxygen and water vapour further contribute to the generation of oxides.
- (ii) A rate of approximately 2 l/min, resulting in the surface of the melt being hardly disturbed. In this second study, a T-type and a disc-type ceramic diffuser (Figure 2.26)

were used to investigate the efficiency of fluxing and degassing compared to the lance system with LM4.

A third study involving degassing was performed in the holding furnace with alloy LM24. This time, two diffusers were sited at the bottom of the holding furnace. The position of the diffusers and the dimension of holding furnace are given in Figure 3.4. Three conditions were tested; both off, one on and one off, and both on. In the second part of this same study, three changes were made in the casting area. These are summarised in Figure 3.5. The rate of the removal of the stopper at the tap hole (at the exit of holding furnace) was controlled slowly such that the turbulence at the launder was minimised (Figure 3.5b '1'). This helped the liquid to flow slowly in the launder, in turn the filling of the liquid in the mould was controlled quiescently (Figure 3.5a '2'). Finally, the launder was lowered close to the casting mould (Figure 3.5a '3'). This also helped the mould to be filled quiescently.

The next study was carried out in the casting area. Alloy LM24 was used to determine the effect of two different casting devices designed to transfer the melt from the launder into the ingot moulds. The details of these devices are confidential and cannot be described in details here, although the principal differences can be clearly stated. The first device involved a free fall from the launder of approximately 250 mm giving turbulent filling of the ingot mould. In this account ingots resulting from this technique will be referred as 'Top Poured'. The second device filled the mould from approximately 10 mm height without disturbing the surface, yielding ingots referred to as 'Bottom Filled'.

In the studies of material from the rotary furnace, because of the difficulty of sampling from inside the furnace itself, samples were only taken (i) after the melt had been transferred into the (stationary) holding furnace, (ii) from the launder from the holding furnace, and (iii) from the cast ingots.

### **3.3 Hydrogen Measurement**

The Severn Science Hyscan Hydrogen monitor was the main instrument used for the work. It measures hydrogen in molten aluminium using a reduced pressure technique. A constant mass

of the melt (100g) is placed in a chamber and the pressure reduced rapidly to a predetermined value (10 mbar) by a vacuum pump. The chamber and associated vacuum system are then isolated from the pump and the sample allowed to solidify. As the melt cools, hydrogen is released and its partial pressure is measured by a gauge whose output is converted continuously to a digital display of hydrogen content. The measurement accuracy of the hydrogen analyser is claimed to be approximately 0.01 cc/100g (0.1 mL/kg Al) and measurement time is less than 5 minutes per sample. The equipment was in calibration and a service is carried out regularly.

### 3.4 Moulds

For the RPT, sand moulds were used in order to produce a cast metal sample of 50 x 35 x 15 mm dimensions (Figure 3.6). Sand moulds were satisfactorily transparent to X-rays, and could easily produce a parallel-sided specimen that was convenient for radiography.

First, different binder contents and types were examined to determine their effect on samples. Resin bonded sand moulds were prepared using 60 AFS silica sand and a binder *Ashland Chemical* 5112 (50%) and 5230 (50%) precatalyzed *Pepset*<sup>TM</sup> resin. Total binder addition levels were 1.2 wt%, 2.4 wt%, 4.8 wt% and 9.6 wt%.

Preparation of the moulds was as follows: the sand and the binder were mixed for 2 minutes. Then, the mixture was packed in the core box. After approximately 15 minutes of curing the moulds were stripped from the box (Figure 3.7).

There was one issue in the use of resin bonded moulds: smoke and gas were evolved because of the binder's organic content. This threatened the contamination of the oil in the vacuum system. Therefore another commonly used inorganic binder,  $\text{NaSiO}_3$ , was examined. However, the lack of strength was a major disadvantage leading to breakdown of the moulds during casting. The bond between the filler grains consisted of silica gel. Under the action of gas pressure (that was used to cure the mould), some of the water was driven off causing the gel to shrink and cracks to develop. Preheating of the moulds after preparation further dried the bonds, so that the strength fell considerably below the original green strength. As a result

of this poor strength, adhering sand particles were observed on the surface of each sample (Figure 3.8a). Interestingly, it was found that addition of 2 wt% coal dust not only increased the strength of the mould but also resulted in a better surface finish with better shake-out properties. Because, in general, liquid metals poorly wet carbon, its deposition on the grains of sand forming the surface of mould produced an improved surface finish (Figure 3.8b).

Compared to the resin binder system, no gas or smoke was observed after pouring the melt into the silicate bonded moulds (despite their content of coal dust). It was a clean, safe process with no major environmental problems. As a result, advantages like its low cost and very short preparation time with no toxicity made the sodium silicate/CO<sub>2</sub> system an attractive method for moulding and it was therefore used for the rest of the tests carried out in the university laboratory.

### 3.5 Density Measurement

Principally, pore formation is enhanced by the applied vacuum in the RPT, therefore the melt quality may be related to the density of the RPT sample. For that reason, to be able to examine the effects of the test pressure on the amount of the porosity, the density of each sample was calculated according to Archimedes Principle (by weighing in air and in water):

$$d = \frac{m_{air}}{(m_{air} - m_{water})d_{water}} \quad (3.1)$$

$d$ : density of sample,

$m_{air}$ : weight in air,

$m_{water}$ : weight in water,

$d_{water}$ : density of water.

The weighing was done on a single pan electronic balance with 0.0001g sensitivity. A wetting agent was added to water for complete wetting of the sample and for ensuring a constant wetting angle on the support wire. The first reading was immediately recorded before

significant penetration of the water into internal cavities occurred, artificially increasing the apparent weight of the sample.

The corresponding density index was then also determined:

$$d_{index} = \frac{d_{air} - d_{vacuum}}{d_{air}} 100 \quad (3.2)$$

$d_{air}$ : density of the sample solidified under atmospheric pressure

$d_{vacuum}$ : density of the sample solidified under vacuum (RPT)

### 3.6 Image Analysis

An X-ray radiographic study was made on each sample at approximately 300  $\mu\text{m}$  resolution. After porosity observation, samples were sectioned (cut by a saw longitudinally into halves) and ground with 120, 400, 800 and 1200 grade papers. Images taken from the surfaces prepared in this way were digitized by a flatbed scanner with a resolution of 1200 pixels per inch (pixel spacing approximately 20  $\mu\text{m}$ ). Images were subjected to Image Analysis to calculate the area, length and shape factor of each pore. To test the accuracy of image analysis results, three different software packages were compared; Sigma Plot Scan Pro 5 (SPSS Inc.), Clemex (Clemex Technologies Inc.) and MCID (Interfocus Ltd.). The University of Birmingham had an agreement with SPSS Company so Sigma Plot was used for all the rest of the analysis carried out.

The term “pore %” used in figures represents the ratio of area of pores over the total area viewed on the sectioned surface of the RPT samples which is formulated as:

$$pore\% = \frac{\text{area of pores}}{\text{total area viewed}} 100 \quad (3.3)$$

Shape factor is an additional dimensionless quantity that was measured, and defined as

$$SF = \frac{4\pi(\text{Area})}{(\text{Perimeter})^2} \quad (3.4)$$

where a perfect circle will have a shape factor of 1. A shape factor of a line will approach zero.

### 3.7 Tensile Test

Ingots were sampled from the beginning, middle and end of production runs in the secondary remelting casting operation. As was described before, various production conditions were subjected to study. In particular, it was of interest to evaluate how the mechanical properties of the cast alloy changed throughout the pour, and as a result of changes in production conditions.

Unfortunately, it was not easy to check directly the tensile properties of the ingots. This would have involved much machining of soft, unheat-treated material, of poor grain size and porosity. Thus a remelting and re-casting procedure into more convenient conventional test bar forms was felt to be essential. Thus a check was carried out to ensure that the remelting and re-casting procedure used to ascertain the properties of the melts would in fact be adequately representative of the original ingot material.

The sample ingots were remelted in a clay-graphite crucible in an induction furnace in the University laboratory. No treatment of any kind was carried out; the melting was conducted with minimal disturbance to the metal. An RPT sample was taken from each melt to test the melt quality by measuring the bifilm content. Subsequently, test bar moulds (Figure 3.9-3.10) were poured. The procedure consisted of two sand moulds that were poured at 750°C from each remelted ingot, producing two castings each weighing approximately 2 kg and each producing 10 bars, giving a total of 20 test bars per sample ingot. The optimised design of the pattern of the test bar mould is shown in Figure 3.9.

Following the casting, tensile samples were machined using a CNC (Computer Numerical Control) to ASTM E 8-00 dimensions (Figure 3.10).

Naturally, it was essential that the cast test bars represented the quality of the sample ingots. It was important therefore to produce bars in which few defects were introduced during filling. Therefore the design of the tensile test pattern was first investigated to check that it filled without unnecessary turbulence, since it is known that turbulence could introduce unwanted defects that would confuse the results. The X-ray studies and schematic illustration of earlier trials for pattern design are given in Figure 3.11 and 3.12. As seen from the figures, the metal was unconstrained and so able to splash freely, without control, along straight runners of large area. A filter was placed under the sprue to slow the metal down. However, it generated bubbles even though the melt was slowed down. Thus it was highly likely that this design would have introduced defects into the cast test bars, so that the design was considered unsuitable. After some trials, a final revised design, constraining the flow within narrow runners, and provided with two right angle steps, was optimised in a video X-ray radiographic study which was given in Figure 3.9. It yielded a flow of apparently excellent integrity that proceeded steadily and without air entrainment.

LM2, LM6, LM24 and LM27 are alloys that are not normally heat treated, being used in the as-cast condition. Only LM4 and LM25 were heat treated before tensile testing. These samples were first heated to 520°C for 6 to 12 hours and water quenched into water at 60°C. Samples were then artificially aged at 170°C for 16 hours.

The tensile machine used was a *Zwick* 1484. Samples were loaded in the same orientation for each test. The accuracy of the load cell was 0.1 N. The crosshead speed was 1 mm/minute. Data from the load cell and extensometer were digitally recorded at 1 data point every 0.005 mm. The extensometer gauge length used was 25 mm.

### **3.7.1 Weibull Analysis**

A Weibull analysis [230] was carried out from the set of tensile test results. The values were plotted as ln-ln plot of failure probability versus log property. The resulting slope of the graph

is termed “The Weibull Modulus”,  $m$ . This is a measure of the variability of the property being measured. The probability of failure,  $F$ , as a function of stress,  $S$ , is given by:

$$F(S) = 1 - e^{-\left(\frac{S}{S_o}\right)^m} \quad (3.5)$$

$S_o$  is called the characteristic strength (i.e. the stress level at which approximately 63% of the specimens have failed) and  $m$  (the Weibull Modulus) is a constant that characterises the spread of the failure data with respect to the  $S$  axis. A high Weibull modulus is desirable since it indicates an increased homogeneity and less spread in the flaw population and a more predictable failure behaviour. Linear regression is used to determine the model parameters, where  $m$  is now simply the slope of the graph:

$$\ln\left(\ln\left(\frac{1}{1-F(S)}\right)\right) = m \cdot \ln(S) - m \ln(S_o) \quad (3.6)$$

### 3.8 Microscopy and Microanalysis

Electron microscope studies on both the fracture surfaces of tensile test bars and inside the pores of sectioned reduced pressure test samples were carried out with a Phillips XL30 scanning electron microscope (SEM). The X-ray detector is part of an Oxford Link ISIS EDS (Energy Dispersive Spectrometer) system consisting principally of the liquid-nitrogen-cooled detector crystal mounted in the SEM column which was used for the quantitative X-ray analysis of the local composition of the alloy.

### 3.9 Quality Index Studies

A series of studies were carried out in an exploratory study to find a parameter that would, for the first time, characterise the quality of a melt in a quantitative manner. Initially the shape

factor (Equation 3.4) obtained from image analysis results was used in an effort to make the test quantitative ( $QI_1$ ).

In second study a second parameter ( $QI_2$ ) was chosen where the average length of pores and the number of pores were taken in account:

$$QI_2 = \frac{\text{average shape factor}}{(\text{average pore length}).(\text{number of pores})} \quad (3.7)$$

In a third study, the number of bifilms was thought to characterise the quality. So, another quality index ( $QI_3$ ) was proposed involving simply the number of pores:

$$QI_3 = \log(\text{number of pores}) \quad (3.8)$$

Finally, a bifilm index ( $QI_4 = BI$ ) was proposed:

$$QI_4 = \text{Bifilm Index} = \sum (\text{pore length}) \quad (3.9)$$

This was an index that was easily calculated, and that gave a numerical result in millimetres. It was expected that the resulting number might be a good measure of metal quality that would be sufficiently easy to use to be adopted for use on the foundry floor.

## CHAPTER 4

### RESULTS

#### 4.1 Laboratory Tests

##### *4.1.1 Effect of binder type and content on RPT*

The experiments with the reduced pressure test originally began with a study of the effect of the binder content on the RPT density and hydrogen content to ensure that no unwanted interference was occurring. The early concern in the use of a chemically bonded sand mould was that as the binder content increased the permeability of the mould would decrease and in turn bubbles would be trapped in the sample and thereby reduce the density of the RPT samples. Also, once the hot metal is poured into the mould, the products of the decomposition of binders might have led to an increased gas with the mould/metal reaction.

An investigation was carried out with LM4 alloy. As seen from Figure 4.1, different binder contents (1.2, 2.4, 4.8 wt% resin and 4 wt% silicate) had no clear effect on the density of the reduced pressure test samples at 100 mbar. The density index (Equation 3.2) change with different resin contents also showed a similar result (Figure 4.2). The interesting finding was the increased scatter in the density results as the residual pressure was lowered from 1000 mbar to 10 mbar (Figure 4.3-4.4). This can also be seen from the comparison in Figure 4.5. The range of density index under normal atmospheric pressure (1000 mbar) is only approximately 0.5 to 1.5% whereas at 100 mbar it is approximately 1.5% to 7% and at 10 mbar approximately 1.5% to 20%.

As seen from the sectioned surface of the RPT samples in Figure 4.6, the pore morphologies and sizes for the same pressures were substantially similar despite differences in binder content. It was concluded that there was a negligible effect of the sand binder on the RPT results. Therefore, because of its simplicity in making and quicker time of curing, 4% sodium

silicate binder (with 2% coal dust addition) was used in experiments that were carried out in the laboratory for all the remaining tests.

#### ***4.1.2 RPT optimisation of temperatures and pressures***

As shown in Appendix I, there is an almost linear relationship between the density of the reduced pressure test sample and the gas content of the melt. This relation assumes that no hydrogen is retained in solid solution, and that all the hydrogen that was originally present in the liquid forms pores. If the gas in the pores is at a pressure equal to the chamber pressure, then close-linear relationships between hydrogen and density at different chamber pressures can be obtained. These theoretical predictions are shown in Figure 4.7.

A series of RPT tests was then carried with LM4 at different temperatures (700°C, 800°C, 900°C) and vacuum levels (10, 50, 100, 200, 1000 mbar). The comparisons of the theoretical relationship and the density of the samples are shown in Figure 4.8 (a-e). The first observation in these results was that the density of the samples did not closely follow the theoretical lines. Again, there was a wide scatter that increased with the increased vacuum.

The sectioned surfaces of one example of each of the series of RPT experiments are shown in Figure 4.9. It is interesting to note that there is no particular pore size or shape that depends upon any of the variables such as hydrogen level, temperature nor pressure.

At 10 mbar, it was observed that some pores burst from the top of the samples. A schematic drawing of this action is shown in Figure 4.10. The sectioned surfaces of some samples are shown in Figure 4.11. Following the action of bursting, the interior of the pore came in contact with the air, so further oxidation took place. This appears to be the reason that some of the pores on the top of the samples looked shiny.

Figure 4.12 a to l shows SEM images from inside the pores of RPT samples. Numerous types of pores were investigated: crack-like, round, interdendritic. The important observation in these pictures is the existence of oxide films in every pore. These rough and thick oxides were confirmed by EDS analysis given in Figure 4.13.

### ***4.1.3 The assessment of effect of bifilms on RPT***

A 200 kg charge of LM0 was melted in a resistance furnace at 750°C. After a careful cleaning treatment (fluxing and degassing for three times with a rotary degasser), the reduced pressure test samples were taken from the melt. These data are shown as filled points in Figure 4.14. Then, after deliberately introducing bifilms (which possibly increased hydrogen content of the melt with air entrapment and breaking of the surface film), samples were taken again which are shown as open points in Figure 4.14. It is interesting to note that the density of the samples fell when action to introduce bifilms was introduced.

In Figure 4.15, same results can be seen from the sectioned surfaces of the reduced pressure test samples. There was no pore formation in the clean melt - in the absence of bifilms - (top row). The pores formed only when the bifilms were deliberately introduced (bottom row).

SEM pictures from inside the pores of pure aluminium samples are shown in Figure 4.16. There are thin and newly formed oxides, together with original bifilms of thick oxides that were folded into the melt. The films were confirmed as oxides by EDS analysis.

## **4.2 Industrial Trials**

This section of the study involves the experiments carried out at the secondary smelting company.

### ***4.2.1 Fluxing and Degassing Studies***

A study was carried out at the melting stage in one of the electric furnaces. Two different gas flow rates were investigated during fluxing and degassing of alloy LM27. In the lance degassing stage, a high gas flow rate was first used to replicate normal production conditions. A second experiment was carried out at a lower gas flow rate, so that the surface of the melt was hardly disturbed. The RPT result of the comparison between high and low flow rates is shown in Figure 4.17. As seen from the figure, after melting prior to any treatment, the

density of the RPT samples and hydrogen is scattered. With the high flow rate, the density is increased but hydrogen remains high. On the contrary, with low flow rate, when surface of the liquid metal was not disturbed, the hydrogen levels were lowered but the density values were scattered.

In a second study with LM4, two different types of ceramic diffuser were used. The aim of this experiment was to see the effect of distribution of bubbles generated by ceramic diffusers and their effects on the metal cleanliness. Although the bubble distribution was seen to be very different (Figure 4.19 and 2.26), as seen from Figure 4.18, there was no clear dissimilarity between the effectiveness of T-type and disc-type diffusers. However the average density values for RPT results from the use of the lance, T-type and Disc-type diffusers were in an ascending order; 2275 kg/m<sup>3</sup>, 2323 kg/m<sup>3</sup> and 2462 kg/m<sup>3</sup> respectively.

#### ***4.2.2. Studies at the Casting Area: Two different Casting heights***

As was described in Section 3.2.2, in the casting area during mould filling, two different casting heights were examined. The density-hydrogen relationship (LM24) when ingots were filled from different heights is shown in Figure 4.20. Two melts with same chemical composition were used for each casting trials (top poured and bottom filled). As seen from the graphs, although the average hydrogen content of the top pouring system had lower hydrogen content compare to bottom filled castings, they gave lower density results. It is important to note that this showed that it was bifilms (turbulent filling) that decreased quality not the gas content. This can be seen in density histogram diagrams in Figure 4.21 a-b.

Actually the difference was observed more clearly on the sectioned surface of the reduced pressure test samples (Figure 4.22). In the bottom filled system, the pores appeared round and small. With the turbulent filling in the top poured system, the pores were larger and their shapes were more complex. The SEM results (Figure 4.23) showed that the pores in bottom filled system also contained some oxides whereas the oxides in the top poured system were crumpled and bigger.

Similar results were found when the test was carried out with LM25. As seen from Figure 4.24, the reduced pressure test samples of the bottom filled system are clearly separated from top poured samples with higher density values. The density histogram diagram illustrates this more clearly in Figure 4.25. The pore morphology change of the RPT samples can also be seen in Figure 4.26.

#### ***4.2.3. Studies in Holding Furnace: Trials on use of Diffusers***

In the secondary remelting process, following the fluxing and degassing, the melt was transferred into the holding furnace. The RPT samples gathered from the holding furnace are given in Figure 4.17 and are seen to be clustered in Region IV. The sample collection was carried out after 30 min to 1 hour holding time. An increase in the density of RPT samples was observed during this time period. However, there were still some concerns about the introduction of bifilms during transfer of the melt from melting furnace to the holding furnace, mainly due to the heavy turbulence and high fall of the liquid on the transfer between these vessels. Therefore an investigation was carried out in the holding furnace by installing two diffusers at the bottom of the furnace. The dimensions of the holding furnace and the position of the diffusers were given in Figure 3.4.

The studied alloy was LM24. Three ingots were taken: one from the start, one from middle and one from the end of the casting process. Different numbers of diffusers were run: 0, 1 and 2. These collected ingots were then melted and heated to 750°C in an induction furnace in the University Laboratory. The RPT samples were taken and the results given in Figure 4.27-4.28.

When no diffuser was used, the densities of the reduced pressure test samples fell towards the end the casting process (Figure 4.27a). Once the diffusers were active, the density stayed high between 2700-2550 kg/m<sup>3</sup> and the results were less scattered (Figure 4.27b, c). This more uniform high quality with the use of diffusers is illustrated clearly in Figure 4.28.

In the second study of the action of the diffusers, three additional major aspects in the casting technique were changed and investigated. These were summarised in the schematic drawings shown in Figure 3.5.

The first change was the height of the launder that delivered the melt to the casting area. The launder was lowered to its maximum extent, so that the fall of the liquid metal would be minimised (Figure 3.5a '1'). The second was carried out at the casting device that filled the mould from the bottom. The internal geometry of the device was clearly not altogether satisfactory, involving some degree of turbulent fall. Therefore the design was altered slightly and casting was slowed down to the degree that eliminated the worst aspects of the turbulent flow in the device such that the melt was filled from the bottom of the ingot slowly with much reduced disturbance (Figure 3.5a '2'). The third change was made in the tapping procedure of the holding furnace (Figure 3.5b '3'). When not controlled carefully, the liquid metal jets out from the tap-hole with the result that the melt is violently and turbulently propelled along the launder, clearly creating new bifilms and dross.

The results were notably different to those of the original production conditions. There was a clear increase in the quality of the castings when these changes were made. The density increases in the reduced pressure test samples when no diffuser is used are given in Figure 4.29a. In these figures, the term "SET 1" indicates the set of results from the previous design (non-quiescent conditions), and the term "SET 2" indicates the new results after the changes have been made as described in the previous paragraph (relatively quiescent conditions). When no diffusers were used (Figure 4.29a), the increase in the density was approximately  $+100 \text{ kg/m}^3$  for each section of the casting; from  $2620 \text{ kg/m}^3$  to  $2704 \text{ kg/m}^3$  at the start,  $2538 \text{ kg/m}^3$  to  $2673 \text{ kg/m}^3$  at the mid,  $2454 \text{ kg/m}^3$  to  $2617 \text{ kg/m}^3$  at the end. The average increase in the density when diffusers were on (Figure 4.29 b, c) was about half of this value, approximately  $+50 \text{ kg/m}^3$ . It is important to note the overlapping scattered data for Set 1 and Set 2 when diffusers were active (Figure 4.29 b, c).

### 4.3 Quality Index Results and Evaluation of Bifilm Index

The ultimate goal of the quantification of the RPT is to define an index or a number so that an action could be taken in order to produce a high quality casting. From this perspective, several studies were made and several quality indices were investigated.

In the RPT, by the solidification under vacuum, the pore formation is magnified, allowing bifilms to become detectable by X-ray radiography and so suggesting a potential direct technique for the study of pore size, shape and distribution. Radiographic images of some RPT samples are given in Figure 4.30. As seen from the figures, the pores overlap and the resolution is not so clear. Despite the obvious interest of these images, it was hard to deliver any quantitative interpretation from these images. This approach was therefore abandoned.

Therefore it was decided to section the samples vertically (Figure 4.31), split into two halves and then carry out studies by simple optical metallographic techniques. Quantitative image analysis was carried out on these polished surfaces. Before relying on the image analysis results, a series of studies was conducted with three different software and image analysis of various shapes were investigated which is shown in Appendix II.

The image analysis results (shape factor, pore percent, pore area) taken from the studies with LM4 are shown in Figures 4.32-4.42. As seen from these Figures, there is no effect of hydrogen content on the shape factor. The values for each pressure (200, 100, 50 and 10 mbar) lie between 0.4 and 0.6. Looking at the effect of temperature (Figure 4.36), it appeared that there is a slight decrease in the shape factor with increased temperature. It is interesting to note that the average pore area and pore volume percent increased with increased temperature (Figure 4.37-4.38). It is important to note that the pore area was calculated from the sectioned surface of the RPT samples. Nevertheless, the pore percent almost linearly decreased with the density of the RPT samples as seen in Figure 4.39 (disregarding the scatter possibly due to the two dimensional calculation of porosity which is a three dimensional volumetric element) but notice the scale of scatter when comparing the pore percent with hydrogen content in Figure 4.40. Similar scatter was observed for relationships between average pore area and hydrogen (Figure 4.41) and average pore area with density (Figure 4.42).

After collation of the image analysis results, different quality indices were proposed (as was given in Section 3.9) and were tested to establish correlations between the observed differences in pore morphologies and estimated behaviour of bifilms. The results of these studies are given in the following section.

### ***4.3.1 Methods investigated to quantify RPT***

The first notable observation was the shape of the pores (Figure 4.9, 4.22, 4.26). Some were elongated and some were round. Therefore the first proposed quality index was the shape factor ( $QI_1$  -Equation 3.4). The change in the shape factor with the density of the RPT samples (alloy LM4) is given in Figure 4.43a. The results appeared to be uniform between 0.3 and 0.6, therefore the distribution of shape factors was plotted (Figure 4.43b) and seen to be more frequent around 0.5.

The second quality index ( $QI_2$  -Equation 3.7) included the average size and the number of the pores. The change of density with the second quality index appeared to give a better understanding of the variables (Figure 4.44). The relationship seemed to be logical in a sense that the quality was increasing with increased density. When comparing two different casting heights (Figure 4.45), the turbulent filling (top poured) had a lower quality index compared to the quiescent filling (bottom filled). The average values were 0.23 and 1.43 respectively.

In the studies with the  $QI_2$  (Figure 4.45), a sudden increase was observed after density values over  $2500 \text{ kg/m}^3$ . It was found that this increase was mainly due to the number of pores. Therefore in the third quality index studies only the number of pores on the sectioned surface of RPT samples was considered. The theoretical approach on the change of density with the  $QI_3$  (Equation 3.8) is demonstrated in Figure 4.46 and the results are given in 4.47.

Finally, the total length of pores was proposed as a quantifying concept. This length was assumed to be the total length of bifilms measured on the sectioned surface of reduced pressure test samples and was measured by summing the maximum lengths of all the pores. This quantity was called the 'bifilm index'. The results obtained from the experiments are summarised in the following two sections.

#### *4.3.1.1 Laboratory test results*

The first bifilm index results were obtained from the initial tests where the effects of temperature and pressure on RPT samples were investigated with LM4. The relationship between density and bifilm index is given in Figure 4.48-4.49. As can be seen from the figures, as the density is increased bifilm index was decreased, however the scatter of the results was for all temperatures and pressures within approximately a factor of 2.

From the same experiments, the relationship between bifilm index and hydrogen content of the melt was also plotted. These results are shown in Figures 4.50-4.51. It is important to note that there is no similarly clear relationship between hydrogen content and the bifilm index.

#### *4.3.1.2 Industrial test results*

The bifilm index comparison of two different casting heights for LM24 is given in Figure 4.52. As seen from these results, the average bifilm index of the bottom filled samples was below 100 mm: 44 mm for 100 mbar and 96 mm for 50 mbar (Figure 4.52 a-b). For top poured samples, the values are scattered between 50 mm and 250 mm with an average of 138 mm for 100 mbar and 196 mm for 50 mbar. It is clear that there is about a two-fold difference in the quality of turbulent and non-turbulent filling systems.

The comparison of the Weibull distributions of the bifilm index of top poured and bottom filled samples can be seen in Figure 4.53. Interestingly, the top poured castings exhibited a higher bifilm index, but also a higher Weibull modulus (Table 4.1) as a result of the castings being consistently bad. In contrast, bottom filled samples show lower bifilm index, but, paradoxically, with lower Weibull modulus as a result of the somewhat higher scatter.

Similar results were found when two different casting heights are compared with LM25. The bifilm index of these tests is given in Figure 4.54. As seen from the figure, for the top poured samples, the density values are below  $2400 \text{ kg/m}^3$ . The bifilm index is scattered between 10 to 370 mm with an average of 148 mm. The density of RPT samples collected from bottom

filled castings are at relatively high levels between 2400 and 2600 kg/m<sup>3</sup> and the bifilm index is between 1 and 100 mm with an average of 48 mm.

The comparison of the Weibull distributions of the bifilm index values of top poured and bottom filled castings in alloy LM25 (Figure 4.55) displayed a reasonably similar character to LM24 studies (Figure 4.53). In this case, in line with expectations, top poured system had higher bifilm indices compared to bottom filled castings, but had similar Weibull modulus (Table 4.1). It is worth commenting that the Weibull slopes may not be reliable for relatively small populations of results such as those investigated here [231-232].

Bifilm indices were also calculated for studies where different number of diffusers were investigated in the holding furnace. The results are given in Figures 4.56-4.58. As was described previously, sample ingots were taken from the start, middle and end of castings when 0, 1 and 2 diffusers were run. Also, different casting conditions were tested ('SET 1' for non-quiescent and 'SET 2' for quiescent).

When no diffuser was used, the data is spread all over the graphs, showing little correlation, with only a weak trend of increasing bifilm index with decreasing density. Further, the materials cast at the end of the casting run showed lower density and higher bifilm index. However, when diffusers are active, the data are compacted into lower right region of the graph which is the high quality region where the density of RPT samples is high and the bifilm index (total length of oxides) is low (Figure 4.56 a-c).

Another representation of the results is summarised in Figure 4.57. At the start of the casting, the bifilm index lies between 100-150 mm. When no diffusers were operated the bifilm index rose toward 250 mm as the end of casting was approached. When diffusers were operational the bifilm index fell to around 100 mm during the course of a production run. It is important and interesting to note that there is no clear difference between the results when using one diffuser or two.

The comparison of the bifilm index results where two different conditions are compared are given in Figure 4.58. The average bifilm length values for 'SET 1' conditions (which is the

fast and turbulent casting: non-quiescent) were 188 mm without diffusers and 100 mm with diffusers. In ‘SET 2’ conditions (the quiescent conditions) these rather high results fell to 39 mm without, and 35 mm with diffusers (Figure 4.58).

It is interesting to note that when the casting is carried out quiescently (achieved simply by implementing simultaneously all the three changes investigated in this study), the average bifilm index values of quiescent conditions (SET 2) was below 50 mm even when no diffusers were used in the holding furnace (Figure 4.58).

Weibull distributions of the bifilm index of two different conditions (non-quiescent and quiescent) are given in Figure 4.59. Here, the reciprocal of the bifilm index was used, because it is common to be seen in Weibull plots that the properties are increased towards the right hand of the X-axis, hence the increase in bifilm index is a decrease in quality. As seen from the Figure 4.59a, the non-quiescent casting condition displayed higher Weibull modulus with higher bifilm index (Table 4.1). Similar to the findings in LM24 (Figure 4.53), the castings in quiescent condition (Figure 4.59b) had lower bifilm index (indicating higher quality) but scattered with a low Weibull modulus.

### ***4.3.2. Relationship between Bifilm Index and Number of Pores***

As was seen in the studies with different quality indices, the number of pores was a dominant factor in some cases. It is also important not to overlook this parameter because the new approach proposed in this study takes as a fundamental assumption that bifilms are the initiators of pores. If this is true, therefore, the number of the pores has to directly correspond with the number of bifilms. For this purpose, a graph was plotted between bifilm index and number of pores which is given in Figure 4.60. It appeared from the graph that there was a linear relationship between the variables.

A schematic illustration of four corners of this relationship is given in Figure 4.61. For simplicity the coordinates of this points will be taken as summarised in Table 4.2. The relationship between hydrogen content and the bifilm index is given in Figure 4.62.

## 4.4 Calculation of air gap between bifilm

A graph between density of RPT samples and hydrogen content was plotted in Figure 4.8 showing the calculated relation between these parameters. The data points below the theoretical line indicated an additional source of gas in the samples which is expected from air that entrained by the bifilms.

Therefore an effort was made to calculate the quantity of air (Appendix III). A volume value was found from the density difference between the RPT sample and the theoretical density (for example: indicated by the arrow in Figure 1, Appendix III). This volume was the volume of *porosity* which formed at various temperatures and under various vacuum levels in the RPT (Figure 4.8). This volume was converted to the STP value. Then, the volume of hydrogen at STP (measured by Hyscan equipment) was extracted from this value giving the volume of air per RPT sample at STP. Average bifilm index values and total number of pores are known for each sample from image analysis results of the sectioned surfaces of RPT samples. From this data, the average volume of air can be calculated per pore. Given the average bifilm length for pore, an average air gap can be calculated per bifilm (Appendix III) which is given in Figure 4.63 for each temperatures tested in the experiments. As seen from Figure 4.63, despite rather large scatter and combinations of factor that may influence air gap, as the temperature increased, the average values of air gap between bifilms was decreased: 0.49 mm, 0.44 mm and 0.34 mm for 700°C, 800°C and 900°C respectively.

## 4.5 Tensile Tests

### 4.5.1 *Optimisation of tensile test pattern*

The aim of the mechanical tests was to compare the tensile test results with the bifilm index of castings. Therefore different test bar patterns were investigated by real-time video X-Ray radiography with a view to optimising the design to achieve quiescent filling (Figures 3.11-

3.12). The Weibull distributions of the mechanical test results that compare the different test bar patterns using LM27 ingots are shown in Figure 4.64.

It was extremely inconvenient and costly to machine bars directly from the ingots. If the material could be remelted and cast into test bar cylinders that would be easily machined, the work could be expedited efficiently. Therefore, to confirm the validity of the final optimised test bar mould design, a check was carried out using alloy LM4 to assess whether oxides were gained or lost by remelting. An ingot was machined into test bars and another one was carefully remelted and cast into moulds. The comparison of the Weibull distributions of the properties of these tests is shown in Figure 4.65.

#### ***4.5.2 Comparison of different conditions***

Following the mould optimisation studies, a comparison of mechanical properties between different casting heights and different Mg contents with the changing bifilm index was investigated.

In the first test, LM2 was used. In these tests, the term “low Mg” indicates 0.02 wt%Mg and the term “high Mg” indicates 0.30 wt%Mg. Sectioned surfaces of RPT samples of different Mg content are shown in Figure 4.66. The Weibull analyses of the tensile test results are shown in Figure 4.67 to Figure 4.72.

SEM studies on the fracture surface of the tensile test samples are given in Figure 4.73 a-h (for low Mg LM2) and Figure 4.74 a-h (for high Mg LM2). Oxides can be seen in all the fracture surfaces. In some cases there were iron phases in plate-like form (possibly beta phase) in Figure 4.73 a, e and f and in Figure 4.74 a, c, d and e, all of which seemed to be associated with bifilms.

In the studies with LM24, the casting sequence was examined by selecting sample ingots from the start, middle and end of pour from the 2.5 ton holding furnace. The results are given in Figure 4.75-4.76. The chemistry of the alloy was sampled over this period and found to be accurately unchanged. The analysis results are given in Table 4.3. However, initial strength

values were found to be low, but towards the end of the casting the proof strength increased by approximately 30 MPa. When the glass cloth filter was not used, the increase in strength was accompanied by a clear decrease in ductility (Table 4.4).

The comparison of the parameters obtained from tensile test results (Bifilm index, UTS, proof stress, elongation and Weibull Modulus) are summarised in Table 4.4.

An RPT sample was taken from castings of the tensile test bars to assess the metal quality by bifilm index. The bifilm index changes with the UTS and elongation obtained from Table 4.4 are shown in Figure 4.77. From the same table, the change in Weibull modulus of UTS and elongation with bifilm index was shown in Figure 4.78.

## CHAPTER 5

### DISCUSSION

#### 5.1 The RPT Mould Effect Study

In the new test studied in this work, small chemically bonded sand moulds were used to produce parallel sided plate castings for radiographic examination. The purpose of using a porous sand mould instead of a steel mould is to ensure air cannot be trapped at the mould wall. It is believed that air entrapment and the subsequent passage of bubbles into the sample are partly responsible for the poor reliability of previously studied reduced pressure test techniques [136, 233-237].

For this purpose a preliminary test was carried to examine the effect of binder content. Although it was thought that as the binder content increased, the permeability of the mould would decrease so that the hydrogen release would decrease and bubbles would be entrapped, interestingly, no detectable effect of the binder content was found at 100 mbar (Figures 4.1-4.2). As seen from the graphs (Figure 4.1-4.2), there was no significant change in the density nor pore size of samples cast in moulds having different binder contents. It is also interesting to note that there was relatively a uniform distribution of the pore sizes throughout the sectioned surface of the RPT samples; there was no obvious metal/mould reaction concentrated beneath the surface of the casting. Thus it seems safe to conclude that any reaction between the test mould and the metal must be negligible.

#### 5.2 Pore Formation and Growth

To investigate the optimum test conditions and also to examine the variables in the reduced pressure test, different vacuum levels and different temperatures were inspected (Table 3.2). There were several important findings from these experiments. One of them was that at 10 mbar bursting of pores from the surface was observed (Figure 4.11). This was also clearly observed from the  $d_{\text{index}}$ -pressure graphics (Figure 4.5). It is obvious that as the vacuum

increases, pore formation is enhanced dramatically (at about 1/100<sup>th</sup> of an atmosphere the volume increases by a factor of approximately 100). This indicated that the use of high vacuum levels would possibly lead to an underestimate of the gas or oxide content of the sample.

It can be noted that bifilms are not visible in those samples solidified at 1 atmosphere pressure (at which Density Index=0.00 % of course), but films adopt their crack-like morphology for Density Index between 0.86 and 2.58 % (Figure 4.9). Above this range, the density index indicates that bifilms are opened to become nearly spherical pores.

At 1000 mbar (1 atmosphere pressure), the RPT results shows no change in density (Figure 4.8a). There are only minor changes which are believed to be related to the amount of shrinkage which is also influenced by bifilms. It is interesting to note that, except for one sample, all the data were above the theoretical line shown in Figure 4.8a. This suggested that hydrogen was not a dominant factor in pore formation. This also confirms the hypothesis of the structure and action of bifilms; although the pore is expected to grow larger with the help of hydrogen diffusing into the central gap, the bifilm is to some extent resistant to unfurling. This resistance is progressively overcome as the RPT pressure is reduced, expanding the residue of the entrained air, and what hydrogen may be present, between the films.

For samples solidified at 200 mbar (Figure 4.8b, 4.41-4.42) the average area of each pore is below 0.1 mm<sup>2</sup> and the density index is around 5%. It seems that the vacuum level – the driving force - is sufficient to magnify the pore (i.e. inflate bifilms) to a limited extent. However, the level of vacuum required for a practical and reliable quantification of RPT would require an even lower pressure between 200 mbar and 10 mbar. As we shall see, a value of 100 mbar corresponds to current industrial practice, and is confirmed in this work as being an appropriate and practical level.

The more interesting result obtained from these preliminary tests is that the predicted linear relationships between hydrogen level of the melt (Figure 4.7) and the density of the reduced pressure test samples were not closely followed in any of the tests carried out at lower pressures as shown in Figure 4.8. As the vacuum level was increased, the observed behaviour

shifted more radically away from the predictions of the simple theory, indicating that typical porosity in castings does not follow closely the laws of free precipitation and expansion by classical gas laws. Clearly, the behaviour is complicated by the expansion of entrained air under vacuum (not previously suspected as a cause of porosity in Al alloy castings) and by the random mechanical problems of opening irregularly convoluted bifilms, potentially inhibiting pore growth.

The Weibull distributions of bifilm index results (Figure 4.53, 4.55, 4.59) were in good agreement with this general picture. The non-quiescent casting conditions were consistently bad with Weibull moduli closely grouped at 3.1, 2.5 and 2.6 (Figure 4.59) and the average bifilm indices were high at 188 mm, 110 mm and 102 mm for 0, 1 and 2 diffusers respectively. Furthermore, when quiescent conditions were achieved, the bifilm index dropped down to 50, 35 and 34 mm indicating that the quality was increased. However, the Weibull modulus values appeared to fall somewhat to 0.5, 1.1 and 1.7. However, this fall in slope is merely a result of some data improving in quality (some higher data points are grouped further to the right on the graph), thus the result is logical, if rather counter-intuitive at first sight. Similar results can be seen in studies with different casting heights. In Figure 4.53, in the comparison of the Weibull distribution of bifilm index of top poured and bottom filled castings, the top poured system has high bifilm index values and high modulus compared to bottom filled castings. This implies that the top filled castings are bad, and uniformly so.

In earlier investigations with RPT, several workers [136, 233-236, 238-240] have attempted to quantify the reduced pressure test with the principle that involved measuring the density of the sample. From that, the volume of the pore in the sample was calculated. Since hydrogen is the only soluble gas, it was assumed that these pores were filled with hydrogen gas. Therefore the volume of hydrogen would be equal to the pore volume of that sample.

A theoretical relation between hydrogen and density was taken in account (Figure 4.7 and Appendix I) and it was assumed that as long as the density was high the quality was said to be high too (Figure 5.1). The density was only related to the hydrogen content of the melt.

However, the scatter of results observed between the hydrogen level of the melt and the density of the reduced pressure test (Figure 4.8) would be expected from the presence of bifilms. This was one of the first indications that the approach of simply measuring the density would be misleading. Although LaOrchan *et al* [240] observed similar scatter (Figure 5.2), they tried to obtain a linear relationship from the data, simply because in theory they believed there had to be such a relation. However, they disregarded the fact that the density values were not affected purely by hydrogen and the problem of effect of metal cleanliness on the density of the samples was never argued.

As seen from the hundreds of results at different vacuum levels (Figure 4.8), the theoretical line divides the graph into two regions, the upper and the lower parts:

➤ *samples on the theoretical line:*

If no hydrogen is retained in solid solution in the alloy, all the hydrogen that was originally present in the liquid forms pores in the solid and none is pumped out of the system during the test and gas forms at a pressure equal to the chamber pressure, then the data should follow the theoretical lines.

➤ *samples above the theoretical line:*

It is well known [127, 134, 170, 195] that there is a threshold hydrogen level below which no pore formation is observed. There is also a solid solubility limit that depends on both the cooling rate and the alloying elements. It can be concluded that hydrogen makes a comparatively small contribution to the nucleation of the bubble, because it concentrates relatively little ahead of the advancing freezing front due to its high solubility in both the liquid and the solid, combined with its high diffusivity [5]. If in addition the gas has no favourable substrate on which to form, it is forced finally into supersaturation in the solid. This effect can be seen in this work. Most figures (Figure 4.8 and 4.14) show a cut-off in results at approximately 1.0 mL/kg Al. Therefore, the experimental results that are above this theoretical line, representing higher densities, are reasonable and explainable.

➤ samples below the theoretical line:

The lower part of the graph is not easily explained assuming the effect of hydrogen alone. It follows that the data below the line necessarily results from another source of gas. Since the test is simply solidification under vacuum, there can be negligible contribution from any other source of hydrogen, but a contribution of air is to be expected from that entrained in the original formation of the bifilms.

In most of the reported investigations summarised in Table 2.1, the initial cause of porosity formation is assumed to be the limitations to feeding. The precipitation of hydrogen from solution is included in the term as an additional force acting to enhance pore formation. So, as long as the pressure inside the pore was equal or greater to the sum of pressures;

$$P_g > P_H - P_S \quad (5.1)$$

pore growth would be achieved where  $P_g$  is pressure in the pore,  $P_H$  is pressure due to hydrogen and  $P_S$  is pressure due to shrinkage. Looking at these assumptions, it seems most likely that if shrinkage is eliminated, then the only factor remaining is hydrogen which is incapable of forming pores homogeneously. In fact, as will become increasingly clear, the formation of a pore almost certainly does not include a nucleation process; bifilms serve as sites into which hydrogen in solution in the melt diffuses and forms molecular hydrogen, thereby contributing to the porosity. Then the shrinkage – if such is present – pulls it from outside to help the pore to grow. Consequently pore formation is a growth phenomenon because the initial pore pre-exists as the entrained air in the bifilm.

A number of earlier workers have assumed that surface tension would be important in pore formation, and have therefore attempted to investigate this [132, 168]. As seen from Equation 2.7, surface tension is in direct relationship with the pressure of inside the pore, assuming the pore to be a bubble, with, of course, a spherical liquid surface. However it was found that the surface tension had no significant effect on the porosity that was formed. This is perhaps hardly surprising because (i) the variations of surface tension are in fact practically negligible, varying only between 0.825 N/m (for Pure Al), 0.790 N/m (Al-7Si), 0.685 N/m (Al-10Si)

[132]. More fundamentally (ii) if the real growth mechanism is the separation of two halves of a bifilm, it follows that surface tension is not involved at all.

In several studies made on porosity formation in aluminium castings, there was no evidence to show that there was a direct relationship between the amount of oxide present and the amount of porosity formed. The predictions were that either hydrogen absorption was increased such that formation of gas porosity was directly related to the amount of dissolved hydrogen in the melt [84, 130, 131, 189, 195, 199] or the mushy zone was increased [190, 191, 196, 197, 201, 241-246]. So, researchers focused on the feedability in the mushy zone, but this feedability problem did not satisfactorily explain the much higher porosity observed in aluminium alloys compared to the theoretical and mathematical approaches made.

It was later reported [247] that melts increased rates of gas absorption from their surroundings due to the possible formation of a more permeable oxide layer. A similar conclusion was observed by Pekguleryuz *et al* [84]. In their study, Sr was added to the melt for modification and the melt was held at 730°C for three hours to reach equilibrium with the atmosphere. Reduced pressure test samples were taken. As the vacuum was increased the pore size was increased but not the number of pores. They assumed that the Sr had increased the oxidation rate, thus pore formation was observed.

Another important similar study was carried by Valtierra *et al* [138]. They studied the role of strontium oxide on porosity formation. They concluded that porosity was not dependent on Sr content but the amount of strontium oxide present in the melt. They had also concluded that the morphology of the pores was determined by the form of the oxides.

Very few researchers mentioned oxide related connections with porosity [85, 87, 88, 150, 157, 164-166, 191]. None of the studies suggested that porosity was effectively nucleating heterogeneously on oxides.

The scenario is that during solidification, hydrogen will be segregated ahead of the solidification front, and may exceed the solubility limit. Since hydrogen porosity cannot nucleate either homogeneously or heterogeneously, it is suspected that it remains in a

supersaturated state. However, in the presence of a bifilm with its enfolded gap, the hydrogen can diffuse in and start to expand the gap to form a pore (Figure 2.21). Actually the initiating porosity is effectively the bifilm itself. These oxides can be seen everywhere in the pores in SEM pictures in Figure 4.12 and 4.13. They are either in folded form as bifilm (a), or some are fragmentary, possibly originating as a part of a bifilm but was partially sucked into the dendritic mesh (b, c, d, e) as was schematically shown in Figure 2.20. Alternatively, what appeared to be an unravelled (fully opened bifilm) was observed in between dendrites (f, g, h). In Figure 4.12 (i to l), young oxide that is formed by the air introduced by the bifilms is seen to be pushed by dendrites. They appear as stretched thin films. These young oxides were visible (Figure 4.12 i-l) but too thin to be detected by EDS analysis because of their nature, however the rough and thick oxides had given clear oxygen peaks (Figure 4.13).

Bifilms are often seen at grain boundaries since the dendrites cannot grow across the air film. With the precipitation of more gas evolving during solidification, the pore may grow more rounded. Finally, the size may be such that the original bifilm will become relatively insignificant in size, effectively tucked in a corner of the pore, while the pore expands into (i) the free liquid to become a spherical pore or (ii) among the dendrites to become an interdendritic pore (Figure 2.21). Both types could be gas or shrinkage or a mixture of the two, depending on whether the pore grows freely in the liquid, or gases surround by dendrites.

### **5.3 Effect of Time and Temperature on Pore Morphology**

It was found that there was no clear effect of temperature on the reduced pressure test results in studies with LM4 (Figure 4.8). Simply, it would be expected that as the temperature was increased, hydrogen pick up would increase (provided moisture or other source of hydrogen was available in the environment of the melt) which would lead to a higher porosity level. This was not found, corroborating the fact that the drying of the furnace refractories had been effective, so that the hydrogen derived from this source was negligible. Although the highest bifilm index value (400 mm) was found at 900°C (Figure 4.50), the distribution of the bifilm index versus hydrogen at different temperatures appeared to be scattered similarly (Figure 4.50).

There is a particularly intriguing observation: it is not related to density but to the pore morphology observed on sectioned surfaces of the RPT samples. As the melt temperature was increased, the pore morphology was altered from a round to a thin and elongated shape (Figure 5.3). This can also be seen in Figure 4.36 where the average shape factor is decreased as the temperature was increased. A similar result was found by Laslaz and Laty [88]. They associated the round pores with strongly oxidized metal where they also found SEM images similar to those shown in Figure 4.12. However, they assumed that the melt was cleaner, because the density of the RPT samples appeared high. In fact, in this study, the SEM results showed that there were some crack-like pores containing fragments of oxides in between the dendrites (Figure 4.12). This can probably be explained by the opening mechanism of a bifilm, more likely by a ratcheting action (Figure 5.4). This action is described below.

Once a bifilm is introduced into the melt, because of bulk turbulence within the melt, the bifilm will be crumpled into a compact form. This bifilm (which is just a few nanometres thick) may at this stage be relatively harmless because of its small overall size and would not be easily detected. In the reduced pressure test, when the vacuum is applied, the volume of gas trapped inside the bifilm will tend to increase and this would force the bifilms to become unravelled, becoming straighter with time.

The diffusion of hydrogen into the gap between the bifilm is another factor driving the growth of pores. But this action would normally only cause an increase in size towards a spherical geometry, reversible if the hydrogen level were to fall. However, in the ratcheting action (Figure 5.4), instead of growing spherically, the bifilm tends to open and at the same time extending its area a little. Such an extended area is oxidized immediately by the air between the bifilms. The process is, of course, irreversible. Thus, as the bifilm circulates in the liquid, its expansion towards the top of the melt, followed by its contraction towards the bottom of the melt, effectively constitutes a breathing, or panting action (Figure 5.5). Since each expansion will be accompanied by the creation of additional oxide film area of the defect, and which cannot be reversed, the area of the bifilm will steadily ratchet up in size. If there is little gas available, the bifilm will merely grow in area but not in thickness, and thus will increase in flatness and length, giving the crack-like forms seen in Figure 5.3c. This is thought to be the mechanism of the elongated pore formation that is observed in the sectioned surfaces.

The stabilisation of the crack-like form by high temperature, despite the varying hydrogen content, possibly suggests that the bifilm diffusion bonds together to some extent, consuming its entrained oxygen and possibly its nitrogen to form bonds of oxide and nitride between the original oxide films [2, 248]. Thus the bifilm will be difficult to inflate, and may have additional rigidity as a result of its increased thickness and its bonding. This is in good agreement with the findings in Figure 4.63. The air volume was reduced as the temperature increased which showed that oxygen in air was being consumed to thicken the oxide of the bifilm.

It is remarkable to note that the form of these crack-like pores does not appear to be sensitive to either hydrogen or pressure. As seen from Figure 4.9, there are samples at 200 mbar with 2.2 mL/kg Al hydrogen level that have the same appearance as the sample at 10 mbar with 3.9 mL/kg Al hydrogen level. Note that the pressure is 20 times higher but the pore morphology looks the same. This proves that the pore size is not the result of normal bubble-like growth processes familiar to physics (in which the bubble is assumed to be always spherical with a liquid/gas interface of a boundary and full of a fluid that follows the Universal Gas Laws), but in all probability is the consequence of the mechanical ratcheting action involved in an irreversible oxide formation (Figure 5.4). This appears to be another unpredicted, complex aspect of the behaviour of bifilms.

SEM studies made inside pores also corroborate the mechanism of their growth by the unravelling of bifilms. In Figure 4.23 (b), there is a crumpled oxide (usually associated with turbulence) seen inside the pore that has grown larger than its originating bifilm. In contrast, in Figure 4.12 (a, g, h), a crack-like pore appears to show a bifilm that is only partially opened in between the dendrites. Only traces of the originating bifilm were found; the remainder was assumed to have been sucked deep into the dendrite mesh, as illustrated in Figure 2.21.

The study with 99% Al at different vacuum levels showed (Figure 4.14) that there would be no pore formation in a clean melt regardless of the hydrogen content (which on occasions was particularly high). The density of the samples remained constant at  $2700 \text{ kgm}^{-3}$ , even though the samples were solidified under vacuum. Once bifilms were introduced, a clear decrease in the density of the samples was observed. This reduction in the density of samples appeared to

be initiated by the inflation of the bifilms as can be clearly seen on the sectioned surfaces of the samples in Figure 4.15 and from SEM pictures of pores shown in Figure 4.16. These results also indicate that hydrogen porosity is not nucleated in a clean melt of pure aluminium in the absence of entrained oxide films. These results confirm early work by Brondyke and Hess [157] and Tiwari and Speech [140].

In the pure Al results of this work, it appeared to be more difficult to produce pores and the pores only formed after the forced introduction of bifilms. This may suggest that either (i) the relatively pure Al is more free of bifilms, or (ii) its rather pure Al oxide amorphous film may be impermeable (or possibly less permeable) to hydrogen, in contrast to Al alloys, in which the oxide structure changes from amorphous to crystalline, producing a less protective film. The crystalline phase contains defects which is one of the reasons why oxidation continues further. In addition, hydrogen finds its way through these defects more easily making the contribution of hydrogen to pore formation in alloys easier than in pure aluminium.

## **5.4 Effect of Different Pouring Height**

The studies in the secondary remelter company in which castings were made from different pouring heights showed the apparent effect of bifilms. Maybe one of most important characteristics of bifilms was found in this investigation. The density-hydrogen relationship when ingots were filled from different heights was shown in Figure 4.20 and 4.24 for alloys LM24 and LM25 respectively. In both of these experiments, the top pouring system gave lower density results compared to the bottom filled system. The histogram of density results showed this distribution more clearly in Figure 4.21 and 4.25. In both cases, the density distributions of top poured castings are wider and the average values are lower whereas the bottom filled samples have steeper and narrow distribution at high density levels.

In the top poured system for LM24 (Figure 4.20), even though the hydrogen levels appeared low, the density results were low too. However, in the bottom filled samples, the density results were higher. Such results illustrate, if further illustration is needed, the non-wisdom of using the RPT as a hydrogen test. This discrimination was much clearer in studies with

LM25. As seen from Figure 4.24, the density of reduced pressure test samples taken from the top poured system is separated clearly from the bottom filled samples.

Similar results were also found on the studies with diffusers used in holding furnace. There was a significant increase in the density of the reduced pressure test samples between non-quiescent (SET 1) and quiescent castings (SET 2) (Figure 4.29a). The values of increase were  $84.4 \text{ kg/m}^3$ ,  $134.6 \text{ kg/m}^3$ ,  $163.0 \text{ kg/m}^3$  for start, middle and end of casting respectively.

The most interesting observation was seen on the sectioned surface of RPT samples (Figure 4.22, 4.26). In the top poured system, with the turbulent filling, when bifilms were incorporated together with trapped air, the unravelling process of bifilms was easier such that this is clearly seen from the large and irregular pore morphology, in line with expectations.

Another interesting result is that the number of pores was smaller in the bottom filled system (Figure 4.22, 4.26). In the top poured system, when bifilms were generated due to the turbulence, more initiation points for pore growth were created. These results can be seen in Figure 4.22, 4.26 from the sectioned surface of both alloys LM24 and LM25.

It is also interesting to note that in studies with LM25, the bottom filled sample castings had a flat upper surface (Figure 4.26) while top poured samples have convex upper surface due to increased pore size as a result of bifilms.

## **5.5 Effect of Different Gas Flow Rates used during Fluxing and Degassing**

At the melting stage, during the studies with LM27 in the 2.5t induction furnace, it was observed that fluxing and degassing had created violent turbulence on the liquid surface. Because of the concerns regarding the introduction of bifilms, an investigation was undertaken with different gas flow rates during this cleaning process. The reduced pressure tests result of this study was given in Figure 4.17.

The data in this figure naturally divide into four regions. Region I shows the results of samples that were taken from the induction melting furnace before any treatment. As can be clearly seen, this region is the most scattered in terms of both density (1700-2700 kg/m<sup>3</sup>) and hydrogen content (2-12 mL/kg Al).

Region II represents the high flow rate degassing. This region is somewhat denser (2300-2700 kg/m<sup>3</sup>), but wider in terms of hydrogen content (2-10 mL/kg Al). This may be because there is a net reduction of the effects of bifilms since bifilms are attached to the rising bubbles, but gas in solution appears to have been increased as a result of enhanced absorption by the disturbance of the surface.

Region III, the low flow rate studies, shows a significantly improved efficiency of degassing. Hydrogen level is the lowest and the narrowest in the graph between 2 and 4 mL/kg Al. However, there exists a scatter in density results (2100-2500 kg/m<sup>3</sup>) which appear to be an indication of insufficient cleaning out of bifilms. It is also important to note that in this region, even though the hydrogen level is low, the density is decreased noticeably, possibly because of the effect of bifilms giving an increased contribution of air (or remnant of air such as N<sub>2</sub> or Ar) resulting in higher porosity.

Finally, Region IV shows the holding furnace results. In this case, both hydrogen and density results appear improved. This seems likely to be because of the sink and float mechanism in the holding furnace where inclusions, as well as bifilms, find time to settle (heavier ones sink, lighter ones that contain more air gap float to surface) and hydrogen in the melt has time to come into equilibrium with its environment which, despite the fuel firing of the holder, seems satisfactorily low. As was also reported by Martin *et al* [249], settling was found to be beneficial to metal cleanliness in controlling the concentration of inclusions.

## 5.6. Comparison of effect of ceramic diffusers during fluxing

In principle, it was assumed that with the use of ceramic diffusers during the fluxing and degassing process in the 2.5t induction furnace finer and homogenous distribution of bubbles would be created so that the cleaning process would be more effective. Schematic drawings

were given in Figures 2.25-2.26 and 4.19. However, this was not found. As seen from Figure 4.18, the results of fluxing and degassing with lance, T-type ceramic diffuser and Disc-type ceramic diffuser are scattered, their RPT distributions overlying in the density/hydrogen field.

Moreover, during the treatment practice with the ceramic diffusers, their heavy weight caused the steel tube to bend. Also, because of thermal shock and repeated use, the ceramics started to crack. In addition, of course, they were expensive. Thus further trials with ceramic diffusers was discontinued. No additional benefit was also seen from the disc diffusers.

Therefore, later at the primary melting stage in the induction furnaces, only the lance system was used. Even though the high flow rate introduced bifilms (as was shown in Section 4.2.1), by the use of diffusers set into the floor of the holding furnace any remaining or newly created inclusions or bifilms were controlled. This action, together with the quiescent conditions later achieved (Section 4.2.3), the quality of the castings were improved significantly.

## **5.7 Evaluation of bifilm index**

Quantification of the quality of the melt is a challenge. Gathering all the results obtained so far from all different conditions and alloys, and considering the complex behaviour of bifilms a quantification study was made and several quality indices were proposed and evaluated. A total of four different concepts of quantification have been explored, with progressively more meaningful and/or useful results.

First, in terms of quantification, a simple practical approach was made following the many previous workers [136, 234-240] who have attempted to quantify the reduced pressure test. A linear relationship between density and hydrogen was assumed, as was shown in Figure 4.8. It was suggested that as long as the density was high, the metal quality was said to be 'clean'. However, as we have discussed, there are fundamental reasons why a direct approach is not likely to be successful; the melt can be dense even though full of bifilms if the bifilms are not opened. Only if there is hydrogen to diffuse into any available existing bifilm, the bifilm will begin to unravel, expand and grow into a pore, and so cause a measurable reduction in density.

Image analysis of the sectioned samples was studied in a further effort to make the test quantitative. The shape of the pores was important. A round and a small pore would be considered to be less harmful than a large and elongated pore which is assumed to be an indication of bifilms [5]. Therefore, shape factor ( $QI_1$ ) was measured. However, the results revealed a relatively constant shape factor in the region of 0.5 (Figure 4.43a). Unfortunately, the pore morphology clearly seen by the unaided eye (Figure 4.9, 4.22) was not easily detected by the image analysis software. This is hardly indicative of porosity resulting from spherical hydrogen bubbles expanding freely in a liquid metal, in which case they would have a constant shape factor of 1.0. Alternatively if the opening of bifilms were easy and progressive, the shape factor would be seen to increase steadily from 0 to 1.0 so that the shape factor would be expected to span this complete range. However, the observation of a fairly constant factor in the region of 0.5 is, however, probably the behaviour to be expected from a messy tangle of crack-like oxide pockets that exhibit some difficulty to expand and straighten to form spherical pores.

It was hoped that the total volume of gas observed in pores would bear some close relation to the total hydrogen content. However, the realisation that probably random quantities of air (probably in the form only of residual nitrogen and argon as a result of the continued reaction of oxygen to form additional oxide) are also involved (Figure 4.8).

The shape of the pores was considered to be of possible importance since it reflected the state of the bifilms whether they were partially or fully opened. In view of the lack of sensitivity of the shape factor approach, a fresh effort was made to find a parameter to quantify the results of the RPT. A second quality index number ( $QI_2$ ) was proposed (Equation 3.7).

The parameter  $QI_2$  was chosen to emphasise the potential quality problems. In this case, the effect of the shape of the pore, the length of the pore and the number of pores were included since all were assumed to act co-operatively to reduce mechanical properties. Thus a high  $QI_2$  number would mean high properties. Note that the basis underlying this formula was that the number of pores was related to the number of bifilms, and the shape and the length of pores are related to the degree of their expansion (Figure 4.44-4.45).

The observed relationship seemed reasonable (Figure 4.44-4.45). The results presented in Figure 4.45 clearly mirror those of Figure 4.43b. They show that the quality of most of the melts that were tested was poor (the values are below 1). It is clear that as the pressure was increased, the quality index number increased, because the volume of the pores will decrease. This reflects the well-known fact that the pressurisation produced, for instance, by a feeder acts to reduce porosity, and additional artificially applied pressure reduces porosity further [5].

In contrast, there were two outstanding data points that have been circled (Figure 4.44): having values of 4.8 (a) and 1.2 (b) quality index. Interestingly, the sample with higher density (b) had lower quality index number. The reason was because this sample had a shape factor of 0.25 and a pore length of 2.1 mm. Sample (a) has 0.54 shape factor and 0.61 mm pore length, which simply means that the lower quality index sample has longer and more crack-like pores. Although these quality index results suggest effects approximately in line with expectations, it is clear that more work needs to be done in this area.

The further interesting feature of Figure 4.45 was the sudden increase in quality index above  $2600 \text{ kgm}^{-3}$  density. This was found to be associated with the fact that all of those samples with high quality had less than 3% area porosity and fewer than 40 pores.

Similar results were obtained from the castings where different pouring heights were used. As seen from Figure 4.45, there is a clear difference in quality between top-poured, turbulently filled samples and those from bottom-filled, non-turbulent castings.

There are again two data points (I) and (II) that can be usefully selected as significant examples (Figure 4.45b). Point I has a quality index value 6.1, and II has 1.2. Interestingly, these have same density but have a significant difference in their quality index. The reason is that the sample with lower quality index has a shape factor of 0.34, a pore length of 1.17 mm and 22 pores. The other sample has 0.45 shape factor, 0.76 mm pore length and 10 pores. This means that the lower quality index sample has long and more elongated pores, and more of them. All the factors contribute negatively in this case.

All of these results illustrate that having a high density does not necessarily mean that the quality is correspondingly high. This is the result of the complex and relatively unpredictable behaviour of the bifilms. They may be fully straightened (but not yet opened) and so behaving as a crack, making little reduction in the density of the casting (Figure 4.9), but having a significant impact on properties. Alternatively, they maybe in a crumpled state, un-opened, having an overall small radius, again having a negligible effect on density, but this time not affecting the properties. A further scenario is when they are to some extent inflated, so that the density is reduced correspondingly; in this case properties will also be expected to be reduced, but to an extent depending on the shape of the partly opened bifilm.

Because the shape factor varied comparatively little (mostly within approximately a factor of 2) and even the pore size not much more than a factor of 10, an alternative approach was made to quantify the RPT simply by counting the number of pores. The number of pores varied by a factor of 100 or more, and was clearly the dominant effect. This number was assumed to be the indication of number of bifilms. In this later exercise, therefore Equation 3.7 was simplified to Equation 3.8.

A theoretical relationship between density and number of pores was plotted as shown in Figure 4.46. In Figure 4.46 (a) the three points 'a,' 'b' and 'c' are used as examples to explain why the size and shape of the pores are neglected in this version of the quality index. Considering first the two points 'a' and 'b' on the horizontal line: they have the same quality index number (both have one pore) but different densities ('a' has higher hydrogen). The second case is the vertical line: points 'b' and 'c'. They have the same density, but different quality index because although they have the same total volume of porosity, 'b' has 1 pore and 'c' has 20 pores. The results of the analysis with LM4 (Figure 4.47) showed that the relationship between the number of pores and the quality index was actually not capable of displaying a sensitive change with the density. As seen from Figure 4.47, the  $QI_3$  appears to follow a constant value below densities  $2500 \text{ kgm}^{-3}$ . Interestingly, this suggests a critical number of pores (per unit volume) such that beyond a certain level, the number of active nuclei does not change, but only the size of the pores increases. Possibly there exists a critical inter-pore spacing at a threshold level where hydrogen is diffused.

In the final approach, an alternative, and happily uncomplicated way of quantifying bifilms was proposed. The total length of bifilms was measured using the sum of the maximum lengths of all the pores on the sectioned surface of reduced pressure test samples. This quality index was named the '*Bifilm Index*' (Equation 3.9).

For a distribution of approximately uniform pores the index is simply the average maximum pore diameter multiplied by the total number of pores. The final index is a length, conveniently measured in millimetres.

The use of a simple total length measurement commends itself as a practical measure of quality in an industrial environment. It is recommended that the parameter be used in this simple and direct form. However, it is to be noted that this practical measure is really a length per standard area of polished surface. This is a curious measure from the point of view of a fundamental or scientific parameter. Thus for such purposes the more logical unit could be, for instance, the total area of bifilms per standard volume or weight of melt. Assuming random orientation of bifilms (probably not always true of course, but adequate for most purposes) a logical measure is:

$$\text{Bifilm quantity} = L_b^2 / \text{weight of sample} \quad (5.2)$$

where units are for instance mm<sup>2</sup>/100g Al. A variant of this approach would be to normalise the total bifilm length, using the length squared to give an effective area, divided by the area over which the measurement was made.

$$\text{Bifilm quantity} = L_b^2 / \text{area of sample} \quad (5.3)$$

This is a dimensionless quantity. This final quantification, whether in a final form such as defined by 5.2 or 5.3 above, was more direct than the previous attempts at quantification, being based on a simply understood length measurement. If the three low data points at 10 mbar at 900 C in Figure 4.49 were neglected, there is a rational relationship between bifilm index and density of the RPT samples. In fact low results in these conditions are to be expected as a result of bubble loss from the top surface of the RPT sample. Thus it seems

reasonable to conclude that the 10 mbar condition is not a reliable condition for the assessment of the bifilm index.

The more consistent results were observed in tests where 100 and 50 mbar were used in the RPT. As seen from Figure 4.52 (a), there are, on average, approximately three times the length of bifilms in top poured castings (138 mm at 100 mbar) compared to bottom filled castings (44 mm at 100 mbar) (corresponding approximately to 20,000 and 2000 mm<sup>2</sup>/100g or to 0.11 and 0.04 respectively).

The quality changes in the samples that were poured from different heights were discussed previously. It was clear that the top pouring system, where bifilms as well as entrapped air were introduced into the melt, had lower quality compared to a bottom filled system. This was to be expected. Most of the previous quality index studies had confirmed this result based on various dimensionless numbers. In this final approach, the quantification was more direct, being based on a simply appreciated length measurement. The worst casting in each case exhibited 240 compared to 140 mm bifilm index (Figure 4.52a).

These results were in good agreement with the studies when different numbers of diffusers were investigated in the holding furnace (Section 4.2.3). In that study, when the metal flow was controlled quiescently from the tapping point (slowly and no dross formation) and the launder was lowered to a minimum height for casting (Figure 3.5), it was seen that the quality was significantly increased (Figure 4.58). The average bifilm length values for non-quiescent conditions (SET 1) were 188 mm without diffusers and 100 mm with diffusers (Figure 4.56). These rather high results fell in quiescent conditions (SET 2) to 39 mm without, and 35 mm with diffusers (Figure 4.58).

It is also interesting to note that when the casting was carried out quiescently (achieved simply by the three changes investigated in this study), the average bifilm index values of SET 2 was below 50 mm even when no diffusers were used in the holding furnace (Figure 4.58). The 50 mm value therefore has been somewhat arbitrarily chosen here as a reasonable working threshold between good and bad qualities which was also seen in the studies with different casting heights where the average values for bottom filled castings were 44 mm and

48 mm for LM24 and LM25 respectively. It represents a target specification that can of course be tightened up as technique improves over time.

Any attempt to quantify the RPT using the estimation of the size of the originating bifilms in the liquid requires care. Clearly, large bifilms are observed as cracks, so their size, in terms of the length of crack, is straightforward to measure. Lengths measured in mm, up to even 10 or 15 mm, have been observed reasonably often during this study. However, for small bifilms, the precipitation of hydrogen can completely inflate the bifilm, or even over-inflate the bifilm thus eventually forming a bubble larger than the originating bifilm. Thus the diameters of spherical bubbles merely indicate an upper limit to the size of the originating defect. Because of this effect there is the danger that the bifilm index will be over-estimated, literally inflated. This threat to accuracy is felt to be relatively modest however. A doubling of the gas content of a spherical inclusion will enhance its size by  $2^{1/3} = 1.27$ . It seems unlikely that inflation by gas will often exceed such a value. In any event, any quantification within a factor of approximately 2 still appears to be useful. The total range of qualities assessable by the bifilm index appears to vary between something as small as perhaps 5 mm or less, up to a maximum in the region of 500 mm. Thus this factor of at least 100 in range means that the factor of 2 or so potential inaccuracy is acceptable in the sense that the result is still of great practical value.

It is clear that the unravelling of the bifilm, depending on the accidental and intricate geometries of the ravelled form, will be expected to show a wide range of difficulties, assisting to explain some of the wide scatter in results seen in this work. As was seen from Figure 4.62, it was really hard to find a relationship between the bifilm index proposed in this study and the hydrogen content of the melt. Hydrogen is evidently a contributor but still it has to be kept in mind that the unfurling and opening of a bifilm is a complicated, uncontrollable and unpredicted phenomena.

## **5.8 The relationship between number of pores, hydrogen and bifilm index**

Looking at the relationship between bifilm index and the number of the pores, if the theoretical points in Figure 4.61 are compared with the experimental findings in Figure 4.60,

it can be seen that points I and IV are not likely to be met. This suggests that there were no single large pores and there were no cases of hundreds of fine pores. All data seemed to lie in between such extremes.

However, when examining Points II and III, it has to be kept in mind that from the approach of Anson [129] (Figure 5.6), a single shrinkage pore could be observed as many small pores in two dimensions. So actually, that single shrinkage pore in Figure 5.6 could be a defect initiated by a single bifilm, but the number of pores would appear to be 5.

It is important to note that the bifilm index (total length of oxide) would still be the same no matter if it is observed as single pore or multiple fragments of that pore. Since it originated from one bifilm, only the number of the pores would change. Therefore a sophisticated image analysis would be required to further develop the contribution of the number of the pores to a future reliable quality index.

Turning now to the problem of the measurement of hydrogen and relating it with the density of RPT samples. This has been the central, if misguided, issue pursued by previous researchers as discussed earlier in this chapter. In addition, however, this raises the issue of the reliability of hydrogen measurement in the liquid aluminium carried out in this work.

In this study, the Hyscan technique was used to measure hydrogen levels. From one melt, different values of hydrogen levels were recorded ranging from 0.5 to 4.0 mL/kg Al (Figure 4.14) although for some cases this value was as high as 12.0 mL/kg Al (Figure 4.20). When the recorded values were put in chronological order from the start of the experiment to the end of the tests, the results showed that the hydrogen level in the melt was not constant nor consistent (Figure 5.7). LaOrchan *et al* [240] had used Alscan in their studies with the RPT. Alscan is, of course, a fundamental method and universally accepted as a reliable technique. These workers also observed the same scatter of hydrogen ranging from 0.5 to 3.5 mL/kg Al (Figure 5.2). The data collected from LaOrchan's results were compared with the findings from the current work in Figure 5.8. As seen from the figure, apart from a few high density values for high hydrogen level at the right top of the plot, the results agree, superimposing as

in the fit of a glove. This strongly suggests that there may be little wrong with the current Hyscan data.

In fact, in this study, an attempt was also made to correlate the results between Alscan and Hyscan. However, the Alscan test required 15 minutes whereas for Hyscan it was 5 minutes. In addition, Alscan required a costly probe which was dipped into the melt, often for several hours during the repeated measurements of the hydrogen. In the end, the wires that held the probe were melted and probe fell into the melt. As a consequence, the Alscan unit could only be used for 4 experiments before the probe needed to be changed. As a result, the use of Alscan for remainder of the tests was discarded.

It is important to keep in mind that the bifilm index is, of course, independent of the *measurement* of the hydrogen content of the melt. Thus measurement of the bifilm index is unaffected by the errors that can occur from hydrogen measurements. Ultimately, the RPT test and the bifilm index are the direct measure of potential defects that may degrade the properties of castings regardless of the measurement of the hydrogen level.

## 5.9 Image Analysis Studies

The use of X-ray radiography was first explored but soon abandoned because images of pores overlapped and confused the interpretation (Figure 4.30). Two dimensional image analyses of polished sections were found to be more straightforward. In this case, since the test was done in 2D, not all of the pores were included of course. However, plotting a graph between observed pore area and density showed a relatively close linear relationship at 100 mbar (Figure 4.39), indicating that the 2D approach would allow an estimate of the total volume of pores in the sample itself.

As was previously discussed, it was found that there was no dependence of shape factor on hydrogen and density (Figure 4.32-4.35, 4.41). This unexpected insensitivity of shape factor to shape changes that appeared clear to the unaided eye was difficult to understand. For this reason, an image analysis of basic geometric shapes of precisely known geometry using three different softwares was studied to test and to compare the accuracy and effectiveness of the

various packages. Results are summarised in Appendix II. These trials showed that the results of the different software systems were in reasonable agreement as illustrated in Figure 1 of Appendix II.

It was also found that the actual problem emerges from the complexity of digitised images. As seen from Figure 9 (Appendix II), a round pore can have intricate shaped edges at highest resolution resulting in 0.61 shape factor instead of a factor much more closer to 1. Possibly a further development is required in software engineering in this situation. If the image was analysed at a sufficiently fine resolution it is estimated that the shape factor would be accurately measured and the problem would be solved.

## 5.10 Optimum Pressure Considerations

As seen from the '*Bifilm Index*' studies, Figure 4.52b appears to give an apparently interesting spread of results. The 50 mbar residual pressure is sufficiently low that for some hydrogen contents the bifilms would have expanded to give bubbles sufficiently large to rise and escape at the surface of the sample during solidification under the reduced pressure. Thus the total porosity, and perhaps the total pore length also, is likely to be *underestimated*. Conversely, such low pressure will also be expected to expand bifilms to create bubbles of a diameter greater than the originating bifilm. Thus the total length of bifilms may be *overestimated*. There are therefore conflicting effects at very low residual pressure, causing the real bifilm sizes to be uncertain. It seems therefore that 50 mbar may be slightly too low a residual pressure to ensure the reliability of the results.

At very high residual pressures, particularly at atmospheric pressure, the bifilms are, of course, not detectable at all (Figure 4.9). This is the very reason for the use of reduced pressure. Clearly, therefore, an optimum pressure exists.

Even so, Figure 4.52a shows similar data but at an intermediate residual pressure of 100 mbar. This pressure cannot be far from an optimum, since bifilms are usually just easily visible, but many retain their crack-like form, and so clearly have not been over-expanded. The commonly used 75 mm Hg, currently widely used in the industry, corresponds almost exactly

to the 100 mbar used here. Thus, this commonly used standard is seen, happily, to be not far from this optimum. Confirmation of this tentatively proposed location of an optimum requires considerably more investigation than could be offered in this study. Work is required to establish a robust optimum that will deliver meaningful and reproducible results from a test that has so far only been criticised for its understandably wide scatter. However, the bifilm index is reasonably insensitive to pressure, and even now appears to give an assessment of quality better than any other reported quantifications of the RPT in the literature.

### **5.11 The Effect of Bifilms on Mechanical Properties**

The final aspect of this investigation was the comparison of the bifilm index with the mechanical test results. The design of the tensile test pattern was first investigated to ensure that the cast test bars would represent the quality of the sample ingots. It was important therefore to produce bars in which few defects were introduced during filling.

The comparison of mechanical properties from the two mould designs showed that the dominant benefit from quiescent filling is the ductility. The non-quiescent system had scattered elongation results while the quiescent filling showed remarkably consistent values (Figure 4.64b). This lends reassurance that the tests carried out with the optimised design of the test bar mould, in which the observed flow appeared to be optimum, are in fact relatively free of internal defects created during filling.

Nevertheless, before melting the ingots and casting them into moulds to produce bars, a simple check was carried out to ensure that the remelted and cast test bars gave results substantially similar to those machined directly from the ingots (Figure 4.65). For instance one might expect that the high volume of shrinkage in the ingots would affect the results so that there would be a difference between the cast and machined bars. In fact, it is rewarding to note that in fact no difference was observed; the results were closely similar.

In the following tests, the effect of different Mg contents on mechanical properties and bifilm index was investigated with alloy LM2. The first observation was the larger pore size of the samples with higher Mg (Figure 4.66). The proof stress increased with the higher Mg from

116 MPa to 149 MPa for bottom filled samples and from 121 MPa to 154 MPa for top poured samples (Table 4.4), which is hardly a significant increase in view of the natural scatter of these values. These effects of Mg may probably be taken as similar to the effects of Sr, since oxidation is enhanced, and Mg has a slight modification effect on the Al-Si eutectic. Some parallels with the action of Sr can be seen in other studies [84, 138, 192, 247].

In the mechanical test results of both low and high oxide contents, high Mg castings showed higher strength (Figure 4.70-4.72). This is to be expected from the action of Mg to strengthen the alloy by  $Mg_2Si$  precipitation, even though no heat treatment was carried out. However, it is interesting that the elongation results for the high Mg castings appeared to be low.

In fact, similar results were also reported by several workers [155, 251-254]. Dasgupta *et al* [255] found that the decrease in ductility (regardless of Mg content) was due to the absence of modified or fibrous eutectic structure. Nagel *et al* [256] found that the decrease in ductility may have to do with the Fe content, since an increase in the Fe content increased the number of  $\beta$ -AlFeSi which were held responsible for crack initiation sites. As it was shown by Cao [164, 165], Fe phases were nucleated on bifilms and it was the bifilms that initiated the crack. Caceres *et al* [22, 257] found in their study where they investigated the effect of casting defects on tensile properties that the dominant parameter was the area of fraction of defects in cross section, (regardless of their shape and distribution). Similar findings were observed on the SEM studies in Figure 4.74 a, d and e. The most likely explanation for these reported findings lies in the behaviour of bifilms.

It is suspected that the slightly increased bifilms, plus their rather thicker oxide that would be expected [258], plus perhaps a somewhat higher hydrogen content as a result of either a more permeable surface film or enhanced reactivity with environmental humidity, might all have contributed to thicker and more open bifilms that would have reduced ductility.

It can also be seen from the Weibull distributions (Figures 4.70-4.72) that in the low Mg alloy with low bifilm index (Table 4.4), the strength appears to be more consistent and repeatable. Conversely, in the high Mg alloy, the strength is generally higher, but the greater scatter

makes the castings more unreliable, and gives rise to some results significantly lower than those for low Mg.

In the studies with LM24 (Figure 4.75-4.76) where the casting sequence was examined, it was found that the chemistry of the alloy remained unchanged from start to finish (Table 4.3). However, initial strength values were low (PS = 119.95 MPa, UTS = 146.46 MPa), but towards the end of the casting the proof strength and the UTS increased by approximately 25 MPa to 145.64 MPa and 169.33 MPa respectively (Table 4.4). When the glass cloth filter (which was placed at the exit of launder prior to mould filling) was not used, the proof strength was 146.70 MPa, but the UTS value was increased to 159.75 MPa which was accompanied by a clear decrease in ductility from 0.45% (filtered) to 0.29% (unfiltered) (Table 4.4). This was expected, but the unexpected increase in proof strength was a clear and secure result. Although it is admitted that the volume fraction of bifilms is in this case extremely small (probably less than 0.1%) the oxide has an effect disproportionate to its volume fraction as a result of its huge area. Cross plots of the existing data are shown in Figure 4.77 where the observed effects of bifilms on the strength and elongation are summarised. The total number of tests carried out may seem unsatisfactorily low for statistical approval.

These findings in the mechanical test results of LM24 were analogous with the RPT studies in the holding furnace where different number of diffusers were run. In that case, when diffusers were not active, there was a decrease in the density of the RPT samples (Figure 4.27a) from start to the end and a considerable increase in the bifilm index (Figure 4.57a). The findings that the quality was decreasing towards to end of the melt are supported here by the mechanical test results.

## **5.12 Parameters Affecting the RPT Sensitivity**

Development of the reduced pressure test into a quantitative analysis technique for determining the metal quality requires full understanding of the system. The system consists of solidification under vacuum. This helps to reveal two detrimental effects of aluminium

alloys: hydrogen porosity and bifilm content. There are several parameters that may influence the effects and behaviour of these defects. They are summarised as follows:

#### ***5.12.1. Sample pouring temperature:***

Increasing the temperature increases gas absorption and the solubility of hydrogen in the liquid. Also as the temperature increases, the oxide structure is altered from amorphous to crystalline  $\gamma$ -phase and, if given time, might even convert to  $\alpha$ -phase. Thicker oxide gives elongated pores with a more rigid structure so that expansion is more restricted thereby leading to higher density. For reliable evaluation, it is suggested that the casting temperature and the holding time prior to sampling should be kept constant.

#### ***5.12.2. Microstructure:***

The metallurgy of the alloy is expected to affect pore size to some extent. Pores will grow until they impinge on the surrounding dendrites and therefore may develop a typical interdendritic shape. If the eutectic fraction is high, then these pores will appear round, instead of because of planar growth of the freezing front. These factors will all affect the size, shape and distribution of the pore and so in turn will affect the measured bifilm index. Even so, this effect is expected to be only of secondary importance.

#### ***5.12.3. Chamber pressure:***

Chamber pressure was a major study area since reducing the pressure increases the pore formation. However, at low vacuum levels, the differences in densities are widely distributed. Also the bursting of bubbles from the surface makes the test unreliable. At low vacuum level (200 mbar) the driving force to expand the air gap between bifilms is insufficient. 100 mbar is most likely to be closest to an optimum pressure. Pressures are easily, accurately and relatively inexpensively controlled, so that changes in the target pressure are not expected to limit the usefulness of the technique.

#### **5.12.4. Shrinkage:**

Surprisingly shrinkage does not appear to be an important factor in the medium to long freezing alloys studied in this work. If a sample is solidified under atmospheric pressure, the applied pressure collapses the top of the sample so that the effect of shrinkage is observed towards the top region of the sample. The interesting point is that the samples that are solidified under vacuum do not show any significant shrinkage in the same region. This may be because when solidification starts under vacuum, the bifilms that are located everywhere in the sample are now able to initiate pores that proceed to expand, countering any effect of shrinkage on solidification. As was seen from the sectioned surfaces of RPT samples, there are pores even very close to the mould walls.

#### **5.12.5. Melt gas content:**

The theoretical linear relationship between the density of a RPT sample and the gas content of the melt was not seen to be followed closely in the experimental trials. Since hydrogen – the only soluble gas in liquid aluminium - cannot nucleate either homogeneously or heterogeneously in the absence of bifilms, there would be no pores observed even when the samples were solidified under vacuum. However, in the presence of bifilms, the hydrogen would initially open them sufficiently to allow their length to be measured accurately. But excess hydrogen would encourage the bifilm to overextend, possibly growing to a pore of diameter much greater than the originating bifilm length. Thus, considering same amount of bifilms behaving in a same way at two different melts with different gas level, it is expected that a high hydrogen level will lead to an overestimation of the bifilm index.

## CHAPTER 6

### CONCLUSIONS

1) The present work confirms that the quantification of the RPT to yield estimates of hydrogen in solution by the use of density measurements is problematical, and despite previous claims, has not yet been achieved. The wide scatter of results is fundamental and necessary as a result of the presence and behaviour of bifilms. At the present time, the RPT appears to be of little use for the assessment of hydrogen content of the alloy.

2) Representative sampling of a casting by just using one RPT sample, although widely practiced, seems to be unreliable. From one 7 kg ingot, the bifilm index values may vary between 0 to 70 mm for one casting and between 40 to 350 mm for another casting made under known poorer conditions. This perceived disadvantage of an apparent lack of reproducibility of the RPT is in fact a reflection of the reality of the sampling problem of scattered defects in suspension in the melt. Since it is clear that a single sample will be inadequate, in practice it is probably to be recommended that at least three RPT samples should be taken to assess melt quality.

3) The development of a quality index using image analysis, where the number of pores, shape and length of the pores are included, is shown to have potential.

4) The Bifilm Index, the total length of bifilms on the sectioned surface of the RPT sample, appears to be the most promising technique. The measurement of samples solidified at 100 mbar residual pressure gave apparently reasonable, and possibly the most reliable results. It is expected therefore that the current industrial norm of 75 mm of mercury (practically identical to one tenth of an atmosphere, 100 mbar) will be confirmed to be an appropriate residual pressure for the reliable operation of this technique.

5) A increase the bifilm index (an increase in total bifilm area) is observed to be accompanied by a small fall in elongation but a small increase in strength. This is not understood.

- 6) When no diffusers were used in the holding furnace there was a deterioration in the quality of melt from the beginning to the end of the casting. The use of diffusers increased the metal quality.
  
- 7) The more quiescently the casting is controlled, the higher the quality of the products. Good control includes (i) careful minimisation of turbulence at tapping; (ii) minimised fall of the liquid; and (iii) filling conditions to reduce turbulence in the until the mould filling stage in a casting process.
  
- 8) The common criticism of the RPT as a poor technique for the assessment of hydrogen content is seen to be accurate for fundamental reasons. However, this is no reason to reject the test, since the test is valuable and robust for assessment of bifilms. It has the additional benefits of simplicity and low cost. Possibly together with Bifilm Number, Bifilm Index appear to be the most important fundamental parameters for the assessment of quality.
  
- 9) It is confirmed that the sectioned RPT technique, despite continuing to resist efforts until now to quantify it, remains a good check of metal quality.

## FUTURE WORK

- Carry out more tensile tests with different alloys and castings conditions to compare bifilm index change with mechanical properties. A valuable target would be the establishment of a map between bifilm index and RPT density, showing the contours of strength and ductility.
- Study image analysis software to determine precisely the parameters and to prepare a computer model to speed up the process.
- Study on the effects of modifiers (such as Sr, Mg etc) on oxide structure and pore morphology under reduced pressure test.
- An investigation on the development of the morphologies of the pores in the RPT samples taken from melts held in a (i) a resistance furnace (relatively slow convective stirring) and (ii) the induction furnace (powerful, rapid stirring).
- Re-processing of the RPT test results obtained from the thesis and with the data that is going to be collected from the future tests, a statistical technique will be used to analyse RPT results in order to find out how many samples should be taken from a melt to get a reliable assessment of the quality of the melt.

## Publications

### Journals

1. D. Dispınar, J. Campbell (2004). "Metal quality studies in secondary remelting of aluminium." *Journal of Institute of Cast Metals Engineers* **178** (3612): 78-86.
2. D. Dispınar, J. Campbell. (2004). "Critical Assessment of Reduced Pressure Test: Part I: Porosity Phenomena." *International Journal of Cast Metals Research* **17**(5) p 280-286.
3. D. Dispınar, J. Campbell. (2004). "Critical Assessment of Reduced Pressure Test: Part II: Quantification." *International Journal of Cast Metals Research* **17**(5) p 287-294.
4. D. Dispınar, J. Campbell (2004) "Étude de la qualité du métal lors de la refonte d'aluminium." *Hommages et Fonderie*, no 349, Novembre, pp. 18-24
5. D. Dispınar, J. Campbell (2004). "Metal quality studies in secondary remelting of aluminium." *Journal of Institute of Cast Metals Engineers Chinese Edition*, December pp. 22-25.
6. D. Dispınar, J. Campbell (2005). "Determination of Aluminium Melt Quality" *Aluminium India - A Quarterly published by AAI – Aluminium Association of India*,
7. D. Dispınar, J. Campbell. (2006). "Critical Assessment of Reduced Pressure Test: Part III: Mechanical Tests." *International Journal of Cast Metals Research...* accepted paper, to be published.
8. D. Dispınar, J. Campbell. (2006). "Tensile test pattern design for reliable mechanical test results of aluminium castings" *unpublished work*

### International Conferences

9. D. Dispınar, J. Campbell (2004). "Determination of Aluminium Melt Quality". *66<sup>th</sup> World Foundry Congress*, Istanbul.
10. D. Dispınar, J. Campbell (2005). "The Use of Bifilm Index as an Assessment of Metal Quality". *134<sup>th</sup> TMS Annual Meeting, Shape Casting: The John Campbell Symposium*, San Francisco, US, pp. 23-30
11. D. Dispınar, J. Campbell (2005), "Determination of aluminium casting quality using Bifilm Index" *12<sup>th</sup> International Metallurgy-Materials Congress and Fair*, Istanbul, Turkey
12. D. Dispınar, J. Campbell (2005), "Effect of diffusers on metal quality used in holding furnaces during recycling of aluminum" *12<sup>th</sup> International Metallurgy-Materials Congress and Fair*, Istanbul, Turkey.

13. D. Dispinar, J. Campbell (2006), "Effect of melting and casting conditions on aluminium alloy quality", *67<sup>th</sup> World Foundry Congress*, Harrogate, UK.

**National Conferences**

14. D. Dispinar, J. Campbell (2004). "Determination of metal quality during secondary remelting of aluminum" *10<sup>th</sup> Materials Symposium*, Denizli, Turkey, p.462-469
15. D. Dispinar, J. Campbell (2004). "Determining aluminium melt quality using reduced pressure test" *10<sup>th</sup> Materials Symposium*, Denizli, Turkey, p.523-531
16. D. Dispinar, J. Campbell (2006). "Effect of binder type and content on the porosity of aluminium castings in reduced pressure test" *11<sup>th</sup> Materials Symposium*, Denizli, Turkey, accepted paper

## References:

1. [www.eaa.net](http://www.eaa.net), *European Aluminum Association*.
2. C. Nyahumwa, N.R. Green, J. Campbell, *Effect of mold filling turbulence on fatigue properties of cast aluminum alloys*. AFS Transactions, 1998. **106**: p. 215-224.
3. C. Nyahumwa, N.R. Green, J. Campbell, *The concept of the fatigue potential of cast alloys*. Journal of Mechanical Behaviour of Metals, 1998. **9**(2): p. 227-235.
4. C.H. Caceres, T. Din, A.K.M.B. Rashid, J. Campbell, *The effect of ageing on Quality Index of an Al-Cu casting alloy*. Materials Science and Technology, 1999. **15**(June): p. 711-716.
5. Campbell, John, *Castings*. 2nd ed. 2003: Butterworth Heinemann, Oxford, UK.
6. J. Runyoro, S.M.A. Boutorabi, J. Campbell, *Critical gate velocities for film-forming casting alloys: a basis for process specification*. AFS Transactions, 1992. **100**: p. 225-234.
7. M. Rezvani, X. Yang, J. Campbell, *Effect of ingate design on strength and reliability of Al castings*. AFS Transactions, 1999. **107**: p. 181-188.
8. M. Tiryakioglu, J. Campbell, N.R. Green, *Review of reliable processes for aluminum aerospace castings*. AFS Transactions, 1996. **104**: p. 1069-1078.
9. N.R. Green, J. Campbell, *Influence of oxide film filling defects on the strength of Al-7Si-Mg alloy castings*. AFS Transactions, 1994. **102**: p. 341-347.
10. X. Dai, X. Yang, J. Campbell, J. Wood, *Effects of runner system design on the mechanical strength of Al-7Si-Mg alloy castings*. Materials Science and Engineering, 2003. **A354**: p. 315-325.
11. Tiryakioglu, M., J. Campbell and J. T. Staley, *Evaluating structural integrity of cast Al-7% Si-Mg alloys via work hardening characteristics: I. Concept of target properties*. Materials Science and Engineering A, 2004. **368**(1-2): p. 205-211.
12. Tiryakioglu, M., J. T. Staley and J. Campbell, *Evaluating structural integrity of cast Al-7%Si-Mg alloys via work hardening characteristics: II. A new quality index*. Materials Science and Engineering A, 2004. **368**(1-2): p. 231-238.
13. Kotzin, E.L., *Metalcasting & Molding Processes*, ed. Kotzin. 1981, Des Plaines, Illinois: American Foundrymen's Society.
14. [www.world-aluminium.org](http://www.world-aluminium.org), *International Aluminium Institute*.
15. R.W. Heine, C.R. Loper Jr., P.C. Rosenthal, *Principles of metal casting*. 2nd ed. 1967: McGraw-Hill Inc.
16. Burns, T.A., *The FOSECO foundryman's handbook*. 9th ed, ed. Burns. 1986, Tamworth: Pergamon Press.
17. Polmear, I.J., *Light Alloys*. 3rd ed. 1995, London: Arnold.
18. S. Makarov, D. Apelian, R. Ludwig, *Inclusion removal and detection in molten aluminum: mechanical, electromagnetic, and acoustic techniques*. AFS Transactions, 1999. **107**.
19. S. Makarov, R. Ludwig, D. Apelian, *Electromagnetic visualization technique for non-metallic inclusions in a melt*. Meas. Sci. Technol., 1999. **10**: p. 1-8.
20. Seniw, Mark E., James G. Conley and Morris E. Fine, *The effect of microscopic inclusion locations and silicon segregation on fatigue lifetimes of aluminum alloy A356 castings*. Materials Science and Engineering A, 2000. **285**(1-2): p. 43-48.
21. C.H. Caceres, B.I. Selling, *Casting defects and the tensile properties of an Al-Si-Mg alloy*. Materials Science and Engineering, 1996. **A220**: p. 109-116.

22. Caceres, C.H., *A rationale for the quality index of Al-Si-Mg casting alloys*. International Journal of Cast Metals Research, 1998. **10**: p. 293-299.
23. Kobayashi, T., *Strength and fracture of aluminum alloys*. Materials Science and Engineering A, 2000. **280**(1): p. 8-16.
24. Q.C. Wang, D. Apelian, D.A. Lados, *Fatigue behavior of A356-T6 aluminum cast alloys. Part I: effect of casting defects*. Journal of Light Metals, 2001. **1**: p. 73-84.
25. Q.C. Wang, D. Apelian, D.A. Lados, *Fatigue behavior of A356/357 aluminum cast alloys. Part II: effect of microstructural constituents*. Journal of Light Metals, 2001. **1**: p. 85-97.
26. R.C. Voigt, D.R. Bye, *Microstructural aspects of fracture in A356*. AFS Transactions, 1991. **99**: p. 33-50.
27. J.-Y. Buffiere, S. Savelli, P.H. Jouneau, E. Maire, R. Fougères, *Experimental study of porosity and its relation to fatigue mechanisms of model Al-Si7-Mg0.3 cast Al alloys*. Materials Science and Engineering, 2001. **A316**: p. 115-126.
28. A.A. Dabayeh, R.X. Xu, B.P. Du, T.H. Topper, *Fatigue of cast aluminum alloys under constant and variable-amplitude loading*. Int. J. Fatigue, 1996. **18**(2): p. 95-104.
29. Sokol'skaya, L.I., *Gases in Light Metals*, ed. Protheroe. 1961, London: Pergamon Press.
30. Glicksman, M.E., *Diffusion in solids*. 2000, New York: John Wiley & Sons Inc.
31. Fukatsu, N., N. Kurita, H. Shiga, Y. Murai and T. Ohashi, *Incorporation of hydrogen into magnesium aluminate spinel*. Solid State Ionics, 2002. **152-153**: p. 809-817.
32. D.E.J. Talbot, D.A. Granger, *Secondary hydrogen porosity in aluminum*. Journal of Institute of Metals, 1963-64. **92**: p. 290-297.
33. J. Weigel, E. Fromm, *Determination of hydrogen absorption and desorption processes in aluminum melts by continuous hydrogen activity measurement*. Metallurgical and Materials Transactions B, 1990. **21B**(October): p. 855-860.
34. C.E. Ransley, H. Neufeld, *The Solubility of Hydrogen in Liquid and Solid Aluminium*. Journal of Institute of Metals, 1947-48. **74**: p. 599-620.
35. Anyalebechi, P.N., *Attempts to predict hydrogen solubility limits in liquid multicomponent aluminum alloys*. Scripta Materialia, 1996. **34**(4): p. 513-517.
36. Anyalebechi, Prince N., *Analysis of the effects of alloying elements on hydrogen solubility in liquid aluminum alloys*. Scripta Metallurgica et Materialia, 1995. **33**(8): p. 1209-1216.
37. W.R. Opie, N.J. Grant, *Hydrogen solubility in aluminum and some aluminum alloys*. Transactions AIME - Journal of Metals, 1950. **188**(October): p. 1237-1241.
38. C.E. Ransley, D.E.J. Talbot, H.C. Barlow, *An instrument for measuring the gas content of aluminum alloys during melting and casting*. Journal of the Institute of Metals, 1957-58. **86**: p. 212-219.
39. C.E. Ransley, D.E.J. Talbot, *The routine determination of the hydrogen content of aluminum and aluminum alloys by the hot-extraction method*. Journal of the Institute of Metals, 1955-56. **84**: p. 445-452.
40. Talbot, D.E.J., *Effects of hydrogen in aluminum, magnesium, copper and their alloys*. International Metallurgical Reviews, 1975. **20**: p. 166-187.
41. O. Kubaschewski, B.E. Hopkins, *Oxidation of Metals*. 1967, London: Butterworths.
42. S. Impey, D.J. Stephenson, J.R. Nicholls, *A study of the effect of magnesium additions on the oxide growth morphologies on liquid aluminum alloys*. Microscopy of Oxidation, 1991: p. 238-244.

43. S. Impey, D.J. Stephenson, J.R. Nicholls. *The influence of surface preparation and pretreatments on the oxidation of liquid aluminum and aluminum-magnesium alloys.* in *Microscopy of Oxidation - Proceedings of the 2nd Int. Conf.* 1993. Cambridge, UK.
44. K. Shimizu, G.M. Brown, K. Kobayashi, P. Skeldon, G.E. Thompson, G.C. Wood, *High Temperature oxidation of an Al-0.5 wt% Mg alloy.* *Microscopy of Oxidation* 3, 1996: p. 396-405.
45. K. Shimizu, A. Gotoh, K. Kobayashi, G.E. Thompson, G.C. Wood, *The nucleation sites of  $\gamma$ -Al<sub>2</sub>O<sub>3</sub> crystals in thermal oxide films on aluminum.* *Proceedings of 1st Int. Conf. - Microscopy of Oxidation, 1991(Cambridge UK):* p. 144-148.
46. M.P. Silva, D.E.J. Talbot, *Oxidation of liquid aluminum-magnesium alloys.* *Light Metals*, 1989: p. 1035-1040.
47. Sleppy, W.C., *Oxidation of molten high-purity aluminum in dry oxygen.* *Journal of the Electrochemical Society*, 1961. **108**(12): p. 1097-1102.
48. G. Wightman, D.J. Fray, *The Dynamic oxidation of aluminum and its alloys.* *Metallurgical and Materials Transactions B*, 1983. **14B**(December): p. 625-631.
49. S.A. Impey, D.J. Stephenson, J.R. Nicholls, *Mechanism of scale growth on liquid aluminum.* *Materials Science and Technology*, 1988. **4**(December): p. 1126-1132.
50. Dignam, M.J., *Oxide films on aluminum I. Ionic conduction and structure.* *Journal of the Electrochemical Society*, 1962. **109**(3): p. 187-191.
51. Dignam, M.J., *Oxide films on aluminum II. Kinetics of Formation in Oxygen.* *Journal of the Electrochemical Society*, 1962. **109**(3): p. 192-198.
52. F. d'Heurle, L. Berenbaum, R. Rosenberg, *On the structure of aluminum films.* *Transactions AIME*, 1968. **242**(March): p. 502-511.
53. G.M. Scamans, E.P. Butler, *In situ observations of crystalline oxide formation during aluminum and aluminum alloy oxidation.* *Metallurgical and Materials Transactions A*, 1975. **6A**(November): p. 2055-2063.
54. L.P.H. Juergens, W.G. Sloof, F.D. Tichelaar, E.J. Mittemeijer, *Thermodynamic stability of amorphous oxide films on metals: Application to aluminum oxide films on aluminum substrates.* *Physical Review B*, 2000. **62**(7): p. 4707-4719.
55. L.P.H. Juergens, W.G. Sloof, F.D. Tichelaar, E.J. Mittemeijer, *Composition and chemical state of the ions of aluminum-oxide films formed by thermal oxidation of aluminum.* *Surface Science*, 2002. **506**: p. 313-332.
56. L.P.H. Juergens, W.G. Sloof, F.D. Tichelaar, E.J. Mittemeijer, *Growth kinetics and mechanisms of aluminum-oxide films formed by thermal oxidation of aluminum.* *Journal of Applied Physics*, 2002. **92**(3): p. 1649-1656.
57. L.P.H. Juergens, W.G. Sloof, F.D. Tichelaar, E.J. Mittemeijer, *Structure and morphology of aluminum-oxide films formed by thermal oxidation of aluminum.* *Thin Solid Films*, 2002. **418**: p. 89-101.
58. R. Fuoco, E.R. Correa, M. de A Bastos, L.S. Escudero, *Characterization of some types of oxide inclusions in aluminum alloy castings.* *AFS Transactions*, 1999. **107**: p. 287-294.
59. C.N. Cochran, D.L. Belitskus, D.L. Kinosz, *Oxidation of aluminum-magnesium melts in air, oxygen, flue gas, and carbon dioxide.* *Metallurgical and Materials Transactions B*, 1977. **8B** (June): p. 323-332.
60. D.J. Field, G.M. Scamans, E.P. Butler, *The high temperature oxidation of Al-4.2 wt Pct Mg alloy.* *Metallurgical and Materials Transactions A*, 1987. **18A**(March): p. 463-472.

61. J.A.S. Tenorio, D.C.R. Espinosa, *High-temperature oxidation of Al-Mg Alloys*. Oxidation of Metals, 2000. **53** (3/4): p. 361-373.
62. K. Shimizu, G.M. Brown, K. Kobayashi, P. Skeldon, G.E. Thompson, G.C. Wood, *The early stages of high temperature oxidation of an Al-0.5wt% Mg alloy*. Corrosion Science, 1998. **40** (4-5): p. 557-575.
63. Crepeau, P.N. *Molten aluminum contamination: gas, inclusions, and dross*. in *Proceedings of the 5th International Conference on Molten Aluminum Processing*. 1995. USA, Des Plaines: AFS Inc.
64. A. Nylund, K. Mizuno, I. Olefjord, *Influence of Mg and Si on the oxidation of Aluminum*. Oxidation of Metals, 1998. **50** (314): p. 309-325.
65. I. Haginoya, T. Fukusako, *Oxidation of molten Al-Mg alloys*. Transactions of the Japan Institute of Metals, 1983. **24** (9): p. 613-619.
66. Wakefield, G. R. and R. M. Sharp, *The composition of oxides formed on Al-Mg alloys*. Applied Surface Science, 1991. **51** (1-2): p. 95-102.
67. Venugopalan, H., K. Tankala and T. DebRoy, *Kinetics of directed oxidation of Al-Mg alloys in the initial and final stages of synthesis of Al<sub>2</sub>O<sub>3</sub>/Al composites*. Materials Science and Engineering A, 1996. **210** (1-2): p. 64-75.
68. L. Rault, M. Allibert, A. Dubus, *In situ study of liquid Al-Mg alloys oxidation*. Materials Science Forum, 1996. **217-222**: p. 165-170.
69. L. Rault, M. Allibert, M. Rrin, A. Dubus, *Oxidation of liquid aluminum-magnesium alloys in moist air*. Light Metals, 1996: p. 345-355.
70. L.-W. Huang, W.-J. Shu, T.-S. Shih, *Diagnosis and analysis of oxide film in Al-Si-Mg alloys*. AFS Transactions, 2000. **108**: p. 547-560.
71. W.M. Zhong, G.L'Esperance, M. Suery, *Interfacial reactions in Al-Mg (5083)/Al<sub>2</sub>O<sub>3</sub>p composites during fabrication and remelting*. Metallurgical and Materials Transactions A, 1995. **26A** October: p. 2625-2635.
72. Do, T., S. J. Splinter, C. Chen and N. S. McIntyre, *The oxidation kinetics of Mg and Al surfaces studied by AES and XPS*. Surface Science, 1997. **387** (1-3): p. 192-198.
73. C. Chen, S.J. Splinter, T. Do, N.S. McIntyre, *Measurement of oxide film growth on Mg and Al surfaces over extended periods using XPS*. Surface Science, 1997. **382**: p. 652-657.
74. Srinivasa Rao, B. and V. Jayaram, *Pressureless infiltration of Al-Mg based alloys into Al<sub>2</sub>O<sub>3</sub> preforms: mechanisms and phenomenology*. Acta Materialia, 2001. **49** (13): p. 2373-2385.
75. A. Munitz, M. Metzger, R. Mehribian, *The interface phase in Al-Mg/Al<sub>2</sub>O<sub>3</sub> composites*. Metallurgical Transactions A, 1979. **10A** (October): p. 1491-1497.
76. Campbell, J., *Critical gate velocity for film-forming casting alloys: A basis for process specification*. AFS Transactions, 1992. **100**: p. 225-234.
77. Campbell, J., *Invisible macrodefects in castings*. Journal de Physique IV, 1993. **3**(November): p. 861-872.
78. Campbell, J. *The origin of porosity in castings*. in *4th Asian Foundry Conference*. 1996.
79. Campbell, J. *The entrainment defect: the new metallurgy*. in *Advances in the Metallurgy of Aluminum Alloys, Proceedings of the James T. Staley Symposium on Aluminum*. 2001: ASM International.
80. Campbell, J., *Pore nucleation in solidifying metals*. Iron and Steel Institute, 1968: p. 19-26.

81. Rooy, E.L., *Mechanisms of porosity formation in aluminum*. Modern Casting, 1992 (September): p. 34-36.
82. Fisher, J.C., *The fracture of liquids*. Journal of Applied Physics, 1948. **19** (November): p. 1062-1067.
83. A. Kaye, A. Street, *Die Casting Metallurgy*. 1982, London: Butterworth.
84. D. Emadi, J.E. Gruzleski, M. Pekguleryuz, *Melt oxidation behavior and inclusion content in unmodified and Sr-modified A356 alloy- their role in pore nucleation*. AFS Transactions, 1996. **104**: p. 763-768.
85. C.J. Simenson, G. Berg, *A survey of inclusions in aluminum*. Aluminium, 1980. **56**: p. 335-340.
86. A.M. Samuel, F.H. Samuel, *Porosity factor in quality aluminum castings*. AFS Transactions, 1992. **100**: p. 657-666.
87. P.S. Mohanty, F.H. Samuel, J.E. Gruzleski, *Experimental study on pore nucleation by inclusions in aluminum castings*. AFS Transactions, 1995. **103**: p. 555-564.
88. G. Laslaz, P. Laty, *Gas porosity and metal cleanliness in aluminum casting alloys*. AFS Transactions, 1991. **99**: p. 83-90.
89. X.-G. Chen, S. Engler, *Formation of gas porosity in aluminum alloys*. AFS Transactions, 1994. **102**: p. 673-682.
90. D. See, R.C. Atwood, P.D. Lee, *A comparison of three modeling approaches for the prediction of microporosity in aluminum-silicon alloys*. Journal of Materials Science, 2001. **36**: p. 3423-3435.
91. P.D. Lee, J.D. Hunt, *Hydrogen porosity in directional solidified aluminium-copper alloys: in situ observation*. Acta Materialia, 1997. **45** (10): p. 4155-4169.
92. P.D. Lee, J.D. Hunt, *Measuring the nucleation of hydrogen porosity during the solidification of aluminium-copper alloys*. Scripta Materialia, 1997. **36** (4): p. 399-404.
93. Lee, P. D. and J. D. Hunt, *Hydrogen porosity in directional solidified aluminium-copper alloys: in situ observation*. Acta Materialia, 1997. **45** (10): p. 4155-4169.
94. Lee, P. D. and J. D. Hunt, *Hydrogen porosity in directionally solidified aluminium-copper alloys: a mathematical model*. Acta Materialia, 2001. **49** (8): p. 1383-1398.
95. Lee, P. D., A. Chirazi and D. See, *Modeling microporosity in aluminum-silicon alloys: a review*. Journal of Light Metals, 2001. **1** (1): p. 15-30.
96. Lee, P. D., R. C. Atwood, R. J. Dashwood and H. Nagaumi, *Modeling of porosity formation in direct chill cast aluminum-magnesium alloys*. Materials Science and Engineering A, 2002. **328** (1-2): p. 213-222.
97. Lee, P. D., A. Chirazi, R. C. Atwood and W. Wang, *Multiscale modelling of solidification microstructures, including microsegregation and microporosity, in an Al-Si-Cu alloy*. Materials Science and Engineering A, 2004. **365** (1-2): p. 57-65.
98. R.C. Atwood, S. Sridhar, P.D. Lee, *Equations for nucleation of hydrogen gas pores during solidification of aluminum seven weight percent silicon alloy*. Scripta Materialia, 1999. **41** (12): p. 1255-1259.
99. R.C. Atwood, S. Sridhar, W. Zhang, P.D. Lee, *Diffusion-controlled growth of Hydrogen pores in Aluminium-Silicon Castings: in situ observation and modelling*. Acta Materialia, 2000. **48**: p. 405-417.
100. R.C. Atwood, P.D. Lee. *A Combined Cellular Automaton and Diffusion Model for the Prediction of Porosity Formation During Solidification*. in *Mod. Cast. Weld. & Adv. Sol. Proc. IX*. 2000. Aachen, Germany.

101. R.C. Atwood, P.D. Lee, *Simulation of the three-dimensional morphology of solidification porosity in an aluminum-silicon alloy*. Acta Materialia, 2003. **51**: p. 5447-5466.
102. D. Argo, J.E. Gruzleski, *Porosity in modified aluminum alloy castings*. AFS Transactions, 1988. **96**: p. 65-74.
103. D.R. Poirier, K. Yeum, A.L. Maples, *A Thermodynamic Prediction for Microporosity Formation in Aluminium-rich Al-Cu Alloys*. Metallurgical and Materials Transactions B, 1987. **18A** (November): p. 1979-1987.
104. D.R. Poirier, P.K. Sung, S.D. Felicelli, *A continuum model of microporosity in an aluminum casting alloy*. AFS Transactions, 2001. **109**: p. 379-395.
105. D.R. Poirier, P.K. Sung, *Thermodynamics of hydrogen in Al-Si alloys*. Metallurgical and Materials Transactions A, 2002. **33A** (December): p. 3874-3876.
106. Conley, James G., Julie Huang, Jo Asada and Kenji Akiba, *Modeling the effects of cooling rate, hydrogen content, grain refiner and modifier on microporosity formation in Al A356 alloys*. Materials Science and Engineering A, 2000. **285** (1-2): p. 49-55.
107. J. Huang, T. Mori, J.C. Conley, *Simulation of Microporosity Formation in Modified and Unmodified A356 Alloy Castings*. Metallurgical and Materials Transactions B, 1998. **29B** (December): p. 1249-1260.
108. T.S. Piwonka, M.C. Flemings, *Pore formation in solidification*. Transactions of the Metallurgical Society of AIME, 1966. **236** (August): p. 1157-1165.
109. K. Kubo, R.D. Pehlke, *Mathematical Modeling of Porosity Formation in Solidification*. Metallurgical and Materials Transactions B, 1985. **16B** (June): p. 359-366.
110. Lee, M. H., J. J. Kim, K. H. Kim, N. J. Kim, S. Lee and E. W. Lee, *Effects of HIPping on high-cycle fatigue properties of investment cast A356 aluminum alloys*. Materials Science and Engineering A, 2003. **340** (1-2): p. 123-129.
111. Lee, P. D. and J. D. Hunt, *Measuring the nucleation of hydrogen porosity during the solidification of aluminium-copper alloys*. Scripta Materialia, 1997. **36** (4): p. 399-404.
112. Lee, P. D., A. Mitchell, A. Jardy and J.-P. Bellot, *Liquid metal processing and casting*. Journal of Materials Science, 2004. **39** (24): p. 7133.
113. Lee, S. M. and C. P. Hong, *Effects of wheel surface condition on solidification behavior and columnar grain growth in Al-4.3wt%Cu ribbons*. Scripta Materialia, 1997. **37**(2): p. 165-171.
114. Lee, W. B., Y. M. Yeon and S. B. Jung, *The improvement of mechanical properties of friction-stir-welded A356 Al alloy*. Materials Science and Engineering A, 2003. **355** (1-2): p. 154-159.
115. Lee, Y. C., A. K. Dahle, D. H. StJohn and J. E. C. Hutt, *The effect of grain refinement and silicon content on grain formation in hypoeutectic Al-Si alloys*. Materials Science and Engineering A, 1999. **259** (1): p. 43-52.
116. P.D. Lee, A. Chirazi, R.C. Atwood, W.Wang, *Multiscale modelling of solidification microstructures, including microsegregation and microporosity, in an Al-Si-Cu alloy*. Materials Science and Engineering, 2004. **A365**: p. 57-65.
117. P.D. Lee, R.C. Atwood, R.J. Dashwood, H. Nagaumi, *Modeling of porosity formation in direct chill cast aluminum-magnesium alloys*. Materials Science and Engineering, 2002. **A328**: p. 213-222.
118. Knuutinen, A., K. Nogita, S. D. McDonald and A. K. Dahle, *Modification of Al-Si alloys with Ba, Ca, Y and Yb*. Journal of Light Metals, 2001. **1** (4): p. 229-240.

119. Knuutinen, A., K. Nogita, S. D. McDonald and A. K. Dahle, *Porosity formation in aluminium alloy A356 modified with Ba, Ca, Y and Yb*. Journal of Light Metals, 2001. **1** (4): p. 241-249.
120. Nogita, K., A. Knuutinen, S. D. McDonald and A. K. Dahle, *Mechanisms of eutectic solidification in Al-Si alloys modified with Ba, Ca, Y and Yb*. Journal of Light Metals, 2001. **1** (4): p. 219-228.
121. J.A. Taylor, D.A. Graham, M.A. Easton, *Redistribution of shrinkage porosity in eutectic Al-Si alloy by addition of Ti-B grain refiner*. AFS Transactions, 1999. **107**: p. 189-195.
122. J.A. Taylor, G.B. Schaffer, D.H. StJohn, *Shrinkage Porosity Formation in Iron-containing Al-Si-Cu-Mg Casting Alloys*. AFS Transactions, 1997. **105**: p. 23.
123. M.O. Otte, S.D. McDonald, J.A. Taylor, D.H. StJohn, W. Schneider, *Controlling porosity-related casting rejects: understanding the role of iron in Al-Si alloy*. AFS Transactions, 1999. **107**: p. 471-478.
124. S.D. McDonald, A.K. Dahle, J.A. Taylor, D.H. St. John, J.W. Zindel, *Microstructural evolution of an Al-Si-Mg foundry alloy during solidification*. Die Casting Conference, 2000(Melbourne, Australia).
125. S.D. McDonald, K. Nogita, A.K. Dahle, J.A. Taylor, D.H. StJohn, *Eutectic solidification and porosity formation in Al-Si alloys: Role of strontium*. AFS Transactions, 2000. **108**: p. 463-470.
126. P.S. Mohanty, F.H. Samuel, J.E. Gruzleski, *Mechanism of heterogeneous nucleation of pores in metals and alloys*. Metallurgical Transactions, 1993. **24A** (August): p. 1845-1856.
127. J.P. Anson, J.E. Gruzleski, *Effect of Hydrogen Content on Relative Shrinkage and Gas Microporosity in Al-7% Si Casting*. AFS Transactions, 1999. **107**: p. 135-142.
128. J.P. Anson, M. Stucky, J.E. Gruzleski, *Effect of Sr modification on nucleation and growth of microporosity during the solidification of Al-7%Si foundry alloy*. AFS Transactions, 2000. **108**: p. 419-426.
129. Anson, J. P. and J. E. Gruzleski, *The Quantitative Discrimination between Shrinkage and Gas Microporosity in Cast Aluminum Alloys Using Spatial Data Analysis*. Materials Characterization, 1999. **43** (5): p. 319-335.
130. D. Emadi, J.E. Gruzleski, *Effects of casting and melt variables on porosity in directionally-solidified Al-Si alloys*. AFS Transactions, 1994. **102**: p. 307-312.
131. D. Emadi, J.E. Gruzleski, *Combating Al-Si Porosity: the Strontium/Hydrogen Myth*. Modern Casting, 1995(March): p. 46-47.
132. D. Emadi, J.E. Gruzleski, J.M. Toguri, *The effect of Na and Sr modification on surface tension and volume shrinkage of A356 alloy and their influence on porosity formation*. Metallurgical and Materials Transactions B, 1993. **24B** (December): p. 1055-1063.
133. W. LaOrchan, J.E. Gruzleski, *Grain refinement, modification and melt hydrogen-their effects on microporosity, shrinkage and impact properties in A356 alloy*. AFS Transactions, 1992. **100**: p. 415-424.
134. P.M. Thomas, J.E. Gruzleski, *Threshold hydrogen fo pore formation during solidification of aluminum alloys*. Metallurgical and Materials Transactions B, 1978. **9B** (March): p. 139-141.
135. A.M. Samuel, F.H. Samuel, *A metallographic study of porosity and fracture behaviour in relation to the tensile properties in 319.2 end chill castings*. Metallurgical and Materials Transactions A, 1995. **26A** (September): p. 2359-2372.

136. A.M. Samuel, F.H. Samuel, *The reduced pressure test as a measuring tool in the evaluation of porosity/hydrogen content in Al-7 wt pct Si-10 vol pct SiC(p) metal matrix composite*. Metallurgical and Materials Transactions A, 1993. **24A** (August): p. 1857-1868.
137. N. Roy, A.M. Samuel, F.H. Samuel, *Porosity formation in Al-9 wt pct S-3 wt pct Cu alloy systems: metallographic observations*. Metallurgical and Materials Transactions A, 1996. **27A** (February): p. 415-429.
138. L. Liu, A.M. Samuel, F.H. Samuel, H.W. Doty, S. Valtierra, *Role of strontium oxide on porosity formation in Al-Si casting alloys*. AFS Transactions, 2002. **110**: p. 449-462.
139. Samuel, A. M., A. Gotmare and F. H. Samuel, *Effect of solidification rate and metal feedability on porosity and SiC/Al<sub>2</sub>O<sub>3</sub> particle distribution in an Al-Si-Mg (359) alloy*. Composites Science and Technology, 1995. **53** (3): p. 301-315.
140. S.N. Tiwari, J. Beech, *Origin of gas bubbles in aluminum*. Metal Science, 1978(August): p. 356-362.
141. Li, Y. M. and R. D. Li, *Effect of the casting process variables on microporosity and mechanical properties in an investment cast aluminium alloy*. Science and Technology of Advanced Materials, 2001. **2** (1): p. 277-280.
142. Li, Z., A. M. Samuel, F. H. Samuel, C. Ravindran, S. Valtierra and H. W. Doty, *Parameters controlling the performance of AA319-type alloys: Part I. Tensile properties*. Materials Science and Engineering A, 2004. **367** (1-2): p. 96-110.
143. Li, Kun-Dar and Edward Chang, *Mechanism of nucleation and growth of hydrogen porosity in solidifying A356 aluminum alloy: an analytical solution*. Acta Materialia, 2004. **52** (1): p. 219-231.
144. K.D. Li, E. Chang, *An analysis on porosity formation in A356 aluminum alloy castings*. International Journal of Cas Metals Res., 2002. **15**: p. 25-30.
145. K.-D. Li, E. Chang, *A modified mechanism of porosity formation in A356 alloy permanent mold casting*. AFS Transactions, 2002. **110**: p. 331-338.
146. X.-G. Chen, S. Engler, *Measuring hydrogen content in molten aluminum alloys using the CHAPEL technique*. Cast Metals, 1993. **6** (2): p. 99-108.
147. Ch. Pequet, M. Rappaz. *Modeling of porosity formation during the solidification of aluminum alloys using a mushy zone refinement method*. in *Modeling of Casting, Welding and Advanced Solidification Processes IX*. 2000. Aachen, Germany.
148. A.V. Kuznetsov, K. Vafai, *Development and investigation of three-phase model of the mushy zone for analysis of porosity formation in solidifying castings*. International Journal of Heat Mass Transfer, 1995. **38** (14): p. 2557-2567.
149. K. Yeum, D.R. Poirier, *Predicting Microporosity in Aluminum Alloys*. Light Alloys, 1988: p. 469-476.
150. M. Serratos, D.R. Poirier, W. Lyman, *Effect of stirring on oxide skins and porosity in A356 aluminum alloy*. AFS Transactions, 2000. **108**: p. 719-724.
151. G.K. Sigworth, C. Wang, *Evolution of Porosity during Solidification, Part 2: A Theoretical Analysis*. AFS Transactions, 1992. **100**: p. 989-1004.
152. G.K. Sigworth, C. Wang, *Evolution of Porosity during solidification, Part 1: A Literature Review*. AFS Transactions, 1992. **100**: p. 191- 987.
153. G.K. Sigworth, C. Wang, *Evolution of Porosity in Long Freezing Range Alloys*. Metallurgical and Materials Transactions B, 1993. **24B** (April): p. 365-377.

154. G.K. Sigworth, C. Wang, *Mechanisms of Porosity Formation during Solidification: A Theoretical Analysis*. Metallurgical and Materials Transactions B, 1993. **24B** (April): p. 349-364.
155. G.K. Sigworth, S. Shivkumar, D. Apelian, *The influence of molten metal processing on mechanical properties of cast Al-Si-Mg alloys*. AFS Transactions, 1989. **99**: p. 811-824.
156. G.K. Sigworth, T.A. Engh, *Chemical and kinetic factors related to hydrogen removal from aluminum*. Metallurgical and Materials Transactions B, 1982. **13B** (September): p. 447-460.
157. K.J. Brondyke, P.D. Hess, *Interpretation of vacuum gas test results for aluminum alloys*. Transactions AIME, 1964. **230** (December): p. 1542-1546.
158. S. Fox, J. Campbell, *Visualisation of oxide film defects during solidification of aluminum alloys*. Scripta Materialia, 2000. **43**: p. 881-886.
159. S. Fox, J. Campbell. *Liquid metal quality*. in *Proceedings of Filling and Feeding of Castings*. 2001. Birmingham UK.
160. S. Fox, J. Campbell, *Internat. Journal of Cast Metals Research*, 2002. **14**(6): p. 335-340.
161. Campbell, J., *Hydrostatic tensions in solidifying materials*. Transactions of the Metallurgical Society of AIME, 1968. **242** (February): p. 264-267.
162. Campbell, J., *Hydrostatic tensions in solidifying alloys*. Transactions of the Metallurgical Society of AIME, 1968. **242** (February): p. 268-271.
163. E.J. Whittenberger, F.N. Rhines, *Origin of porosity in castings of magnesium-aluminum and other alloys*. Transactions AIME - Journal of Metals, 1952(April): p. 409-420.
164. X. Cao, J. Campbell, *Effect of precipitation of primary intermetallic compounds on tensile properties of cast Al-11.5Si-0.4Mg alloy*. AFS Transactions, 2000. **108**: p. 391-400.
165. X. Cao, J. Campbell, *The nucleation of Fe-rich phases on oxide films in Al-11.5Si-0.4-Mg cast alloys*. Metallurgical and Materials Transactions A, 2003. **34A** (July): p. 1409-1420.
166. N.D.G. Mountford, R. Calvert, *Precipitation effects in liquid aluminum alloys*. Journal of the Institute of Metals, 1959-60. **88**: p. 121-127.
167. Nagaumi, Hiromi, *Prediction of porosity contents and examination of porosity formation in Al-4.4%Mg DC slab*. Science and Technology of Advanced Materials, 2001. **2** (1): p. 49-57.
168. D.R. Poirier, R. Speiser, *Surface tension of aluminum rich Al-Cu liquid alloys*. Metallurgical and Materials Transactions A, 1987. **18A** (June): p. 1156-1160.
169. J. Zou, S. Shivkumar, D. Apelian, *Modeling of microstructure evolution and microporosity formation on cast aluminum alloys*. AFS Transactions, 1990. **98**: p. 871-878.
170. S. Shivkumar, D. Apelian, J. Zou, *Modeling microstructure evolution and microporosity formation in cast aluminum alloys*. AFS Transactions, 1990. **98**: p. 897-904.
171. V. Laurent, C. Rigaut, *Experimental and Numerical Study of Criteria Functions for Predicting Microporosity in Cast Aluminium Alloys*. AFS Transactions, 1992. **100**: p. 647-655.

172. P. Rousset, M. Rappaz, B. Hannart, *Modeling of Inverse Segregation and Porosity Formation in Directionally Solidified Aluminium Alloys*. Metallurgical and Materials Transactions A, 1995. **26A** (September): p. 2349-2358.
173. V.R. Voller, S. Sundarraaj, *A model of inverse segregation: the role of microporosity*. International Journal of Heat Mass Transfer, 1995. **38** (6): p. 1009-1018.
174. B. Szpunar, R.W. Smith, *Monte Carlo simulation of solidification processes; porosity*. Canadian Metallurgical Quarterly, 1996. **35** (3): p. 299-303.
175. Jeong, Hyunjo and David K. Hsu, *Quantitative estimation of material properties of porous ceramics by means of composite micromechanics and ultrasonic velocity*. NDT & E International, 1996. **29** (2): p. 95-101.
176. K. Jahrling, S. Tait, *Measurements of the evolution of porosity in a mushy layer*. Journal of Crystal Growth, 1996. **167**: p. 285-291.
177. M. Bobeth, M. Gutkin, W. Pompe, A.E. Romanov, *Modelling of vacancy diffusion and pore formation during parabolic oxide growth*. Phys. Stat. Sol. A, 1998. **165**: p. 165-184.
178. Matan, N., H. M. A. Winand, P. Carter, M. Karunaratne, P. D. Bogdanoff and R. C. Reed, *A coupled thermodynamic/kinetic model for diffusional processes in superalloys*. Acta Materialia, 1998. **46** (13): p. 4587-4600.
179. Stoehr, Robert A., *Modeling the influence of fluid flow on the development of porosity and microstructure in castings*. Canadian Metallurgical Quarterly, 1998. **37**(3-4): p. 179-184.
180. J.A. Taylor, G.B. Schaffer, D.H. StJohn, *The role of iron in the formation of porosity in Al-Si-Cu based casting alloys: Part III. A microstructural model*. Metallurgical and Materials Transactions A, 1999. **30A**(June): p. 1657-1662.
181. Atwood, R. C., S. Sridhar, W. Zhang and P. D. Lee, *Diffusion-controlled growth of hydrogen pores in aluminium-silicon castings: in situ observation and modelling*. Acta Materialia, 2000. **48**(2): p. 405-417.
182. Q. Chen, C. Ravindran, *Effect of hydrogen content and solidification time on porosity formation in LFCs of A356 Alloy- A semi-empirical model*. AFS Transactions, 2000. **108**: p. 297-303.
183. Buffiere, J-Y., S. Savelli, P. H. Jouneau, E. Maire and R. Fougères, *Experimental study of porosity and its relation to fatigue mechanisms of model Al-Si7-Mg0.3 cast Al alloys*. Materials Science and Engineering A, 2001. **316** (1-2): p. 115-126.
184. See, D., R. C. Atwood and P. D. Lee, *A comparison of three modeling approaches for the prediction of microporosity in aluminum-silicon alloys*. Journal of Materials Science, 2001. **36** (14): p. 3423-3435.
185. Sung, P. K., D. R. Poirier, S. D. Felicelli, E. J. Poirier and A. Ahmed, *Simulations of microporosity in IN718 equiaxed investment castings*. Journal of Crystal Growth, 2001. **226** (2-3): p. 363-377.
186. M. McLaughlin, C.-W. Kim, K. Kubo, *An Application of Porosity Simulation to an Aluminum Automotive Suspension Component*. AFS Transactions, 2002. **110**: p. 223-236.
187. Melo, M. L. N. M., E. M. S. Rizzo and R. G. Santos, *Numerical model to predict the position, amount and size of microporosity formation in Al-Cu alloys by dissolved gas and solidification shrinkage*. Materials Science and Engineering A, 2004. **374** (1-2): p. 351-361.
188. Burchell, V.H., *The influence of gas content induced by poling on the properties of some aluminum alloys*. The British Foundryman, 1969 (April): p. 138-169.

189. X. Bian, Z. Zhang, X. Liu, *Effect of strontium modification on hydrogen content and porosity shape of Al-Si alloys*. Materials Science Forum, 2000. **331-337**: p. 361-366.
190. R. Fuoco, H. Goldenstein, J.E. Gruzleski, *Evaluation of Effect of Modification-induced eutectic undercooling on microporosity formation in 356 Al Alloy*. AFS Transactions, 1994. **102**: p. 297-306.
191. H. Iwahori, K. Yonekura, Y. Yamamoto, M. Nakamura, *Occuring behavior of porosity and feeding capabilities of sodium- and strontium-modified Al-Si alloys*. AFS Transactions, 1990. **98**: p. 167-173.
192. Liu, L., A. M. Samuel, F. H. Samuel, H. W. Doty and S. Valtierra, *Influence of oxides on porosity formation in Sr-treated Al-Si casting alloys*. Journal of Materials Science, 2003. **38** (6): p. 1255-1267.
193. Fasoyinu, F.A., *Effect of mg concentration on drossing tendency, inclusion formation, casting fluidity, hydrogen pick up and mechanical properties from gravity diecasting alloy A380.0*. AFS Transactions, 1994. **102**: p. 515-528.
194. S. Impey, D.J. Stephenson, J.R. Nicholls. *A study of the effect of magnesium additions on the oxide growth morphologies on liquid aluminum alloys*. in *Proceedings of 1st International Conf. Uni. of Cambridge*. 1990. Cambridge.
195. Q.T. Fang, D.A. Granger, *Porosity formation in modified and unmodified A356 alloy castings*. AFS Transactions, 1989. **97**: p. 989-1000.
196. R. Fuoco, E.R. Correa, A.V.O. Correa, *Effect of modification treatment on microporosity formation in 356 Al alloy*. AFS Transactions, 1995. **103**: p. 379-387.
197. R. Fuoco, E.R. Correa, H. Goldenstein, *Effect of modification treatment on microporosity formation in 356 Al alloy, Part I: interdendritic feeding evaluation*. AFS Transactions, 1996. **104**: p. 1151-1157.
198. Haque, M. M., *Effects of strontium on the structure and properties of aluminium-silicon alloys*. Journal of Materials Processing Technology, 1995. **55** (3-4): p. 193-198.
199. Q.T. Fang, P.N. Anyalebechi, D.A. Granger, *Measurement of Hydrogen Porosity in Unidirectional Solidified Aluminum Alloys*. Light Alloys, 1988: p. 477-486.
200. Li, B. Q. and P. N. Anyalebechi, *A micro/macro model for fluid flow evolution and microstructure formation in solidification processes*. International Journal of Heat and Mass Transfer, 1995. **38** (13): p. 2367-2381.
201. C.H. Caceres, M.B. Djurdjevic, T.J. Stockwell, J.H. Sokolowski, *The effect of Cu content on the level of microporosity in Al-Si-Cu-Mg casting alloys*. Scripta Materialia, 1999. **40** (5): p. 631-637.
202. Haque, M. M. and M. A. Maleque, *Effect of process variables on structure and properties of aluminium-silicon piston alloy*. Journal of Materials Processing Technology, 1998. **77** (1-3): p. 122-128.
203. Young, M.J., *Correlation of tensile properties to the amount of gas porosity in permanent mold test bars*. AFS Transactions, 1981. **89**: p. 465-468.
204. Jahrling, Katia and Stephen Tait, *Measurements of the evolution of porosity in a mushy layer*. Journal of Crystal Growth, 1996. **167** (1-2): p. 285-291.
205. L.A. Narayanan, F.H. Samuel, J.E. Gruzleski, *Crystallisation behavior of iron-containing intermetallic compounds in 319 aluminum alloy*. Metallurgical and Materials Transactions A, 1994. **25A** (August): p. 1761-1773.
206. A. Pennors, A.M. Samuel, F.H. Samuel, H.W. Doty, *Precipitation of  $\beta$ -Al<sub>5</sub>FeSi iron intermetallic in Al-6%Si-3.5%Cu (319) type alloys: role of Sr and P*. AFS Transactions, 1998. **106**: p. 251-264.

207. F.H. Samuel, P. Ouellet, A.M. Samuel, H.W. Doty, *Effect of Mg and Sr additions on the formation of intermetallics in Al-6 wt pct Si-3.5 wt pct Cu-(0.45) to (0.8) wt pct Fe 319 type alloys*. Metallurgical and Materials Transactions A, 1998. **29A** (December): p. 2871-2884.
208. F.H. Samuel, A.M. Samuel, H.W. Doty, S. Valtierra, *Decomposition of Fe-intermetallics in Sr-modified cast 6xxx type aluminum alloys for automotive skin*. Metallurgical and Materials Transactions A, 2001. **32A** (August): p. 2061-2075.
209. Crepeau, P.N., *Effect of iron in Al-Si casting alloys: a critical review*. AFS Transactions, 1995. **103**: p. 361-366.
210. J.C. Church, K.L. Herrick, *Quantitative gas testing for production control of aluminum casting soundness*. AFS Transactions, 1970. **78**: p. 277-280.
211. D.J. Neil, A.C. Burr, *Initial bubble test for determination of hydrogen content in molten aluminum*. AFS Transactions, 1961. **69**: p. 272-275.
212. L.C.B. Martins, C.W. Sanderson, J. Tessandori, *NOTORP hydrogen analyzer operating principles and application at commonwealth aluminum*. Light Metals, 1998: p. 817-826.
213. H. Rosenthal, S. Lipson, *Measurement of gas in molten aluminum*. AFS Transactions, 1955. **63**: p. 301-305.
214. [www.abb.com](http://www.abb.com), *ABB Ltd*.
215. A.R. Khoei, I. Masters, D.T. Gethin. *The application of Taguchi Methods to the Aluminium Recycling Process*. in *4th ASM International Conference on the Recycling of Metals*. 1999.
216. Tenorio, J. A. S. and D. C. R. Espinosa, *Effect of salt/oxide interaction on the process of aluminum recycling*. Journal of Light Metals, 2002. **2** (2): p. 89-93.
217. Samuel, M., *A new technique for recycling aluminium scrap*. Journal of Materials Processing Technology, 2003. **135** (1): p. 117-124.
218. A.R. Khoei, I. Masters, D.T. Gethin, *Design optimisation of aluminum recycling process using Taguchi technique*. Journal of Materials Processing Technology, 2002. **127**: p. 96-106.
219. S.B. Davies, I. Masters, D.T. Gethin. *Numerical modelling of a rotary aluminum recycling furnace*. in *Proc. 4th International Symposium on Recycling of Metals and Engineered Materials*. 2000. TMS.
220. N. Unlu, M.G. Drouet, *Comparison of salt-free aluminum dross treatment processes*. Resources, Conservation and Recycling, 2002. **36**: p. 61-72.
221. Gallo, R., *Development, evaluation and application of solid fluxes*. Modern Casting, 2002(October): p. 30-33.
222. Gallo, R., *Development, evaluation and application of granular and powder fluxes in transfer ladles, crucible and reverberatory furnaces*. Foseco, 2002. **237** (May): p. 8-16.
223. R.R. Corns, T.P. Rack, *Practical implementation of aluminum degassing using a new non-toxic gas mixture*. AFS Transactions, 1989. **97**: p. 983-988.
224. J.A. Dantzig, J.A. Clumpner, D.E. Tyler, *Degassing of static melts by insoluble purge gases*. Metallurgical and Materials Transactions B, 1980. **11B** (September): p. 433-438.
225. Neff, D.V., *Understanding aluminum degassing*. Modern Casting, 2002 (May): p. 24-26.
226. H. Ni, B. Sun, H. Jiang, D. Shu, W. Ding, *Degassing effect of RE flux on aluminum melt*. AFS Transactions, 2002. **110**: p. 267-270.

227. X.-G. Chen, F.J. Klinkenberg, R. Ellerbrok, S. Engler, *Efficiency of impeller degassing and regassing phenomena in aluminum melts*. AFS Transactions, 1994. **102**: p. 191-197.
228. J.E. Gruzleski, B. Closset, *Treatment of Liquid Aluminum-Silicon Alloys*. 1990: American Foundry Society.
229. [www.pyrotek.info](http://www.pyrotek.info), Pyrotek Inc.
230. Weibull, W., *A statistical distribution function of wide applicability*. Journal of Applied Mechanics, 1951 (September): p. 293-297.
231. *Personal discussions and unpublished work of M. Tiryakioglu*
232. *Personal discussions and unpublished work of N.R. Green*
233. E.L. Rooy, E.F. Fisher, *Control of aluminum casting quality by vacuum solidification test*. AFS Transactions, 1968. **76**: p. 237-240.
234. W. LaOrchan, M.H. Mulazimoglu, J.E. Gruzleski, *Constant volume risered mold for reduced pressure test*. AFS Transactions, 1993. **101**: p. 253-259.
235. W. LaOrchan, M.H. Mulazimoglu, J.E. Gruzleski, *Quantification of the reduced pressure test*. AFS Transactions, 1991. **99**: p. 653-659.
236. J.E. Gruzleski, W. La Orchan, H. Mulazimoglu, *New reduced pressure test quantifies hydrogen content*. Modern Casting, 1995 (September): p. 47-49.
237. L. Parmenter, D. Apelian, F. Jensen, *Development of a statistically optimized test method for the reduced pressure test*. AFS Transactions, 1998. **106**: p. 439-452.
238. M.H. Mulazimoglu, N. Handiak, J.E. Gruzleski, *Some observations on the reduced pressure test and hydrogen concentration of modified A356 alloy*. AFS Transactions, 1989. **97**: p. 225-232.
239. S. Dasgupta, L. Parmenter, D. Apelian. *Relationship between the reduced pressure test and hydrogen content of the melt*. in *5th International AFS Conference Moletn Aluminum Proceedings*. 1998.
240. W. LaOrchan, M.H. Mulazimoglu, X.-G. Chen, J.E. Gruzleski, *Quantified reduced pressure test*. AFS Transactions, 1995. **103**: p. 565-574.
241. Liao, Hengcheng and Guoxiong Sun, *Mutual poisoning effect between Sr and B in Al-Si casting alloys*. Scripta Materialia, 2003. **48** (8): p. 1035-1039.
242. Liao, Hengcheng, Yu Sun and Guoxiong Sun, *Correlation between mechanical properties and amount of dendritic [alpha]-Al phase in as-cast near-eutectic Al-11.6% Si alloys modified with strontium*. Materials Science and Engineering A, 2002. **335** (1-2): p. 62-66.
243. J.M. Kim, H.W. Kwon, C.R. Loper Jr., *Feeding behavior of modified and unmodified Al-Si alloys*. AFS Transactions, 1996. **104**: p. 743-749.
244. S.-T. Kao, E. Chang, *Feeding efficiency criteria for porosity formation in A356 alloy sand plate castings*. AFS Transactions, 1996. **104**: p. 545-549.
245. Dahle, A. K. and D. H. StJohn, *Rheological behaviour of the mushy zone and its effect on the formation of casting defects during solidification*. Acta Materialia, 1998. **47** (1): p. 31-41.
246. M. Dash, M. Makhlof, *Effect of key alloying elements on the feeding characteristics of aluminum-silicon casting alloys*. Journal of Light Metals, 2001. **1**: p. 251-265.
247. J.R. Denton, J.A. Spittle, *Solidification and susceptibility to hydrogen absorption of Al-Si alloys containing strontium*. Materials Science and Technology, 1985.
248. R. Raeiszadeh, W.D. Griffiths (2005). *A Method to Study the Life-Cycle of a Double Oxide Film Defect in Liquid Aluminum Alloys*. 134<sup>th</sup> TMS Annual Meeting, Shape Casting: *The John Campbell Symposium*, San Francisco, US, pp. 13-22

249. L.-P. Martin, G. Dube, D. Frayce, R. Guthrie, *Settling phenomena in casting furnaces: a fundamental and experimental investigation*. Light Metals, 1988: p. 445-455.
250. Pekguleryuz, Mihriban O. and Nicolas Pedneau, *In-Situ Method for the Investigation of Equiaxed Grain Growth in Hypoeutectic and Hypereutectic Al-Si Alloys*. Scripta Materialia, 1998. **38** (10): p. 1533-1539.
251. M. Drouzy, S. Jacob, M. Richard, *Interpretation of tensile results by means of quality index and probable yield strength*. AFS Int Cast Metal Jnl, 1980. **5**: p. 43-50.
252. Mondolfo, L.F., *Aluminum Alloys: Structure and Properties*. 1976: Butterworth Co. Ltd.
253. Sulinski, J., AFS Transactions, 1967. **75**: p. 548-566.
254. Bailey, W.A., Foundry, 1964 (May): p. 54-60.
255. R. Dasgupta, C.C. Brown, S. Marek, *Effect of increased magnesium content on the mechanical properties of sand-cast 319 aluminum alloy*. AFS Transactions, 1989. **97**: p. 245-254.
256. G.E. Nagel, J.P. Mouret, J. Dubruelh, *A357 type alloy with improved properties*. Trans. Amer. Foundrymen Soc, 1983. **91**: p. 157-160.
257. Caceres, C. H. and B. I. Selling, *Casting defects and the tensile properties of an Al-Si-Mg alloy*. Materials Science and Engineering A, 1996. **220** (1-2): p. 109-116.
258. M. Divandari, J. Campbell, *A new technique for the study of aluminum oxide films*. Aluminum Transactions, 2002. **2** (2): p. 233-238.

## APPENDIX I

### Calculation of Theoretical Hydrogen-Density Relationship

Density of a sample is defined by mass divided by its volume:

$$d = \frac{m}{V}$$

If there is  $V$  amount of gas present in the sample, then the density should be:

$$d = \frac{m_{metal} + m_{gas}}{V_{metal} + V_{gas}}$$

the weight of the gas is negligible ,  $m_{gas}=0$ ,

$$d = \frac{m_{metal}}{V_{metal} + V_{gas}}$$

Any ‘ $V$ ’ amount (volume) of gas will decrease the density accordingly.

In the reduced pressure test, since solidification is carried under vacuum, then  $V$  volume of gas will be enhanced by the vacuum action according to the following equation:

$$P_1V_1 = P_2V_2$$

Therefore, for example, if the reduced pressure test is carried at 100 mbar, the volume of the gas should be:

$$1000.V_1 = 100.V_2$$

$$V_2 = 10.V_1$$

signifying that the volume of hydrogen should be 10 times greater at 100 mbar.

For example, if the measured hydrogen level of the melt is 0.24 cc/100g Al, then the density of the sample without any pore should be:

$$2,7 \text{ g / cc} = \frac{100 \text{ g}}{37,03 \text{ cc}}$$

0.24 cc/100g Al hydrogen level at 100 mbar = 2.4 cc/100g Al, then the density measured after reduced pressure test should be lowered accordingly:

$$d = \frac{100}{37.03 + 2.4}$$

$$d=2.43 \text{ g/cc}$$

## APPENDIX II

### Comparison of Image Analysis Software

To make sure that the image analysis results were accurate, three different software packages were compared (Sigma Plot -SPSS, MCID, Clemex). First a simple test was done: shapes of ellipses with known dimensions were subjected to image analysis. The data collected from the image analysis is summarised in Tables 1-3. The results are given in Figures 1-3.

**Table 1:** Image analysis results for Shape Factor

SHAPES	Height	Width	Calculated Shape Factor	MCID Shape Factor	SPSS Shape Factor	CLEMEX Shape Factor
	1	1	1.00	0.99	0.90	1.00
	1	2	0.80	0.84	0.76	0.83
	1	3	0.60	0.66	0.61	0.66
	1	4	0.47	0.54	0.50	0.53
	1	5	0.38	0.45	0.42	0.45
	1	6	0.32	0.39	0.36	0.37
	1	7	0.28	0.34	0.32	0.33
	1	8	0.25	0.30	0.28	0.30
	1	9	0.22	0.27	0.26	0.27
	1	10	0.20	0.24	0.23	0.24
	1	11	0.18	0.22	0.21	0.22
	1	12	0.17	0.20	0.20	0.20
	1	13	0.15	0.19	0.18	0.19
	1	14	0.14	0.18	0.17	0.18
	1	15	0.13	0.17	0.16	0.16

**Table 2:** Image analysis results for Area

SHAPES	Height	Width	Calculated Area	MCID Area	SPSS Area	CLEMEX Area
	1	1	0.79	0.81	0.81	0.86
	1	2	1.57	1.61	1.61	1.70
	1	3	2.36	2.41	2.41	2.54
	1	4	3.14	3.22	3.22	3.40
	1	5	3.93	4.01	4.01	4.23
	1	6	4.71	4.80	4.80	4.91
	1	7	5.50	5.60	5.60	5.91
	1	8	6.28	6.40	6.40	6.74
	1	9	7.07	7.21	7.21	7.59
	1	10	7.85	8.02	8.02	8.43
	1	11	8.64	8.81	8.81	9.27
	1	12	9.42	9.61	9.61	10.10
	1	13	10.21	10.43	10.43	10.97
	1	14	10.99	11.20	11.20	11.78
	1	15	11.78	12.01	12.01	12.47

**Table 3:** Image analysis results for Length

SHAPES	Height	Width	Calculated Length	MCID Length	SPSS Length	CLEMEX Length
	1	1	1	1.02	1.02	1.06
	1	2	2	2.00	1.98	2.05
	1	3	3	3.03	3.00	3.11
	1	4	4	4.03	4.00	4.14
	1	5	5	5.00	4.97	5.14
	1	6	6	6.00	5.97	6.16
	1	7	7	7.00	6.97	7.19
	1	8	8	8.00	7.97	8.19
	1	9	9	8.97	8.95	9.19
	1	10	10	9.97	9.95	10.22
	1	11	11	10.97	10.95	11.24
	1	12	12	11.95	11.92	12.24
	1	13	13	12.92	12.92	13.27
	1	14	14	13.95	13.92	14.30
	1	15	15	14.95	14.92	15.32

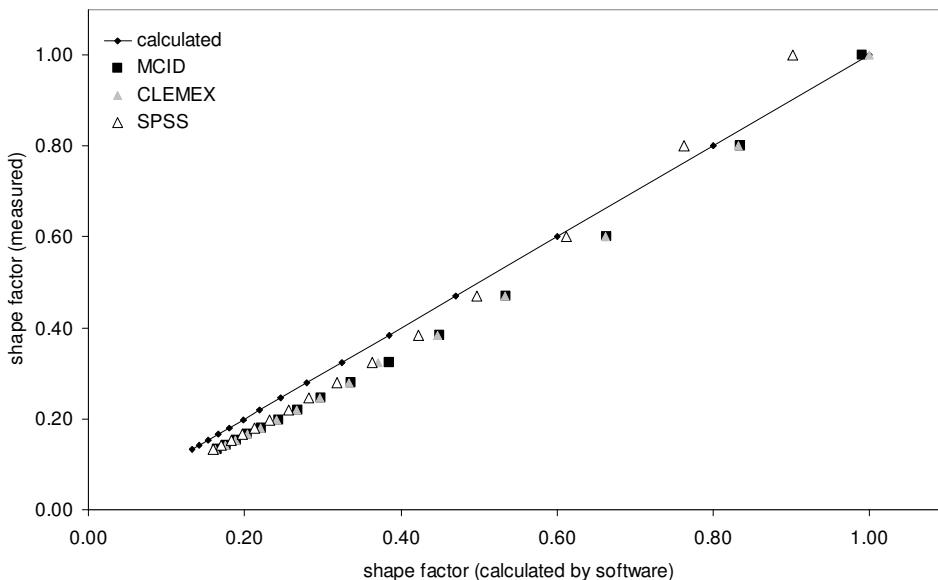


**Figure 1:** Comparison of shape factor that is calculated with three different software

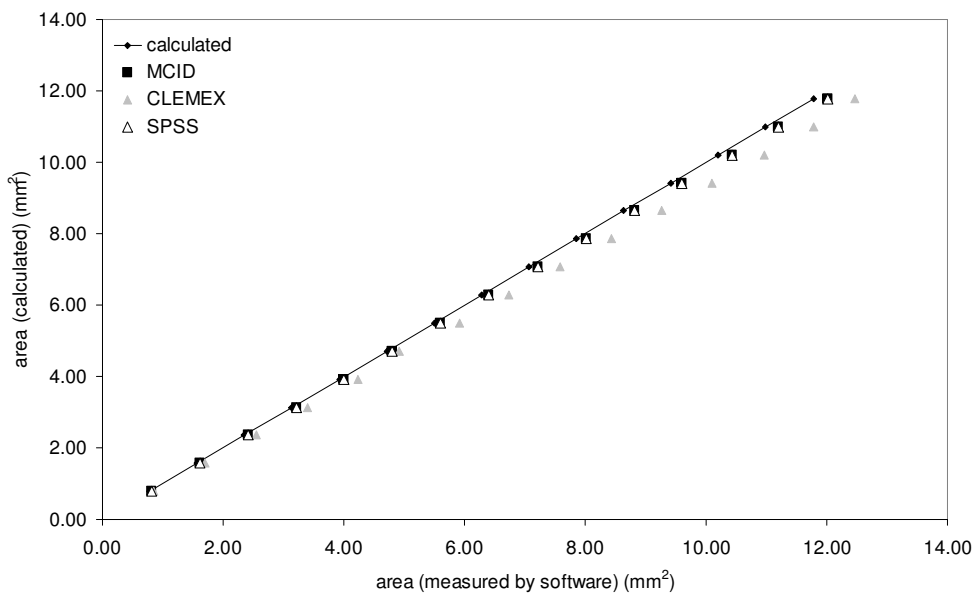


**Figure 2:** Comparison of area that is calculated with three different software

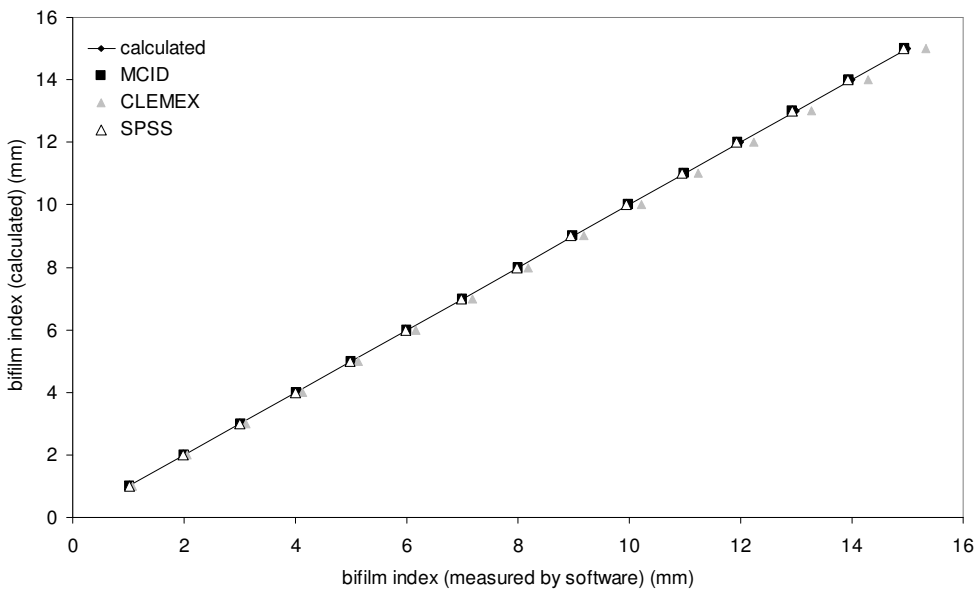


**Figure 3:** Comparison of maximum length that is calculated with three different software

**Table 4:** Image analysis results of complex shapes comparing three different software

	Shape factor			Area			Length		
	MCID	SPSS	CLEMEX	MCID	SPSS	CLEMEX	MCID	SPSS	CLEMEX
	0.80	0.80	0.80	8.27	8.27	8.29	4.03	4.03	4.39
	0.72	0.71	0.72	18.82	18.82	18.83	6.63	6.93	6.62
	0.61	0.54	0.61	4.13	4.13	4.11	2.85	3.16	3.09
	0.67	0.66	0.67	18.88	18.88	18.89	6.63	7.18	6.63
	0.55	0.54	0.55	4.13	4.13	4.09	2.72	4.01	3.09
	0.61	0.60	0.61	6.16	6.16	6.14	2.88	3.18	3.78
	0.95	0.95	0.97	6.84	6.84	6.84	2.88	3.09	3.99
	0.75	0.69	0.73	6.15	6.15	6.14	3.19	4.01	3.78
	0.99	0.90	0.98	6.40	6.40	6.39	2.88	2.86	3.86
	0.87	0.79	0.85	5.60	5.60	5.58	2.83	2.96	3.60
	0.38	0.35	0.38	4.06	4.06	4.03	4.13	4.73	3.06
	0.17	0.15	0.16	5.83	5.83	5.79	3.55	4.85	3.67

Then complex shapes as shown in Table 4 were used to analyse the same parameters.

To test the sensitivity of the image analysis software, circles with various dimensions (from 100 mm halving each time and down to 0.1 mm) were drawn. They were printed out and scanned and subjected to image analysis. As seen from Figures 4 and 5, the area and the bifilm index of these circles are in good relationship with the image analysis results. However, the shape factor calculations show (Figure 6) that there was a slight difference between the results; SPSS software appeared to give lower values compared to other software.

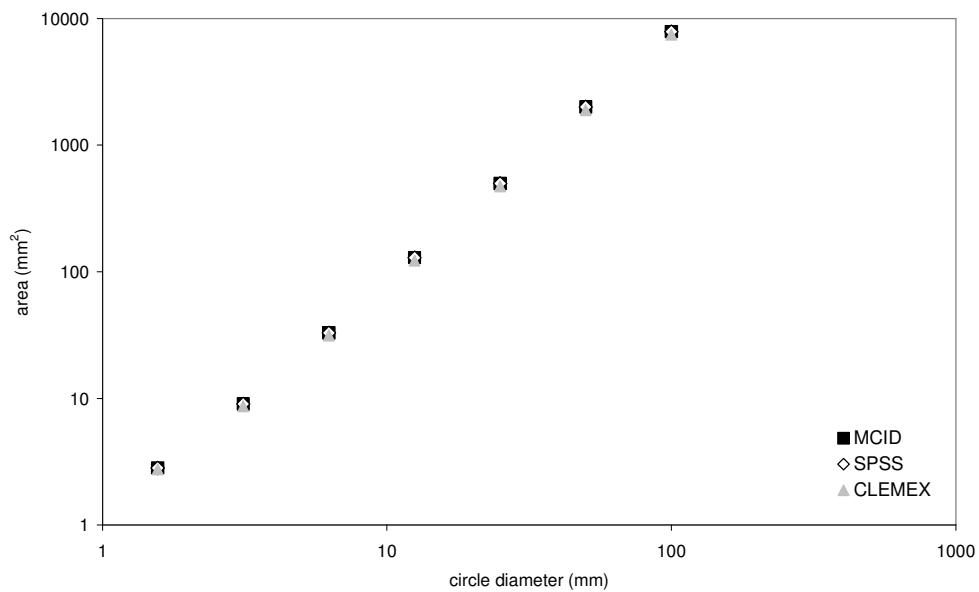


*Figure 4: Change in the area of circles*

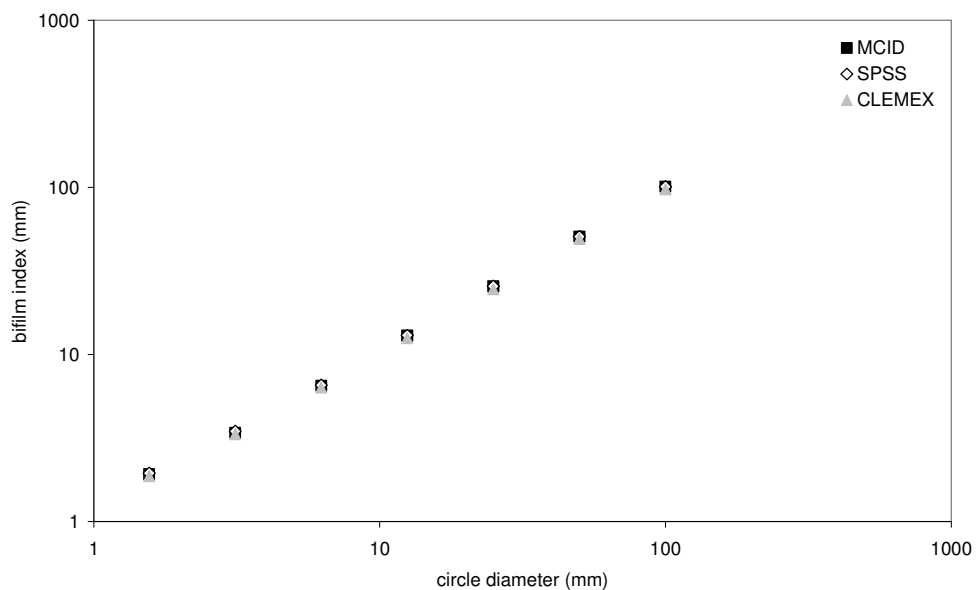


*Figure 5: change in the bifilm index*

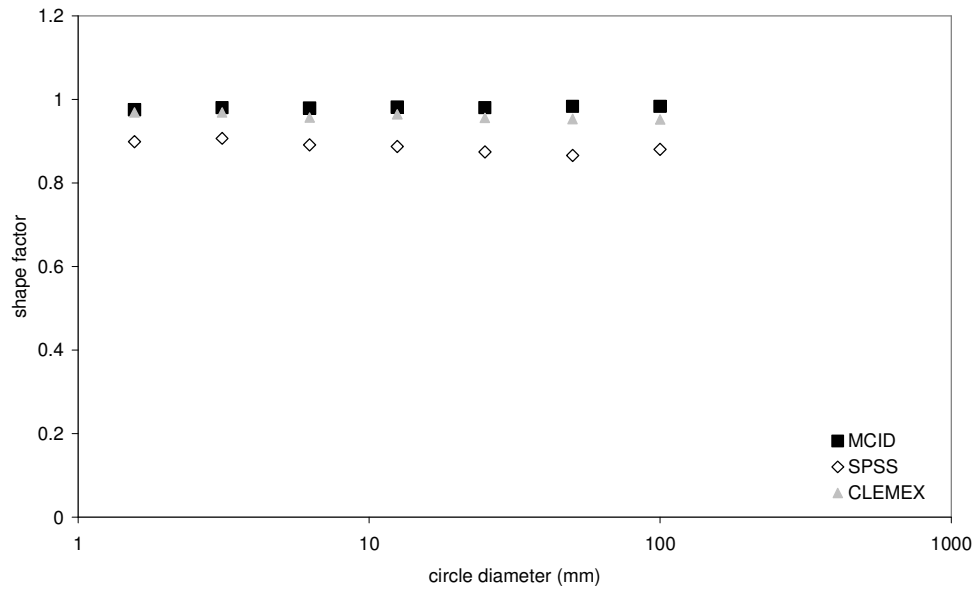


**Figure 6:** calculation of shape factor using different software

To make sure that the software (Sigma Plot) was measuring accurately, different scanning dpi (Dot per Inch) levels and different type of picture formats were used. As seen from Figure 7, there was no effect of these variables, the variation was only plus or minus 5%. However, as seen from Figure 8, the shape factor is very sensitive to the resolution used. For values below 600 dpi, the results are quite misleading, but for resolutions above 600 dpi, the results are constant and in good agreement with different picture formats used.

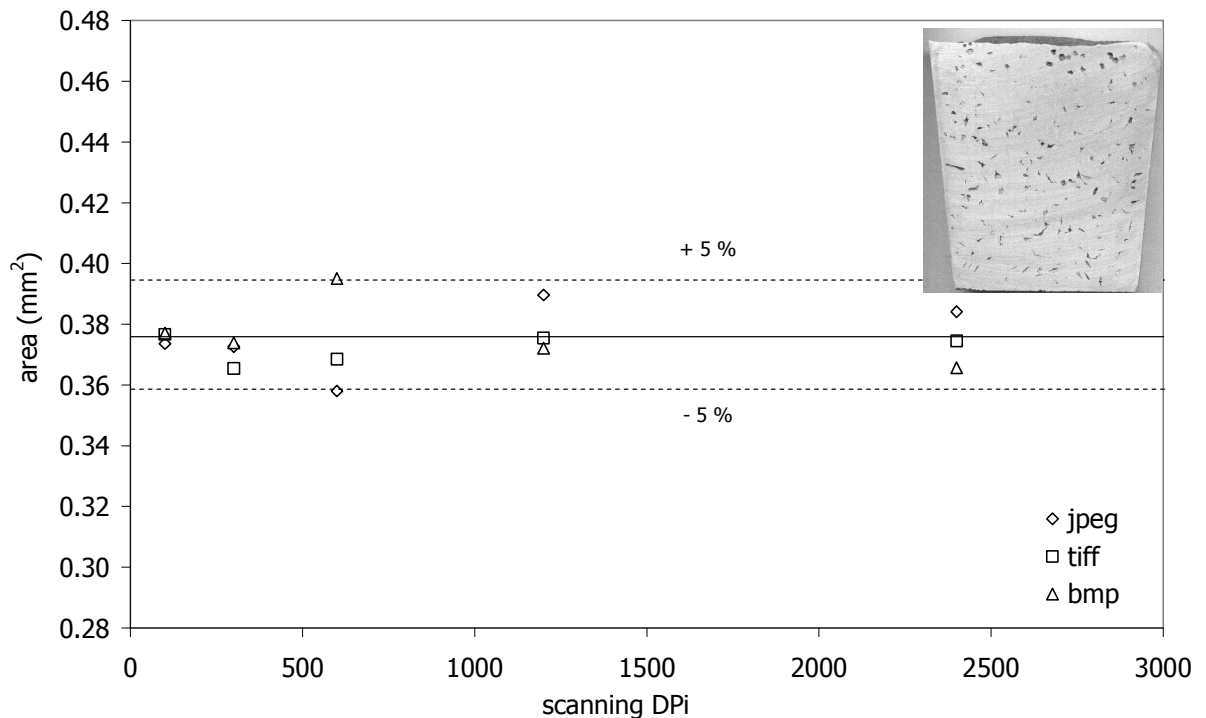


**Figure 7:** measured average area of pores that were scanned at different resolutions and saved at different picture formats

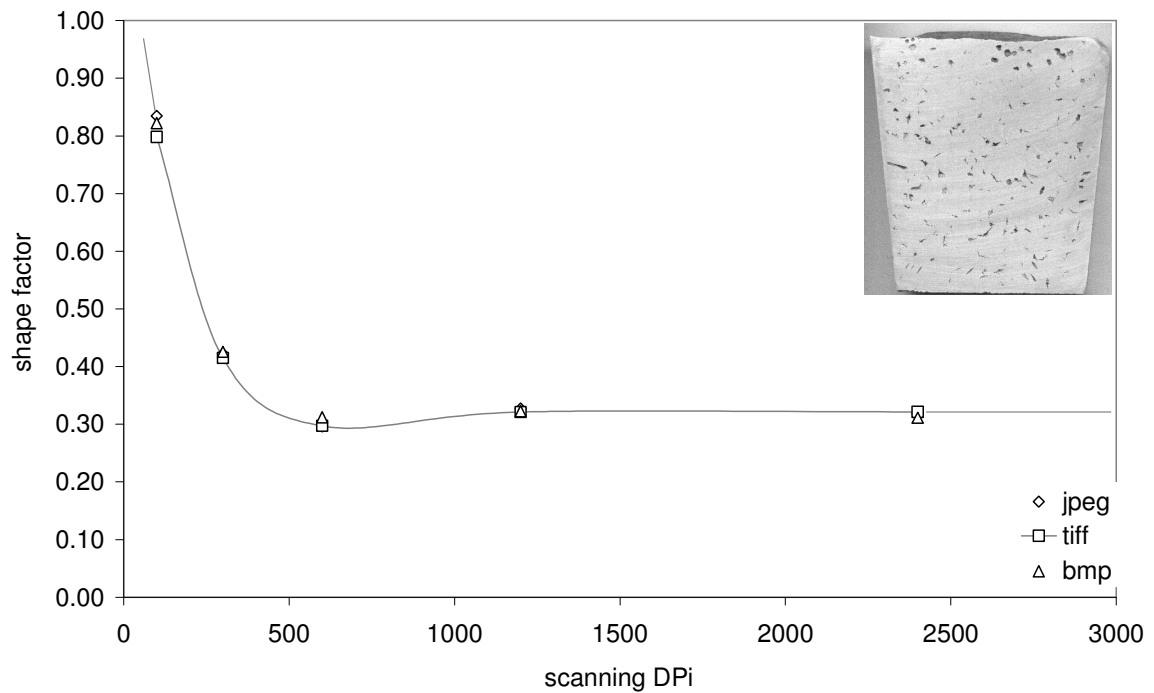


**Figure 8:** measured shape factor of pores that were scanned at different resolutions and saved at different picture formats

It is important to note that the shape factor results for the basic geometric figures were simple; however for the images of the sectioned surface of RPT samples (Figure 9), a round pore could easily give a shape factor of 0.61 rather than the expected value of 1. A further improvement is required in the software engineering of image analysis.

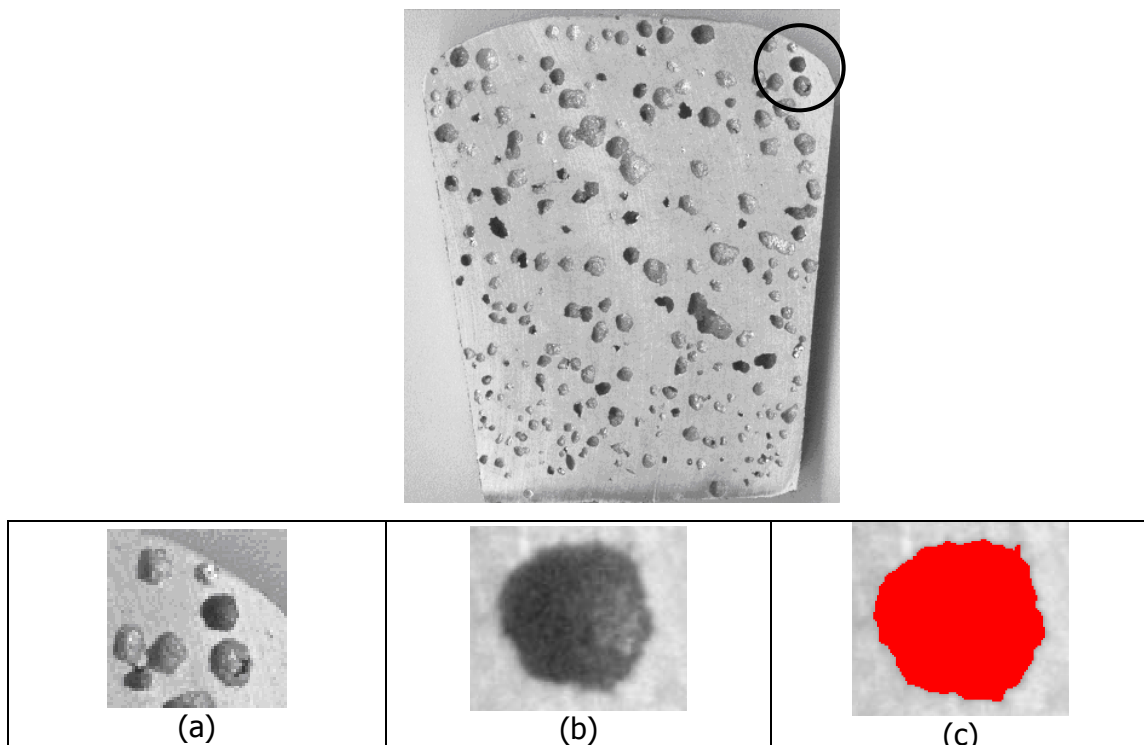


**Figure 9:** Calculation of shape factor: Result was= 0.61  
 Image scanned 1200 dpi saved in JPEG format  
 (a) a closer look at the pore, (b) the pore itself,  
 (c) after threshold is applied by software

## APPENDIX III

### Calculation of Air Gap between Bifilm

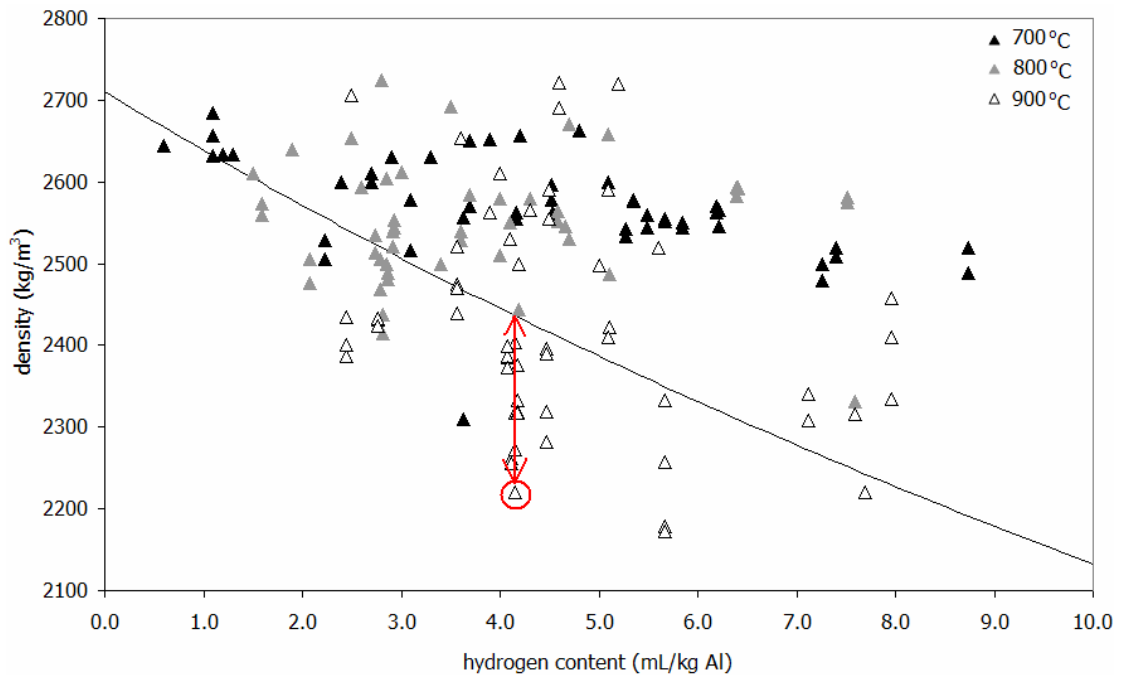


**Figure 1:** Relationship between density of RPT samples and Hydrogen content of the melt (100 mbar)  
(Figure taken from Section 4.1.2 – Figure 4.8 c)

A graph between density of RPT and hydrogen content was plotted (Figure 4.8). There exists a theoretical ‘almost’ linear relationship between density and hydrogen content (Appendix I). This linear line divides the graph into two parts: upper and lower. The samples above this line indicate that not all the available hydrogen had been used to form the pore. The samples on the line indicate all the hydrogen had been used for pore formation. The samples below this line indicated an additional source of gas in the pore. This is expected to be the contribution from air that had been originally entrained by the bifilms (Section 5.2).

Therefore an effort was made to calculate the quantity of air. A volume value was found from the density difference between the RPT sample and the theoretical density (for example: indicated by the arrow in Figure 1). This volume was the volume of *porosity* which formed at various temperatures (Figure 1) and at 100 mbar the RPT test pressure. This volume was converted to the STP value. Then, the volume of hydrogen at STP (measured by Hyscan equipment) was extracted from this value giving the volume of air per RPT sample at STP. Average bifilm index values and total number of pores are known for each sample from image analysis results of the sectioned surfaces of RPT samples. From this data, the average

volume of air can be calculated per pore. Given the average bifilm length for pore, an average air gap can be calculated per bifilm for each temperatures tested in the experiments.

Density ( $d$ ) of a sample is mass ( $m$ ) over volume ( $V$ ):

$$d = \frac{m}{V}$$

Volume of a pore is:

$$V_{pore} = \frac{m}{d_{RPT} - d_t}$$

$d_{RPT}$ : density of RPT samples

$d_t$ : theoretical density according to hydrogen level

Volume of air ( $V_{air}$ ) is the volume difference between the pore volume ( $V_{pore}$ ) and the volume of hydrogen ( $V_{Hydrogen}$ ):

$$V_{air} = V_{pore} - V_{Hydrogen}$$

This volume of the air is formed at 100 mbar (under vacuum in RPT test) at the melt temperature (or casting temperature) which needs to be converted to the STP volume which is calculated by:

$$\frac{P_1 V_1}{T_1} = \frac{P_2 V_2}{T_2}$$

$$P_1 = 1000 \text{ mbar}$$

$$V_1 = \text{volume of air at STP}$$

$$T_1 = 293\text{K}$$

$$P_2 = 100 \text{ mbar}$$

$$V_2 = \text{volume of air at RPT (calculated above as } V_{air}\text{)}$$

$$T_2 = 973\text{K}$$

$$V_1 = \frac{293.100.V_2}{1000.973}$$

$V_1$  is the total volume of air gap between bifilms in a RPT sample. From the image analysis results of the sectioned surface of RPT samples, number of pores and bifilm index is calculated. From this data, average air gap per pore (and per bifilm index) can be calculated.

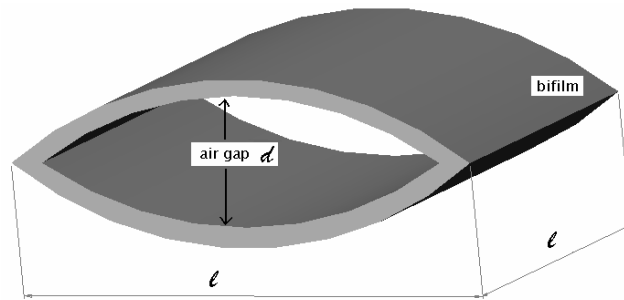


**Figure 2:** A schematic representation of a bifilm

Considering a simple geometry of a bifilm (Figure 2), if the bifilms are assumed to be equally as long, on average, in distances measured at right angles to the polished surface, as those measured distances in the polished surface. Then the average air gap thickness  $d$  from  $V$  volume of air would be given from the simple relation:

$$d = \frac{V}{(BI)^2}$$

$BI = l$  in Figure 2 and is the bifilm index (mm). Squaring this value will give an estimate of the total area of bifilm.